Thermoelectric Property Studies on Lead Chalcogenides, Double-filled Cobalt Tri-Antimonide and Rare Earth-Ruthenium-Germanium

by
Huijun Kong

A dissertation submitted in partial fulfillment
of the requirements for the degree of
Doctor of Philosophy
(Physics)
in The University of Michigan
2008

Doctoral Committee:

Professor Ctirad Uher, Chair
Professor Massoud Kaviany
Professor Bradford G . Orr
Professor Leonard M. Sander
Associate Professor Cagliyan Kurdak

Dedicated to my parents

Acknowledgments

I first wish to thank Professor Ctirad Uher, my committee chair and research advisor. Throughout the past four years, Professor Uher has supported me in completing this dissertation. He has taught me the work ethics as an experimental physicist by example. I am very grateful for his kindness, patience and encouragements, and for allowing me the freedom to work at my own pace.

My committee members deserve thanks for serving on my doctoral committee and for their insightful comments.

Special thanks are due to my collaborators, Professor Donald Morelli, Dr. Xun Shi, Professor Mercouri G. Kanatzidis, Dr. Pierre F. P. Poudeu, Dr. John Androulakis, Dr. Chia-Her Lin and Joseph Sootsman. The research presented in this dissertation would not have been possible without their contributions.

My current labmates, Dr. Yi-Jiunn Chien, Dr. Changpeng Li, my junior Lynn Endicott also merit special acknowledgement for helping and assisting me in the lab on a daily basis. I would like to thank Dr. Carl Henderson at EMAL for helping me with EPMA measurement. I greatly appreciate his assistance.

My parents have always been supporting me wholeheartedly. They provide me many opportunities in life. I am eternally grateful for their unconditional love and support.

Financial support for this thesis work was provided by the Office of Naval Research under MURI program, titled New Thermoelectric Materials for Direct Energy Conversion.

Table of Contents

List of Figures

List of Tables

Abstract

Motivated by the energy applications of thermoelectrics (TE) such as power generation and refrigeration, my research goal is to develop novel materials with high dimensionless figure-of-merit ZT. Thermoelectric materials are characterized over a broad temperature range from 2 K to 800 K. According to the definition of ZT ($=S^2\sigma T/\kappa$ where S is the Seebeck coefficient, σ the electrical conductivity, κ the thermal conductivity, and T the absolute temperature), reducing thermal conductivity κ increases ZT. However, it is challenging to tailor material structures to enhance acoustic phonon scattering without impeding charge transport. We investigated three types of solid-state compounds: lead chalcogenides, filled skutterudites and ternary germanides, for their structural, electronic, thermal, and magnetic properties. For lead chalcogenides, nanoparticles embedded in the lattice enhance the mid- to long-wavelength phonon scattering, significantly reducing lattice thermal conductivity κ_L (~ 0.4 $Wm^{-1}K^{-1}$ at 300 K for PbTe with 8% PbS). These nanostructured PbTe-based alloys exhibit the highest ZT of approximately 1.5. For *n*-type filled skutterudites, ZT close to 1.4 is achieved by placing Ba and Yb into the interstitial void of $CoSb_3$. Rare-earth ruthenium germanium compounds of the composition $R_3Ru_4Ge_{13}$ have the cage-like structure similar to filled skutterudites, resulting in relatively low κ_L (~ 2 $Wm^{-1}K^{-1}$ at 300 K). They could potentially be developed into a new class of prospective TE materials.

Chapter I

Introduction to Thermoelectrics

One of the most pressing challenges of our time is to find alternative energy sources which are environmentally friendly. Thermoelectricity is a phenomenon that describes conversion of thermal energy into electricity or vice-versa. It is based on three important transport effects: the Seebeck effect, the Peltier effect and the Thomson effect. These effects are explained in 1.1. The principle of thermoelectricity provides a "clean" way to generate electric power as well as perform cooling functions, along with other advantages such as the quietness (no moving parts) and long-term stability. Thermoelectric materials have attracted great attention from world-wide research groups because of their unique applications. For example, they are being considered for use in the tailpipes of carbon-neutral vehicles, in which engine exhaust heat could be recovered and converted to electric power. Thermoelectric devices for power generation and refrigeration are detailed in 1.4. The energy efficiency of thermoelectric devices is determined by the thermoelectric performance of materials of which they are made. Despite the advantages of thermoelectric technology, the efficiency of thermoelectric devices is still not high enough for widespread use. The goal is to search for novel thermoelectric materials with a high thermoelectric figure-of-merit (ZT).

For a very long time, bismuth telluride-based alloys have had the highest ZT, which is slightly above unity. During the last decade, the search for promising bulk thermoelectric materials has intensified. New material systems are being developed to achieve ZT well above unity. The most striking feature of these materials is that they possess very low thermal conductivities while maintaining good electrical properties. Section 1.5 gives a review of the established thermoelectric materials.

1.1 Thermoelectric Phenomena

1.1.1 Seebeck Effect

The Seebeck effect was first discovered by the German physicist Thomas Johann Seebeck in 1821 [1.1]. Seebeck first detected a voltage between two ends of a metal bar in the presence of a temperature gradient along the bar. It was later discovered that a compass needle deflected when placed in the vicinity of a closed loop formed of two dissimilar metals with a temperature difference between the junctions. This observation provides direct evidence that a current flows through the closed circuit driven by the temperature difference. A temperature difference causes charge carriers (electrons or holes) in the material to diffuse from the hot side to the cold side. Mobile charge carriers migrate to the cold side and leave behind their oppositely charged and immobile nuclei at the hot side thus giving rise to a thermoelectric voltage. The buildup of charge carriers on the cold side eventually ceases when there exists an equal amount of charge carriers drifting back to the hot side as a result of the electric field created by charge separation. At this point, the material reaches the steady state. Only an increase in the temperature difference can resume a buildup of more charge carriers on the cold side and thus lead to an increase in the thermoelectric voltage. The voltage, called the thermoelectric *emf*, is generated by a temperature difference between two different materials such as metals or semiconductors. This drives a continuous current flowing through the conductors if their junctions are kept at different temperatures.

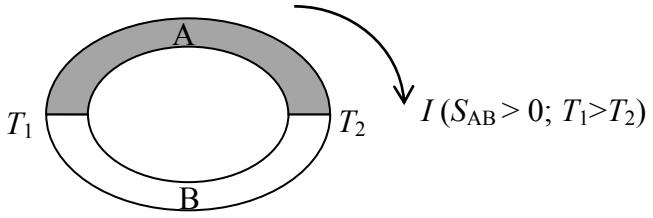

Fig. 1.1. Seebeck effect in a closed circuit. A, B are two conductors, and T_1, T_2 are the temperatures at the junctions.

If the differential Seebeck coefficient between A and B (S_{AB}) is positive, the current flows from junction 1 to 2 through conductor A (clockwise direction) when $T_1 > T_2$. In the case of an open circuit as shown in Fig. 1.2, voltage (ΔV) is developed between *a* and *b*.

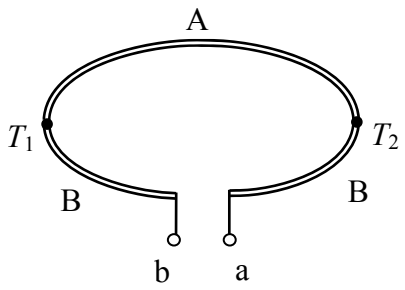

Fig. 1.2. Seebeck effect in an open circuit. a and b are the two open ends of the circuit.

In Eq. (1.1.1), S_A and S_B are the (absolute) Seebeck coefficients of material A and B, and T_1 and T_2 are the temperatures at the junction 1 and 2. The (absolute) Seebeck coefficient *S*, also called thermopower of a material, measures the magnitude of an induced thermoelectric voltage in response to a temperature difference across that material in units of μV/K.

$$\Delta V = V_a - V_b = \int_{T_2}^{T_1} S_{AB} dT = \int_{T_2}^{T_1} \left(S_A - S_B \right) dT \qquad (1.1.1)$$

1.1.2 Peltier Effect

The Peltier effect is the conversion of electricity into heat transfer. This effect was first observed in 1834 by Jean Peltier [1.2]. The Peltier effect can be regarded as the reverse of the Seebeck effect. The Peltier effect is the underlying foundation for thermoelectric refrigeration.

When an electric current passes through two dissimilar materials such as metals or semiconductors that are connected at two junctions, heat will be absorbed at one junction and liberated at the other junction. As a result, one junction cools off while the other heats up, depending on the direction of the current.

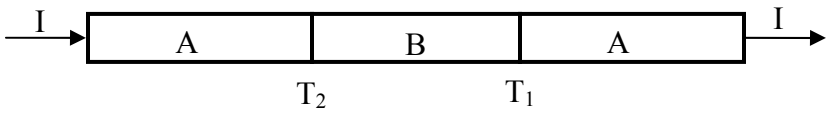

Fig. 1.3. An example of Peltier effect.

Peltier effect is illustrated in Fig. 1.3. When a current I flows through the circuit, heat is absorbed at the junction at T_2, and emitted at the junction at T_1 if the differential Peltier coefficient Π_{AB} is negative. The Peltier heat (Q) absorbed by the cold junction per unit time is given by

$$\frac{dQ}{dt} = \Pi_{AB} I = \left(\prod_A - \prod_B\right) I \tag{1.1.2}$$

where $\prod_A$ and $\prod_B$ are the Peltier coefficients of material A and B.

1.1.3 Thomson effect

Thomson effect is named after William Thomson, later known as Lord Kelvin. It is defined as the rate of heat emitted or absorbed in a current-carrying conductor subjected to a temperature gradient [1.3]. Metals such as zinc and copper have a hotter end at a higher potential and a cooler end at a lower potential. When current moves from the hotter end to the colder end, it is moving from a high to a low potential, so there is liberation of heat. This is called the positive Thomson effect. Metals such as cobalt, nickel, and iron have a cooler end at a higher potential and a hotter end at a lower potential. When current moves from the hotter end to the colder end, it is moving from a low to a high potential, and there is absorption of heat. This is called the negative Thomson effect. In lead, there is approximately zero Thomson effect.

If a current density J passes through a homogeneous conductor, heat production per unit volume q is

$$q = \rho J^2 - \mu J \frac{dT}{dx} \tag{1.1.3}$$

where ρ is the resistivity of the material, dT/dx is the temperature gradient along the conductor, and μ is the Thomson coefficient.

The first term in Eq. (1.1.3), $\rho J^2 (= RI^2 / V)$, represents the Joule heat per unit volume, which is not reversible. The second term, $\mu J \frac{dT}{dx}$, is the Thomson heat, which changes the sign when J changes direction. The reversible nature of the Thomson effect manifests itself in its mathematical form.

1.1.4 Thomson Relationships

The absolute Seebeck coefficent (S), Peltier coefficient (Π) and Thomson coefficient (μ) are related to one another by Thomson (or Kelvin) relationships [1.3], listed as Eq. (1.1.4) and (1.1.5):

$$S = \frac{\Pi}{T} \tag{1.1.4}$$

$$\frac{dS}{dT} = \frac{\mu}{T} \tag{1.1.5}$$

1.2 Thermoelectric Figure-of-merit

In the early 1900s, E. Altenkirch introduced the concept of figure of merit [1.4-1.5]. It qualitatively showed that good thermoelectric materials should have high electrical conductivity to minimize Joule heating, low thermal conductivity to retain heat at the junctions and maintain a large temperature gradient, and large Seebeck coefficients for maximum conversion of heat to electrical power or electrical power to cooling performance. These three properties were later incorporated mathematically into one formula. The commonly used figure-of-merit (FOM) of a thermoelectric material is defined as:

$$Z \equiv \frac{S^2 \cdot \sigma}{\kappa} \tag{1.2.1}$$

where S is the Seebeck coefficient, σ is the electrical conductivity and κ is the thermal conductivity, as introduced in the section 1.1. Since Z has a unit of K^{-1}, one often uses

dimensionless figure-of-merit defined as *ZT*. The figure of merit (*ZT*) is the standard measure of a single material's thermoelectric performance. *ZT* is directly related to energy conversion efficiency (η). The rule of thumb is that higher *ZT* leads to more efficient energy conversion. The mathematical forms are included in 1.4.

1.3 Optimization of Thermoelectric Performance

As follows from Eq. (1.2.1), good thermoelectric materials possess large power factor ($S^2\sigma$) and low thermal conductivity. Early on, both theoretical studies and experimental results of solid state materials have indicated that some semiconductors fit the profile nicely [1.6-1.7]. Recent research in thermoelectrics has been primarily focused on how to optimize the thermoelectric performance of these materials.

Compared to metals, semiconductors have larger thermopower (S) but lower electrical conductivity (σ). One way to increase electrical conductivity is to dope the materials. One needs to be aware that heavy doping decreases thermopower because the Fermi level is moved close to the corresponding band edge or even into the band itself. It is critical to find a doping level where power factor ($S^2\sigma$) is optimized. Although effective doping can increase the power factor, it is necessary to preserve the long-range crystalline order so as to sustain high carrier mobility.

In order to reduce thermal conductivity, the common approach is to introduce additional short-range disorder into the crystalline structure. On the other hand, the distortion inevitably impedes charge transport, which may reduce electrical conductivity. To minimize the carrier scattering, one could form alloys through substitution by isoelectronic elements. Due to the different sizes and masses, atomic substitution efficiently scatters relatively short-wavelength phonons, thereby reducing the thermal conductivity in crystalline solids up to the alloy limit. One of the main challenges of increasing ZT is to reduce thermal conductivity beyond the alloy limit. Several novel ideas have been proposed to increase ZT. One is the so-called electron crystal phonon glass (ECPG) concept [1.8]. It means that ideal thermoelectric materials look like good crystals for the electronic properties but behaves like glass from the thermal point of view. One can reduce the lattice thermal conductivity without dramatically reducing the power

factor. Another approach is to increase the power factor by manipulating electronic density of states (DOS) using low dimensional quantum confinement effects in materials such as quantum dot superlattices, nanowires and quantum wells [1.9-1.11].

In the course of this dissertation research, several routes were explored to effectively reduce the thermal conductivity of conventional and novel thermoelectric materials. By incorporating nanoparticles into lead chalcogenide-based alloys, the thermal conductivity can be reduced significantly, which leads to much improved ZT values of these compounds. In another class of novel thermoelectrics called skutterudites, such as $CoSb_3$, double-filling with "rattling" atoms achieves the same goal. The cage-like structure in skutterudites which favors the low thermal conductivity is also found in rare earth-ruthenium-germanium compounds. These materials can potentially be developed into another family of good thermoelectrics.

1.4 Thermoelectric Applications

1.4.1 Power generation

Thermoelectric generators convert heat into electrical power based on the Seebeck effect. A single-couple generator consists of a *p*-type leg and a *n*-type leg. The basic operation is illustrated in Figure 1.4. In practice, a thermoelectric power generation device uses a number of unicouples. The two legs of a single couple and many thermocouples in a thermoelectric device are connected thermally in parallel and electrically in series.

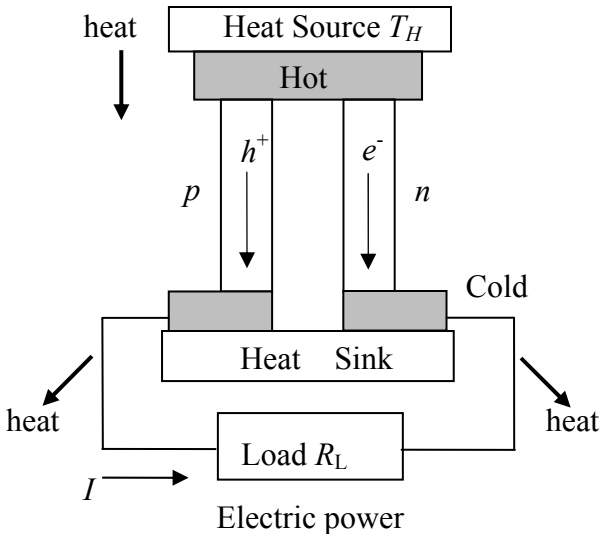

Fig. 1.4. Single-couple power generator using Seebeck effect.

Heat is pumped into one side of the couple and rejected from the opposite side. Heat flows through the two thermoelements. The thermocouple is connected to an electrical load of resistance R_L. An electrical current I, produced by the Seebeck voltage, is proportional to the temperature gradient between the hot and cold junctions ΔT.

$$I = \frac{(S_p - S_n) \cdot \Delta T}{R + R_L} \tag{1.4.1}$$

where R is the total electrical resistance of the device, S_p and S_n are the Seebeck coefficients of p-type and n-type leg, respectively. The useful power is given by

$$W = I^2 R_L \tag{1.4.2}$$

The heat drawn from the hot junction Q_H is partially lost because of the conduction through the thermoelements. The remainder is used to compensate for the Peltier cooling of the hot junction when a current is flowing. The efficiency of thermoelectric power generation η is defined as the ratio of power generated W to power drawn from a heat source Q_H [1.12].

$$\eta = \frac{W}{Q_H} = \frac{I\left[\left(S_p - S_n\right)\Delta T - IR\right]}{K\Delta T + \left(S_p - S_n\right)IT_H - I^2 R/2} \tag{1.4.3}$$

where K is the total thermal conductance with p, n legs in parallel. I, S_p, S_n, ΔT, R, R_L are the same notations as appeared in Eq. (1.4.1) and (1.4.2).

The figure of merit (Z) for a thermocouple is directly related to the maximum efficiency of thermoelectric power generator $\eta_{\max}$. If the load R_L is chosen to maximize the efficiency η, $\eta_{\max}$ is given by

$$\eta_{\max} = \frac{(\gamma - 1)\Delta T}{(\gamma + 1)T_H - \Delta T}; \quad \gamma = \left(1 + Z\overline{T}\right)^{1/2} \tag{1.4.4}$$

where Z is the figure of merit and $\overline{T}$ is the average temperature. For a single couple,

$$Z = \left(S_p - S_n\right)^2 / \left(KR\right); \; \overline{T} = \left(T_H + T_C\right)/2 \tag{1.4.5}$$

where K and R are the total thermal conductance (p, n legs in parallel) and electrical resistance (p, n legs in series). T_H and T_C are the temperatures of the hot and cold sides of the generator. As indicated in Eq. (1.4.4) and (1.4.5), the power generation efficiency η depends on the materials used in the thermocouple, the temperatures of the hot and cold sides of the generator, and the load driven by the generator. Eq. (1.4.4) can also be expressed as a function of Carnot efficiency of a generator ϕ_c ($= \Delta T / T_H$):

$$\eta_{\max} = \frac{\gamma - 1}{(\gamma + 1)/\phi_c - 1} \tag{1.4.6}$$

Figure 1.5 displays power generating efficiency $\eta_{\max}$ as a function of thermocouple's figure-of-merit ZT for different T_H, and T_C = 300 K. A thermocouple with ZT = 2.0 would have an efficiency of ~ 22% when T_H = 800 K, T_C = 300 K.

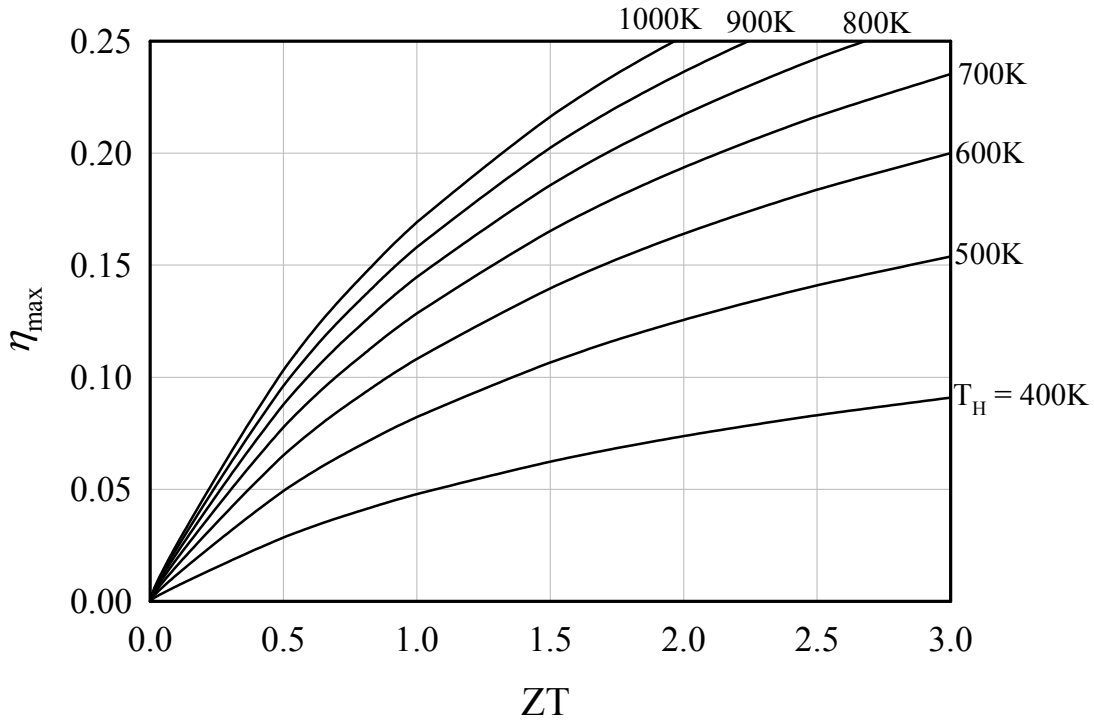

Fig. 1.5. Power generating efficiency η_{max} as a function of the dimensionless figure-of-merit of the thermocouple ZT for different T_H, and T_C = 300 K.

1.4.2 Thermoelectric Refrigeration

If an electric current is applied to the thermocouple as shown in Fig. 1.6, heat is pumped from the cold junction to the hot junction. The cold junction will rapidly drop below ambient temperature, provided heat is removed from the hot side. The temperature gradient will vary according to the magnitude of current applied.

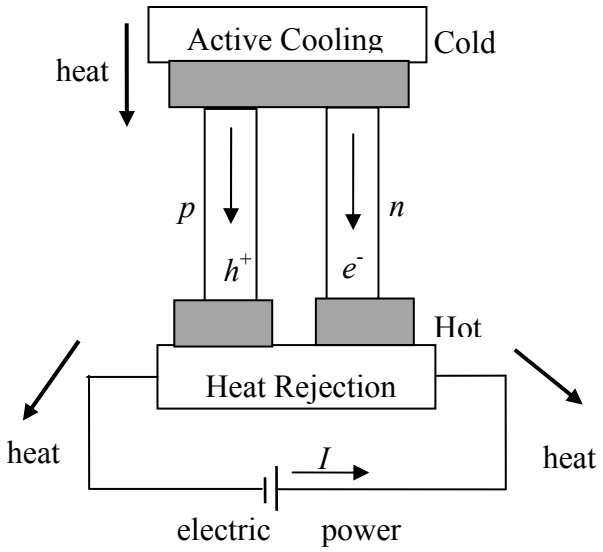

Fig. 1.6. Single-couple refrigerator using Peltier effect.

The coefficient of performance (COP) for a thermoelectric refrigerator ϕ is defined as the ratio of the heat flow rate drawn from the source Q_c to the total power consumption W [1.12].

$$\phi = \frac{Q_c}{W} = \frac{\left(S_p - S_n\right) IT - K\Delta T - I^2 R/2}{I\left[\left(S_p - S_n\right)\Delta T + IR\right]} \tag{1.4.7}$$

where K and R are the total thermal conductance (p, n legs in parallel) and electrical resistance (p, n legs in series) of a thermocouple. The maximum COP ($\phi_{\max}$) is

$$\phi_{\max} = \frac{T_c\left(\gamma - 1\right) - \Delta T}{\Delta T\left(\gamma + 1\right)} \tag{1.4.8}$$

where γ is defined in Eq. (1.4.4). The Carnot limit for a refrigerator is $T_c / \Delta T$. Eq. (1.4.8) can be rewritten as a function of the Carnot limit.

$$\phi_{\max} = \frac{\phi_c\left(\gamma - 1\right) - 1}{\gamma + 1} \tag{1.4.9}$$

1.5 State-of-the-art Thermoelectric Materials

Bismuth Telluride

Bi_2Te_3 has a tetradymite structure with space group $R\bar{3}m$. Fig. 1.7 shows, along the *c* axis, the lattice is stacked in a repeated sequence of five atom layers: Te^1-Bi-Te^2-Bi-Te^1 [1.13]. The superscripts 1 and 2 denote differently bonded tellurium atoms. The Te and Bi layers are held together by strong ionic-covalent bonds (Te^1-Bi and Bi-Te^2). The weak van der Waals force dominates between two adjacent Te^1 layers on the boundaries of these units, which accounts for the ease of cleavage in planes perpendicular to the *c*-axis. Both conduction and valence bands have six-fold symmetry. Recent reports indicate that nanostructured thin-film superlattices of Bi_2Te_3 and Sb_2Te_3 have $ZT \sim 2.4$ at room temperature. Bi_2Te_3 and its alloys such as *p*-type $Bi_{2-x}Sb_xTe_3$ and *n*-type $Bi_2Te_{3-x}Se_x$ are suitable for use below 400K and are thus premier materials for thermoelectric refrigeration at ordinary temperature [1.7]. The materials become chemically unstable at temperatures higher than that.

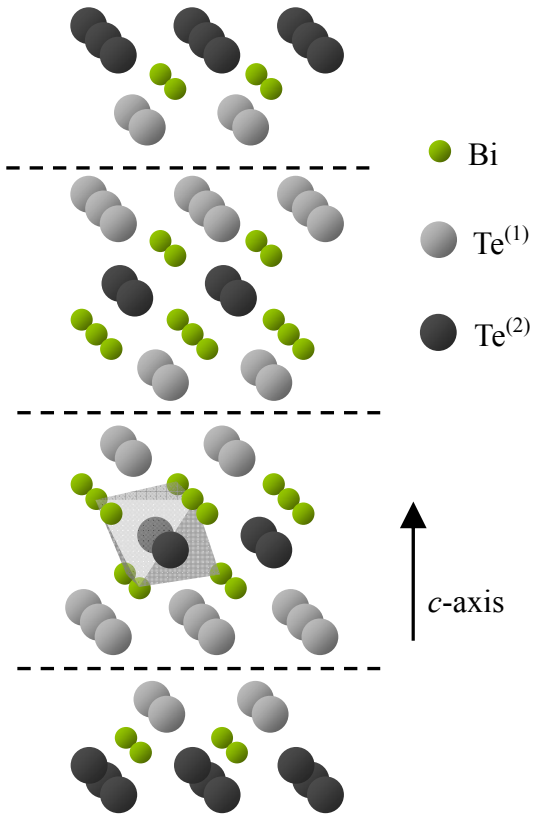

Fig. 1.7. Atomic layers in the Bi_2Te_3 crystal structure [1.13]. Dashed lines indicate van der Waals gaps. The octahedral coordination is highlighted for a $Te^{(2)}$ atom.

Bismuth-Antimony Alloy

Both bismuth and antimony are semimetals due to the energy overlaps between the conduction and valence bands. The overlap is small enough for the elements to display nonmetallic features such as a change of carrier concentration on the addition of impurities. For pure bismuth, the bands overlap by only about 0.02 eV. By alloying with 4-40% antimony, the Fermi level rises until a positive band gap appears so that the alloys become semiconductors [1.14]. The observed maximum band gap is about 0.014 eV corresponding to the composition $Bi_{0.88}Sb_{0.12}$. The dimensionless thermoelectric figure of merit (ZT) of Bi-Sb alloys can be substantially improved by applying magnetic fields in the bisectrix direction [1.7]. In zero magnetic field, the maximum value of ZT is less than 0.6 [1.15]. In a magnetic field of 0.15 T, ZT approaches 1.2 at temperatures of the order of 100 K [1.16].

$AgSbTe_2$-GeTe (TAGS)

The acronym TAGS stands for tellurium-antimony-germanium-silver. This material is formed by alloying silver antimony telluride, $AgSbTe_2$, with germanium telluride, GeTe. The structural phase transition from the cubic (NaCl) to rhombohedral structure occurs when GeTe fraction becomes less than 80%. The dimensionless figure-of-merit ZT of 1.2 at 700K is reported for $(AgSbTe_2)_{0.15}(GeTe)_{0.85}$ [1.17]. The composition with the optimal performance is close to the phase transition. Lattice strains related to the transition may play a part in reducing the lattice thermal conductivity, and thus increasing ZT. TAGS is an excellent *p*-type thermoelectric material in the temperature range of 600-800K. The drawbacks of TAGS system are the poor mechanical properties and relatively high cost.

Lead Chalcogenides

Chalcogenides are predominantly semiconductors, most of which are stable and have relatively high melting points. PbTe melts at 923^{o}C compared to 585^{o}C for Bi_2Te_3. These semiconductors are suitable for thermoelectric applications over a wide range of temperature of 100-1400 K, typically. Lead telluride has a maximum $ZT \sim 0.8$ at approximately 800K. This compound is widely used for power generation in the intermediate temperatures of 600-900 K.

In the past decade, reformed lead tellurides have led to improvements in performance. Bi-doped (*n*–type) $PbSe_{0.98}Te_{0.02}$/PbTe quantum dot superlattices grown by MBE have a *ZT* of 1.6 at 300K [1.9]. These thin-film $PbSe_{0.98}Te_{0.02}$/PbTe systems feature PbSe nanodots embedded in the PbTe matrix. At approximately 550 K, these samples were reported to exhibit *ZT* ~ 2.5. The high *ZT* value is achieved by a noticeable suppression of the thermal conductivity due to strong phonon scattering induced by the PbSe nanodots.

$AgSbTe_2$ and PbTe are both good thermoelectric candidates. Recently, the alloy of both materials $(PbTe)_m$-$AgSbTe_2$, or LAST-*m* materials ("LAST" stands for "lead-antimony-silver tellurium"), were reported to exhibit large *ZT* values from ~ 1.2 (LAST-10) to ~ 1.7 (LAST-18) at 700 K [1.18]. The atomic structure of $(PbTe)_m$-$AgSbTe_2$ can be described by substituting Ag and Sb for Pb sites in the PbTe matrix. High resolution TEM images of LAST- 18 samples revealed significant compositional modulations on a scale of 10nm, including endotaxially dispersed quantum dots. The nanoparticles are coherently embedded in the PbTe matrix, with a lattice mismatch of only about 2-4%. This endotaxy occurring in these materials could be highly conducive to facilitate excellent carrier transport throughout the sample and yet heat conduction is strongly suppressed [1.18]. The LAST materials actually show exceptionally low lattice thermal conductivity of ~ 0.45 $Wm^{-1}K^{-1}$ at 700 K (actual value depends on *m*). Such low lattice thermal conductivity is due to the scattering of mid-to-long wavelength phonons by the nanoparticles. Experimental results indicate that the formation of the nanostructures and the thermoelectric performance of LAST materials are very sensitive to synthesis conditions and small changes in chemical composition. Chapter IV focuses on the experimental work on reducing the thermal conductivity of lead chalcogenide-based materials such as $Pb_{9.6}Sb_{0.2}Te_{10-x}Se_x$ (where x = 0, 1, 2, 3, 4, 5, 6, 7, 8, 9, 10), PbTe + x%M (where M = Bi, Sb, InSb and $2 \leq x \leq 16$), $(Pb_{0.95}Sn_{0.05}Te)_{1-x}(PbS)_x$ (where x = 0.04, 0.08, 0.16) and PbTe + x%Eu (where x = 0.5, 1, 2, 3).

Skutterudites

Skutterudites represent a family of compounds with the structure MX_3, where M is Co, Rh, or Ir, and X is P, As, or Sb. The name of "skutterudite" originates from the name of a small Norwegian town called Skutterud where $CoAs_3$ was extensively mined.

Skutterudites can reach *ZT* beyond 1 in the range of 700-900 K. Take a unit cell of $CoSb_3$ as an example (see Fig. 1.8) [1.19]. Co_1 and Sb_6 are octahedrally bonded. The corner-sharing octahedra ($CoSb_6$) produce a void at the center of the eight $CoSb_6$ cluster, occupying a body-centered position in the cubic unit cell. The void is large enough to accommodate relatively large metal atoms, forming filled skutterudites. A selection of filler atoms such as rare earths, alkaline earths, and alkali metals can be introduced into the voids of the skutterudite structure to provide a broad spectrum of phonon scattering frequencies [1.20-1.21]. Each filler ion represents a phonon resonance scattering center with a specific frequency and only those normal phonon modes with frequencies close to this local resonant frequency can interact strongly with the vibration modes of the fillers. Therefore, filling the structure with multiple ions can suppress the lattice thermal conductivity κ_{latt}. The choice and concentration of the filler atoms are critical to reducing κ_{latt}. Like PbTe alloys, filled skutterudites are also used for power generation applications in the intermediate temperature range of 600-900K. As part of this thesis work, studies on *n*-type double-filled cobalt tri-antimonide $Ba_xYb_yCo_4Sb_{12}$ (where $0.03 \leq x \leq 0.15$ and $0 \leq y \leq 0.12$) are detailed in Chapter V.

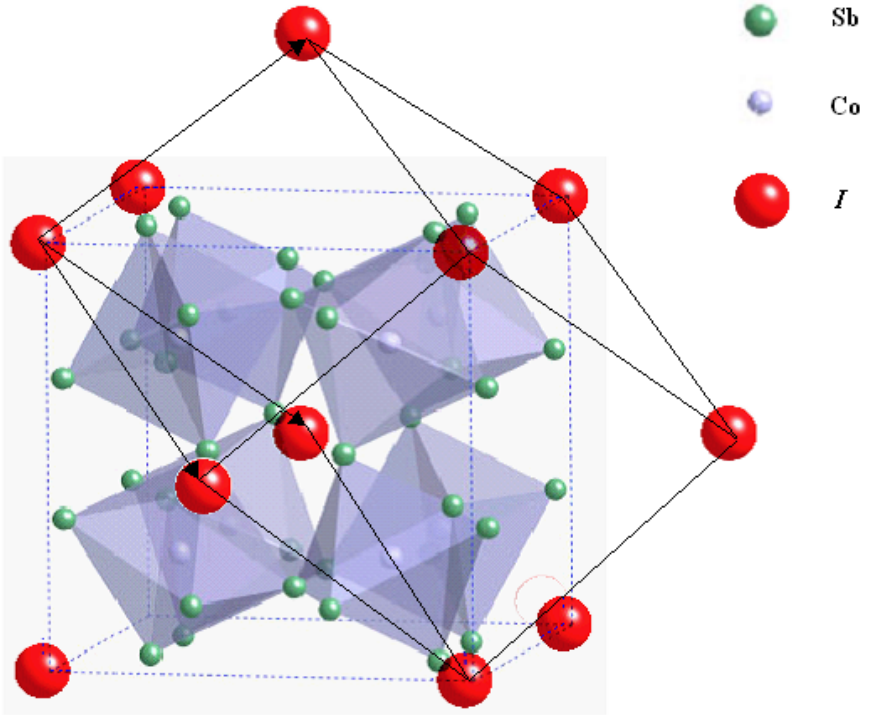

Fig. 1.8. A unit cell and a primitive cell of $CoSb_3$ inserted with filler ion *I* [1.19].

References to Chapter I

1.1 T. J. Seebeck, Abhandlungen der Deutschen Akademie der Wissenschaften zu Berlin, 265, 1822-1823.
1.2 J. C. Peltier, Ann. Phys. Chim. LV1, 371, 1834.
1.3 D. D. Pollock, Thermoelectricity: theory, thermometry, tool (ASTM 1985).
1.4 E. Altenkirsch, E. Phys. Z. **10**, 560 (1909)
1.5 E. Altenkirsch, E. Phys. Z. 12, 920 (1911)
1.6 A. F. Ioffe, Semiconductor Thermoelements and Thermoelectric Cooling (Infosearch 1957).
1.7 H. J. Goldsmid, Electronic Refrigeration (Pion Limited 1986).
1.8 G. A. Slack in CRC Handbook of Thermoelectrics, edited by D. M. Rowe (CRC Press, Boca Raton, 1995), p. 407.
1.9 T. C. Harman, P. J. Taylor, M. P. Walsh, B. E. LaForge, Science, **297**, 2229 (2002).
1.10 J. Heremans, C. M. Thrush, Phys. Rev. B **59**, 12579 (1999)
1.11 L. D. Hicks, M. S. Dresselhaus, Phys. Rev. B **47**, 12727 (1993)
1.12 G. S. Nolas, J. Sharp, H. J. Goldsmid, Thermoelectrics Basic Principles and New Materials Developments (Springer 2001).
1.13 Y. J. Chien, Ph.D thesis, University of Michigan, 2007.
1.14 A. L. Jain, Phys. Rev. **114** 1518 (1959).
1.15 G. E. Smith, R. Wolfe, J. Appl. Phys. **33**, 841 (1962).
1.16 W. M. Yim, A. Amith, Solid-State Electron. **15**, 1141 (1972).
1.17 E. A. Skrabek and D. S. Trimmer, in CRC Handbook of Thermoelectrics, edited by D. M. Rowe (CRC Press, Boca Raton, 1995), p. 267.
1.18 K. F. Hsu, S. Loo, F. Guo, W. Chen, J. S. Dyck, C. Uher, T. Hogan, E. K. Polychroniadis, M. G.. Kanatzidis, Science, **303**, 818 (2004).
1.19 X. Shi, W. Zhang, L. D. Chen, J. Yang, C. Uher, Phys. Rev. B **75**, 235208 (2007).
1.20 C. Uher, in Recent Trends in Thermoelectric Materials Research I, Semiconductors and Semimetals, Vol. **69**, edited by T. M. Tritt (Academic Press, 2001), p. 139-253 and references therein.
1.21 J. Yang, W. Zhang, S. Q. Bai, Z. Mei, L. D. Chen, Appl. Phys. Lett. **90**, 192111 (2007).

Chapter II

Transport Theory in Solids

It is important for us to understand the behavior of electrical and thermal transport in thermoelectric materials in order to select appropriate candidates and optimize their performance. This chapter is a brief review of the theory of transport properties in semiconductors, the class of materials to which most thermoelectric materials belong. The transport theory explains how carriers and phonons affect thermoelectric properties. The aim is to provide some guidance on how we can alter structures to manipulate transport to enhance the thermoelectric performance.

2.1 Transport Equation

The Liouville theorem states the distribution function of particles in an isolated system f is constant for motion along a phase trajectory. The general expression of the transport equation is [2.1]

$$\frac{df}{dt} = \frac{\partial f}{\partial t} + \left[\frac{\partial f}{\partial t}\right]_{\text{ext}} + \left[\frac{\partial f}{\partial t}\right]_{\text{int}} \tag{2.1.1}$$

where the carrier distribution function $f(\boldsymbol{r},\boldsymbol{k},t)$ represents the average number of particles in a state described by the position vector $\boldsymbol{r}$, the wave vector $\boldsymbol{k}$, and the time t. The subscripts "ext" and "int" denote the changes of f under external forces and internal phenomena, respectively. For the interest of our study, we assume that carriers are in steady states. Therefore,

$$\frac{\partial f}{\partial t} = 0 \Rightarrow \left[\frac{\partial f}{\partial t}\right]_{\text{ext}} = -\left[\frac{\partial f}{\partial t}\right]_{\text{int}} \tag{2.1.2}$$

The transport equation for carriers can be written as follows:

$$-\left[\frac{\partial f\left(\vec{r},\vec{k}\right)}{\partial t}\right]_{\text{ext}} = \vec{v}\cdot\nabla_r f + \frac{d\vec{k}}{dt}\cdot\nabla_k f = \left[\frac{\partial f}{\partial t}\right]_{\text{int}} \tag{2.1.3}$$

where $\boldsymbol{v}$ is the velocity of carriers. ∇_r, ∇_k are gradients with respect to position and wave vector, respectively. When the carrier scattering can be described in terms of a relaxation time $\tau\left(\vec{k}\right)$, the term $\left[\frac{\partial f}{\partial t}\right]_{\text{int}}$, known as the collision integral, can be reduced to

$$\left[\frac{\partial f}{\partial t}\right]_{\text{int}} = -\frac{f - f_0}{\tau\left(\vec{k}\right)} \tag{2.1.4}$$

where f_0 and f are the equilibrium and the slightly perturbed (i.e. $\left|f - f_0\right| \ll f_0$) distribution function, respectively. The transport equation in the relaxation time approximation becomes

$$-\frac{f - f_0}{\tau\left(\vec{k}\right)} = \vec{v}\cdot\nabla_{\vec{r}} f + \frac{d\vec{k}}{dt}\cdot\nabla_{\vec{k}} f \tag{2.1.5}$$

Assuming that the conductor is isotropic and the external forces and flows of electricity and heat are in the direction of the x axis, this 3D equation can be simplified into a 1D case. For charge carriers (holes or electrons), we use Fermi distribution function $f_0(E)$. Since $\left|f - f_0\right| \ll f_0$, f can be replaced by f_0 on the right side of Eq. (2.1.5). Therefore, we have

$$\frac{f(E) - f_0(E)}{\tau} = v_x \frac{\partial f_0(E)}{\partial E}\left(\frac{\partial E_f}{\partial x} + \frac{E - E_f}{T}\frac{\partial T}{\partial x}\right);$$

$$f_0(E) = \left[\exp\left(\frac{E - E_f}{k_B T}\right) + 1\right]^{-1} \tag{2.1.6}$$

where v_x is the velocity of the carriers in x direction. This equation applies to both holes and electrons. The electric current density j_x and the heat flow rate per unit cross-section area w_x (carried by carriers) are given by [2.2]

$$j_x = \mp\int_0^\infty e v_x f(E) g(E)\, dE \tag{2.1.7}$$

$$w_x = \int_0^\infty v_x \left(E - E_f\right) f(E)\, g(E)\, dE \tag{2.1.8}$$

where $g(E)$ is the density of state function. For parabolic band structures, which means $E \propto k^2$, $g(E)$ is given by

$$g(E) = \frac{4\pi\left(2m^*\right)^{3/2} E^{1/2} dE}{h^3} \tag{2.1.9}$$

where m^* is the effective mass of a carrier defined in expression

$$\frac{1}{m^*} = \frac{1}{\hbar^2}\frac{d^2E}{dk^2} \tag{2.1.10}$$

Since $j_x = w_x = 0$ when $f = f_0$, one can replace f by $f - f_0$ in Eq. (2.1.7) and (2.1.8). In cases of interest to us, v_x is approximately equal to the thermal velocity. Hence,

$$E = 3\left(\frac{1}{2}m^* v_x^{\,2}\right) \Rightarrow v_x^{\,2} = \frac{2E}{3m^*} \tag{2.1.11}$$

By substituting Eq. (2.1.11) in Eq. (2.1.7) and (2.1.8) and with f replaced by $f - f_0$, we have [2.2]

$$j_x = \mp\frac{2e}{3m^*}\int_0^\infty g(E)\tau E\frac{\partial f_0(E)}{\partial E}\left(\frac{\partial E_f}{\partial x} + \frac{E - E_f}{T}\frac{\partial T}{\partial x}\right)dE \tag{2.1.12}$$

$$w_x = \pm\frac{E_f}{e}j_x + \frac{2}{3m^*}\int_0^\infty g(E)\tau E^2\frac{\partial f_0(E)}{\partial E}\left(\frac{\partial E_f}{\partial x} + \frac{E - E_f}{T}\frac{\partial T}{\partial x}\right)dE \tag{2.1.13}$$

2.2 Electrical Conductivity and Seebeck Coefficient

To calculate the electrical conductivity σ, we consider there is no temperature gradient, i.e. $\partial T / \partial x$ is equal to zero. The electric field ε_x is given by

$$\varepsilon_x = \pm\frac{\partial E_f / \partial x}{e} \tag{2.2.1}$$

Thus, from Eq. (2.1.11) and (2.1.13), the electrical conductivity σ can be derived as

$$\sigma = \frac{j_x}{\varepsilon_x} = -\frac{2e^2}{3m^*}\int_0^\infty g(E)\tau E\frac{\partial f_0(E)}{\partial E}dE \tag{2.2.2}$$

To calculate the expression for the Seebeck coefficient S and thermal conductivity κ, we can set the electric current j_x equal to zero. From (2.1.12), we have

$$\frac{\partial E_f}{\partial x}\int_0^\infty g(E)\tau E\frac{\partial f_0(E)}{\partial E}dE+\frac{1}{T}\frac{\partial T}{\partial x}\int_0^\infty g(E)\tau E\left(E-E_f\right)\frac{\partial f_0(E)}{\partial E}dE=0 \quad (2.2.3)$$

According to the definition of the Seebeck coefficient

$$S=\frac{dV}{dT}=\frac{1}{e}\left(\frac{\partial E_f/\partial x}{\partial T/\partial x}\right) \quad (2.2.4)$$

and Eq. (2.2.3), S is given by

$$S=\pm\frac{1}{eT}\left[E_f-\int_0^\infty g(E)\tau E^2\frac{\partial f_0(E)}{\partial E}dE\Big/\int_0^\infty g(E)\tau E\frac{\partial f_0(E)}{\partial E}dE\right] \quad (2.2.5)$$

The Seebeck coefficient is negative if carriers are electrons, and positive if they are holes. The Peltier coefficient Π can be derived from the Seebeck coefficient using the first Thomson relationship (see Eq. (1.1.4)).

For convenience, we define the following expression as the integral K_s:

$$K_s=-\frac{2T}{3m^*}\int_0^\infty g(E)\tau E^{s+1}\frac{\partial f_0(E)}{\partial E}dE \quad (2.2.6)$$

There may be several scattering processes present with different relaxation times τ. They should all be taken into account, but we assume that one scattering process usually predominates so that the relaxation can be expressed in the form

$$\tau=\tau_0E^r \quad (2.2.7)$$

where τ_0 is a constant, r is another constant, often called the scattering parameter. Inserting (2.1.9) and (2.2.7) in (2.2.6), we may rewrite K_s as

$$\begin{aligned}K_s&=-\frac{8\pi}{3}\left(\frac{2}{h^2}\right)^{3/2}\left(m^*\right)^{1/2}T\tau_0\int_0^\infty E^{s+r+3/2}\frac{\partial f_0(E)}{\partial E}dE\\&=\frac{8\pi}{3}\left(\frac{2}{h^2}\right)^{3/2}\left(m^*\right)^{1/2}T\tau_0\left(s+r+\frac{3}{2}\right)\left(k_BT\right)^{s+r+3/2}F_{s+r+1/2}\end{aligned}$$

where

$$F_n(\zeta)=\int_0^\infty\frac{x^n dx}{\exp(x-\zeta)+1};\quad \zeta=\frac{E_f}{k_BT},\ x=\frac{E}{k_BT} \quad (2.2.8)$$

n can be integers or half-integers. The expression for the electrical conductivity σ in terms of K_s is

$$\sigma = \frac{e^2}{T} K_0 \tag{2.2.9}$$

The expression for the Seebeck coefficient S in terms of K_s is

$$S = \pm \frac{1}{eT}\left(E_f - \frac{K_1}{K_0} \right) = \pm \frac{k_B}{e}\left[\zeta - \frac{(r+5/2)F_{r+3/2}(\zeta)}{(r+3/2)F_{r+1/2}(\zeta)} \right] \tag{2.2.10}$$

where E_f is the Fermi level. For electrons, E_f is measured upward from the bottom of the conduction band. For holes, E_f is measured downward from the top of the valence band. The carrier concentration n is

$$n = \int_0^\infty f(E) g(E)\, dE = \frac{4}{\sqrt{\pi}} \left(\frac{2\pi m^* k_B T}{h^2} \right)^{3/2} F_{1/2}(\zeta) \tag{2.2.11}$$

(A) Non-degenerate condition

The non-degenerate approximation is applicable when $\zeta = E_f / k_B T \ll 0$. This means the Fermi level lies within the band gap well away from the appropriate band edge, but still much further from the opposite band edge so that minority carriers can still be neglected. Experimentally, the Fermi level can be adjusted by changing the carrier concentration in semiconductors.

When $\zeta = E_f / k_B T \ll 0$,

$$F_n(\zeta) \to \int_0^\infty \frac{x^n}{\exp(x-\zeta)} dx = \exp(\zeta)\Gamma(n+1) \tag{2.2.12}$$

where Γ is the gamma function. The Seebeck coefficient of a non-degenerate semiconductor from Eq. (2.2.10) is

$$S = \pm \frac{k_B}{e}\left[\zeta - \left(r + \frac{5}{2} \right) \right] \tag{2.2.13}$$

From Eq. (2.2.11) in (2.2.12), ζ can be written as

$$\zeta = -\ln \frac{2\left(2\pi m^* k_B T\right)^{3/2}}{h^3 n} \tag{2.2.14}$$

Power factor ($S^2\sigma$) is optimized when $\partial(S^2\sigma)/\partial n = 0$, which gives $\zeta = r + 1/2$. Under this condition, the optimum concentration n_0 is

$$n_0 = \frac{2\left(2\pi m^* k_B T\right)^{3/2}}{h^3} \exp\left(r + 1/2\right) \tag{2.2.15}$$

To maximize $S^2\sigma$, the effective mobility $\mu(m^*)^{3/2}$ should be as high as possible.

(B) Degenerate condition

The degenerate condition is satisfied when $\zeta = E_f / k_B T \gg 0$. This means the Fermi level is well above the conduction band edge for electrons or well below the valence band edge for holes. $F_n(\zeta)$ can be expressed in the form of a series:

$$F_n\left(\zeta\right) = \frac{\zeta^{n+1}}{n+1} + n\zeta^{n-1}\frac{\pi^2}{6} + n\left(n-1\right)\left(n-2\right)\zeta^{n-3}\frac{7\pi^4}{360} + \ldots \tag{2.2.16}$$

The higher order terms rapidly converge to zero when $\zeta \gg 0$. Therefore, one can use as many terms in the series as needed to yield nonzero values for the transport coefficients. For the Seebeck coefficient *S*, the first two terms are typically used.

$$S = \mp\frac{\pi^2}{3}\left(\frac{k_B}{e}\right)\frac{r+\frac{3}{2}}{\zeta} \tag{2.2.17}$$

2.3 Thermal Conductivity

Thermal conductivity κ indicates the ability of a material to conduct heat, which is defined as heat *Q* transmitted in time *t* through a distance *L*, in a direction normal to a surface of area *A*, due to a temperature difference ΔT, under steady state conditions and when the heat transfer is dependent only on the temperature gradient. This quantity κ can be expressed as:

$$\kappa = \frac{Q}{t}\frac{L}{A\Delta T} \tag{2.3.1}$$

The transport of heat by any elementary excitations, such as phonons, electrons, photons and etc., can be described by the following equation [2.3]

$$\kappa = \frac{1}{3}C_v v^2 \left\langle \tau \right\rangle \tag{2.3.2}$$

where C_v is the specific heat; v is the velocity of propagation of an elementary excitation and $\langle\tau\rangle$ is its average relaxation time, which is the time taken to travel a mean free path $l\ (=v\langle\tau\rangle)$.

2.3.1 Electronic Thermal Conductivity

The electronic component of the thermal conductivity is an important part, especially in the case of heavily doped semiconductors ($n \sim 10^{19}$-10^{20}cm^{-3}). Before calculating the exact expression of electronic thermal conductivity κ_e and Wiedemann-Franz law, we take a simplified approach to understand the underlying physics. In the case of non-degenerate electron gas, C_v is described by

$$C_v = \frac{3}{2} n k_B \tag{2.3.3}$$

where n is the carrier concentration and k_B is Boltzmann's constant. According to Eq. (2.3.2), we obtain the electronic thermal conductivity

$$\kappa_e = \frac{1}{2} n v^2 k_B \langle\tau\rangle \tag{2.3.4}$$

The electrical conductivity of a semiconductor with a carrier concentration of n is given by

$$\sigma = ne\mu; \quad \mu = \frac{e\langle\tau\rangle}{m^*} \tag{2.3.5}$$

where μ is the carrier mobility; m^* is the effective mass of a carrier. From (2.3.5), we can rewrite κ_e in Eq. (2.3.4) as

$$\kappa_e = \left(\frac{1}{2} m^* v^2\right) \frac{k_B}{e^2} \sigma \tag{2.3.6}$$

The average kinetic energy $\left\langle \frac{1}{2} m^* v^2 \right\rangle$ of carriers is the thermal energy of $3k_BT/2$. Therefore, the electronic thermal conductivity is

$$\kappa_e = \frac{3}{2} \left(\frac{k_B}{e}\right)^2 \sigma T \tag{2.3.7}$$

This approach gives the order of magnitude for the constant, known as Lorenz number L in Wiedemann-Franz Law $\kappa_e = L\sigma T$. It has the order of $\frac{3}{2}\left(\frac{k_B}{e}\right)^2$. The exact form of the electronic thermal conductivity κ_e can be derived from the transport equations in 2.1. When the electric current density j_x is equal to zero, $\kappa_e = -\frac{w}{\left(\frac{\partial T}{\partial x}\right)}$.

From Eq. (2.1.13), κ_e is

$$\kappa_e = \frac{2}{3m^*T}\left\{\frac{\left[\int_0^\infty g(E)\tau E^2 \frac{\partial f_0(E)}{\partial E}dE\right]^2}{\int_0^\infty g(E)\tau E \frac{\partial f_0(E)}{\partial E}dE} - \int_0^\infty g(E)\tau E^3 \frac{\partial f_0(E)}{\partial E}dE\right\}$$
$$= \frac{1}{T^2}\left(K_2 - \frac{K_1^{\,2}}{K_0}\right) \tag{2.3.8}$$

where K_s is defined in Eq. (2.2.6). To describe κ_e in the form of Wiedemann-Franz Law ($\kappa_e = L\sigma T$), from Eq. (2.3.8) and (2.2.8), the Lorenz number L takes the form

$$L = \frac{1}{e^2T^2}\left(\frac{K_2}{K_0} - \frac{K_1^{\,2}}{K_0^{\,2}}\right)$$
$$= \left(\frac{k_B}{e}\right)^2\left\{\frac{\left(r+\frac{7}{2}\right)F_{r+\frac{5}{2}}(\zeta)}{\left(r+\frac{3}{2}\right)F_{r+\frac{1}{2}}(\zeta)} - \left[\frac{\left(r+\frac{5}{2}\right)F_{r+\frac{3}{2}}(\zeta)}{\left(r+\frac{3}{2}\right)F_{r+\frac{1}{2}}(\zeta)}\right]^2\right\}$$

$$\text{where } F_n(\zeta) = \int_0^\infty \frac{x^n dx}{\exp(x-\zeta)+1};\ \zeta = \frac{E_f}{k_BT},\ x = \frac{E}{k_BT} \tag{2.3.9}$$

For non-degenerate samples, the Lorenz number is given by

$$L = \left(r+\frac{5}{2}\right)\left(\frac{k_B}{e}\right)^2 \tag{2.3.10}$$

For strongly degenerate samples, the Lorenz number is a universal constant

$$L = \frac{\pi^2}{3}\left(\frac{k_B}{e}\right)^2 = 2.45\times10^{-8}\,\mathrm{V^2/K^2} \tag{2.3.11}$$

2.3.2 Lattice Thermal Conductivity

Lattice thermal conductivity κ_L is dependent on the phonon specific heat C_{ph}. First, we briefly discuss the methods for the determination of the specific heat of a solid. Fig. 2.1 shows the lattice vibration frequency (ω) as a function of the wave vector (q). Specifically, the vibration spectrum of a 3D lattice has three acoustic modes (2 transverse and 1 longitudinal) and (3n-3) optical modes (n is the number of atoms per primitive unit).

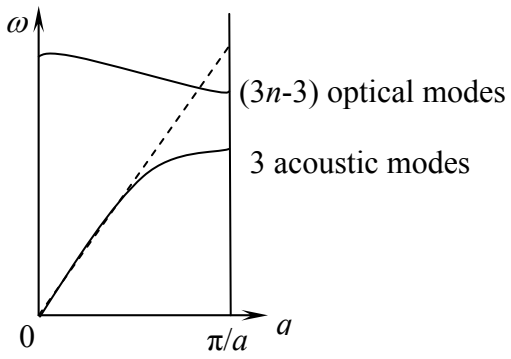

Fig. 2.1. The dependence of lattice vibration frequency on the wave vector (a is the lattice constant).

In the Einstein theory, it is assumed that all the atoms in the lattice vibrate at the same frequency ω, the phonon specific heat C_{ph} can be written as

$$C_{ph} = k_B \frac{x^2 e^x}{\left(e^x - 1\right)^2};\ x = \frac{\hbar\omega}{k_B T} \tag{2.3.12}$$

where $\hbar$ is the Planck constant; k_B is the Boltzmann constant. To consider all the acoustic modes in a solid, a frequency distribution $\rho(\omega)$ in an isotropic elastic continuum was introduced by Debye to replace the single frequency.

$$\int_0^{\omega_{\max}} \rho(\omega)\, d\omega = 3N;\ \ \rho(\omega) = \frac{1}{2\pi^2}\left(\frac{1}{v_l^3} + \frac{2}{v_t^3}\right)\omega^2 \tag{2.3.13}$$

where $\omega_{\max}$ is the maximum vibration frequency; v_l and v_t are the speeds of longitudinal and transverse acoustic modes; N is the number of atoms per unit volume. To simplify the mathematical form, the average speed of sound v_s is defined by

$$\frac{3}{v_s^3} = \frac{1}{v_l^3} + \frac{2}{v_t^2} \tag{2.3.14}$$

Substituting Eq. (2.3.14) into (2.3.13), we solve for $\omega_{\max}$

$$\omega_{\max} = 2\pi v_s \left(\frac{3N}{4\pi}\right)^{1/3} \tag{2.3.15}$$

The specific heat per unit volume can be written as [2.4]

$$\begin{aligned} C_v &= \int_0^{\omega_{\max}} C_{ph}\rho(\omega)\,d\omega \\ &= 9Nk_B\left(\frac{T}{\theta_D}\right)^3 \int_0^{\theta_D/T} \frac{x^4 e^x}{\left(e^x-1\right)^2}\,dx; \quad x = \frac{\hbar\omega}{k_B T} \end{aligned} \tag{2.3.16}$$

where $\theta_D = \dfrac{\hbar\omega_{\max}}{k_B}$, known as the Debye temperature for the acoustic modes. The Debye temperature for the optical modes is defined similarly. At very low temperature ($T \ll \theta_D$), $C_v \propto T^3$; at high temperatures ($T \gg \theta_D$), $C_v \to 3Nk_B$, known as the Dulong-Petit limit.

By applying Eq. (2.3.2), the lattice thermal conductivity κ_L is

$$\begin{aligned} \kappa_L &= \frac{1}{3} v_s^2 \int_0^{\omega_{\max}} \tau_{ph} C_{ph}\rho(\omega)\,d\omega \\ &= \frac{k_B}{2\pi^2 v_s}\left(\frac{k_B T}{\hbar}\right)^3 \int_0^{\theta_D/T} \frac{\tau_{ph} x^4 e^x}{\left(e^x-1\right)^2}\,dx\ ; \quad x = \frac{\hbar\omega}{k_B T} \end{aligned} \tag{2.3.17}$$

where τ_{ph} is the relaxation time. The relaxation time τ_{ph} can be combined as:

$$\tau_{ph}^{-1} = \sum_i \tau_i^{-1} \tag{2.3.18}$$

where i denotes different phonon scattering processes which contribute to thermal resistivity. Phonons may be scattered by grain boundaries, point defects or impurities, and other phonons.

In general, phonon-phonon scattering processes fall into two categories: *N* process and *U* process. *N* process (normal process) is a type of scattering which conserves total lattice momentum:

$$\vec{q}_1 + \vec{q}_2 = \vec{q}_3 \quad \text{or} \quad \vec{q}_1 = \vec{q}_2 + \vec{q}_3 \tag{2.3.19}$$

where $\vec{q}$ denotes the momentum vector. The normal process is shown schematically in Fig. 2.2 (a). In the *N* processes, the direction of the energy flux remains constant. Thus,

this type of phonon-phonon interaction does not contribute to thermal resistivity. *N* processes may affect the lattice thermal conductivity indirectly by redistributing phonon modes. These phonons are then scattered by other processes. The scattering processes which do not conserve total lattice momentum are called *U* processes, often called Umklapp processes:

$$\vec{q}_1 + \vec{q}_2 = \vec{q}_3 + 2\pi\vec{G} \tag{2.3.20}$$

where $\vec{G}$ is the reciprocal lattice vector. The vector $\vec{G}$ "flips" the phonons over to a lower frequency and wave vector $\vec{q}_3$, and reverses the direction of the phonons, therefore producing a resistance to heat flow. This type of scattering gives rise to a finite thermal resistivity.

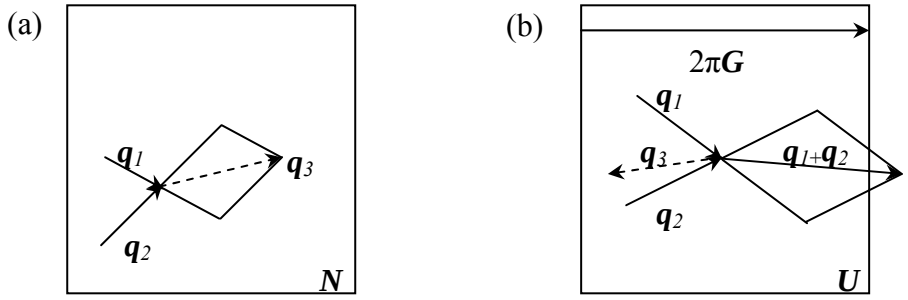

Fig. 2.2. Schematic of (a) *N* process and (b) *U* process scattering

The relaxation rate for *U*-process scattering τ_U^{-1} is [2.5]

$$\tau_U^{-1} = \frac{\hbar\gamma^2}{Mv_s^2}\omega^2\frac{T}{\theta_D}\exp\left(-\frac{\theta_D}{3T}\right) \tag{2.3.21}$$

where M is the average mass per atom, and γ is the Grüneisen parameter. At sufficiently high temperatures (when $T > \theta_D$), if *U*-process dominates, κ_L varies as T^{-1}.

In addition to phonon-phonon interactions, phonons may be scattered by imperfections in the crystal lattice. The boundary scattering rate τ_B^{-1} is [2.6]

$$\tau_B^{-1} = v_s / L \tag{2.3.22}$$

where *L* is the grain size of polycrystalline samples or the dimensions of single crystal samples.

The point defect or impurity scattering rate τ_{PD}^{-1} is [2.7]

$$\tau_{PD}^{-1} = \frac{V}{4\pi v_s^3}\omega^4 \sum_i x_i \left(\frac{M_i - M}{M}\right)^2 \tag{2.3.23}$$

where V is the volume per atom, x_i is the concentration of atoms of mass M_i, M is the average mass per atom. Impurity atoms have different masses (density) and spring constants (elasticity) from the host atoms. Phonons scatter when they encounter a change in acoustic impedance $Z_{acoustic}$, defined as

$$Z_{acoustic} = \sqrt{\rho C} \tag{2.3.24}$$

where ρ is the mass density and C is the elastic stiffness of the chemical bonds. Defects and dislocations disrupt phonon transport in a similar fashion.

Different phonon scattering mechanism may dominate depending on the temperature. The wavelength of dominant phonons is determined by Wien's displacement law [2.8],

$$\lambda_{dom} = \frac{h\nu}{3k_B T} \tag{2.3.25}$$

where k_B is Boltzmann's constant, and h is Planck's constant. As the temperature increases, the phonon wavelength decreases. When the phonon wavelength becomes comparable to the size of the defects, defect scattering becomes the dominant scattering mechanism. Alloys have considerable amount of defects and therefore defect scattering may dominate over much of the temperature range. For a further increase in temperature, the phonon wavelength continues to decrease and eventually the wave vectors become large enough for Umklapp processes to dominate.

References to Chapter II

2.1 I. M. Tsidil'kovskii: Thermomagnetic Effects in Semiconductors, translated by A. Tybulewicz, edited by H. J. Goldsmid (Infosearch, London, 1962)
2.2 G. S. Nolas, J. Sharp, H. J. Goldsmid: Thermoelectrics Basic Principles and New Materials Developments (Springer 2001)
2.3 N. W. Ashcroft, N. D. Mermin: Solid State Physics (W.B. Saunders, Philadelphia, 1976)
2.4 H. J. Goldsmid: Electronic Refrigeration (Pion Limited, London, 1986)
2.5 G. A. Slack, S. Galginaitis, Phys. Rev. **133**, A253 (1964)
2.6 M. Omini, A. Sparavigna, Phys. Rev. B, **61**, 6677 (2000)
2.7 R. Berman: Thermal Conduction in Solids (Clarendon Press, Oxford, 1976)
2.8 C. L. Tien, A. Majumdar, F. M. Gerner: Microscale Energy Transport (Taylor and Francis 1998)

Chapter III

Experimental Techniques

3.1 Material Synthesis

Bulk thermoelectric specimens are mostly prepared through solid state reactions at high temperatures. Pure chemical elements (typically of 99.99% or 99.999% purity) are mixed based on their stoichiometric compositions. Active reactants need to be weighed inside a glove box filled with inert gases. The mixture of materials is placed in a quartz ampoule and sealed under vacuum which eliminates oxygen. This prevents possible oxidation during chemical reaction at high temperatures.

For reactions involving elements of very high melting point (above 1200^{o}C), arc melting is more appropriate than solid state reaction. The mixed materials are placed in the cup of a copper hearth. The hearth is inserted into the tapered hole at the bottom of a furnace and clamped into position. The furnace cavity is purged by a mechanical pump, followed by backfilling with inert gases such as argon or helium. Once the system is purged and the desired power setting on the power supply is set, the electrodes are brought to a position near the edge of materials to be melted and an arc is struck. For our experiments, it is preferable to melt a small piece of titanium prior to melting the specimen, as the gettering action of titanium removes possible impurity from the furnace cavity. The specimen is often turned over and remelted for a few times in order to achieve homogeneity.

Chemical reaction is followed by annealing in order to form stable single phase solid solutions. After annealing, specimens are cut into pieces of different size for measurement purposes. For specific compounds like skutterudites, additional material processing is performed after annealing. For example, spark plasma sintering (SPS) can be used to condense the powders and further remove impurity phases to enhance the mechanical and thermoelectric properties.

3.2 Chemical and Structural Analysis

3.2.1 X-ray Powder Diffraction (XRD)

For X-ray measurements, pieces cut from specimens are first crushed into small chunks and then ground into fine powder using an agate mortar and pestle. The powder is pressed between two glass slides to form a uniform thin layer. The glass slide with the powder layer on top is loaded into Scintag diffractometer for 2θ scan. The X-ray tube utilizes Cu Kα radiation (wavelength: 1.540562Å). The continuous scan mode was selected with the scan rate of 2 deg/min. The measured XRD pattern is compared to the available diffraction patterns of the same crystal structure to check if the specimen is single phase.

3.2.2 Electron Microprobe Analysis

X-ray powder diffraction is effective in terms of identifying the single phase on a macroscopic scale. To confirm the single phase locally and determine the actual chemical composition on a microscopic scale, we need electron microprobe analysis (EPMA). For our polycrystalline samples, the average grain size is approximately 50 μm, which is large enough to resolve with EPMA. A thin slice of sample is cut and polished for such an analysis. A number of positions are selected on the EPMA images to analyze the chemical composition.

3.3 Low Temperature Property Measurements: longitudinal stead-state method

Electrical conductivity σ, thermopower S and thermal conductivity κ are measured simultaneously by the four-probe longitudinal steady-state technique using a liquid He^4 cryostat. Samples are cut with a low speed diamond wheel saw in a parallelepiped shape with heat flow along the longitudinal axis. Samples are mounted on the cryostat and protected from excessive radiation loss by two radiation shields. Fig. 3.1 is a schematic diagram of the typical sample mounting.

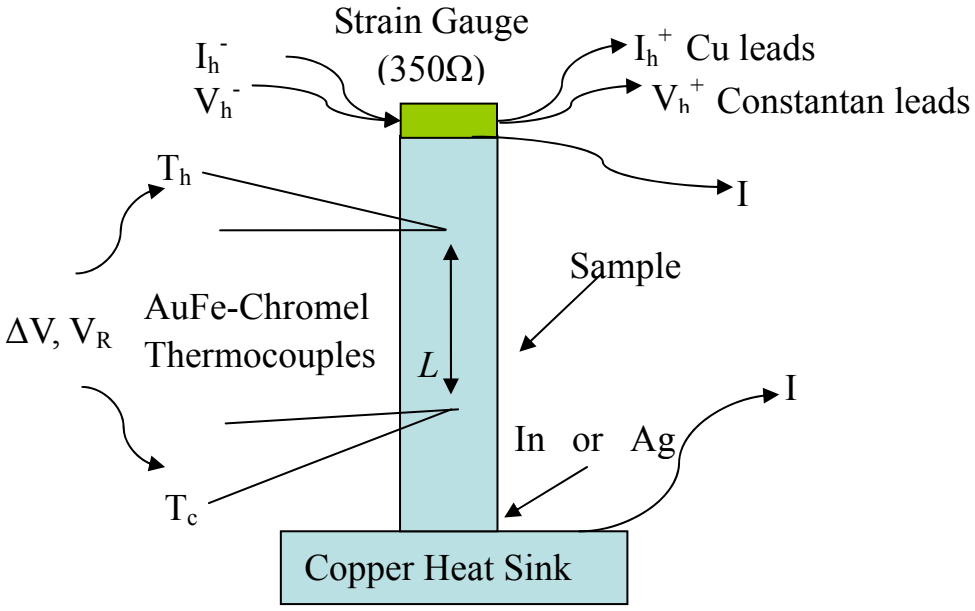

Fig. 3.1. Sample mounting for low temperature measurements

One end of the sample is attached to a heat sink by indium solder, silver paste/epoxy, or clamping, depending on whether indium wets the material and the thickness of the sample. The heat sink is the cold tip of the liquid helium cryostat, the temperature of which is adjusted using a Lakeshore 340 temperature controller. Heat input to the sample is made via a small strain gauge heater with 350 Ω resistance attached to the free end of the sample using varnish. For a given current I and voltage V across the heater, the power P_h (= IV) is generated by the heater. The temperatures of two contact points, separated by a distance L along the sample, are measured by AuFe-Chromel thermocouples. The heat flow injected by the heater develops a temperature difference ΔT between the two points along its length. Fine copper (Cu) wires are selected as Seebeck / resistive probes because of the low resistivity and small thermopower of copper. The contribution of copper's thermopower is subtracted out from a combined measurement of both sample and Cu leads. For small temperature differences ($\Delta T \le 0.05 \left(T_h + T_c\right)/2$ in our experiments), the total thermal conductivity at the average temperature $T_{av} (=\left(T_h + T_c\right)/2)$ can be written as

$$\kappa = \frac{P_h}{\Delta T} \cdot \frac{L}{A} \tag{3.3.1}$$

where A is the cross section area of the sample. Heat may be lost by radiation to the surroundings; conduction and convection between the surroundings and the sample; and conduction through wires attached to the sample. To prevent conduction and convection via surroundings, the sample is enclosed in a can which can be evacuated by a diffusion pump to a pressure of less than 10^{-7} Torr. Conduction via leads can be greatly reduced by using long and very fine wires of low thermal conductivity. To minimize the thermal resistance between the sample and the heat sink, the sample is usually attached to the heat sink using low-melting point solder. Radiation loss can be minimized by surrounding the sample with a copper shield thermally grounded to the heat sink, although it cannot be totally eliminated. Radiation loss (P_{rad}) is experimentally determined near room temperature in a subsequent measurement where the sample is detached from the heat sink and suspended by its connecting leads under vacuum. According to the Stefan's law, the radiation loss between the surrounding and the sample is [3.1]

$$P_{rad} \propto T_{av}^4 - T_s^4 \tag{3.3.2}$$

where T_{av} is the average temperature of the sample and T_s is the temperature of the surrounding. Given the fact that the difference between T_{av} and T_s is very small compared to T_s, Eq. (3.3.2) is approximated to be

$$P_{rad} \propto T_s^3 \cdot \Delta T \tag{3.3.3}$$

From the above relation, the portion of radiation (P_{rad}/P) can be calculated at each temperature of interest. Thermal conductivity is computed by subtracting the portion of radiation from the measurement in the entire temperature range. Radiation loss is insignificant below about 100 K for most thermoelectric samples.

3.4 High Temperature (above 300*K*) Property Measurements

3.4.1 Seebeck Coefficient

The Seebeck coefficient S, also called thermopower, is related to the electronic structure. The sign of the Seebeck coefficient indicates the dominant charge carrier type in general.

p-type materials have positive *S* whereas *n*-type materials have negative *S*. In our laboratory, the Seebeck coefficient *S* is measured by a home-built apparatus along with electrical conductivity σ at high temperatures [3.2-3.4]. Fig. 3.2 is a diagram of the experimental setup for Seebeck coefficient measurement. *S* is given by

$$S_{sample} = \frac{V_c - V_h}{\Delta T} + S_{lead} \tag{3.4.1}$$

where S_{lead} and S_{sample} are the Seebeck coefficient of lead wires and that of the sample, respectively. ΔT is the imposed temperature gradient along the sample.

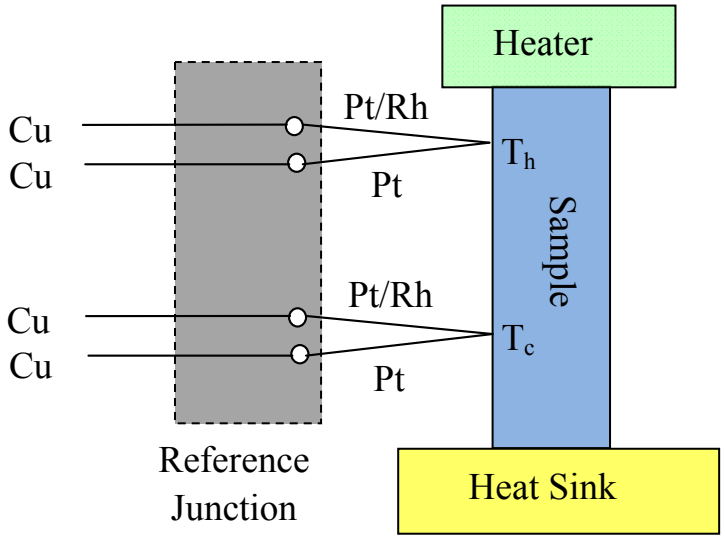

Fig. 3.2. Experimental setup for the Seebeck coefficient measurement at high temperatures

The technique used for measuring the Seebeck coefficient over a wide range of temperatures is to apply an appropriate temperature gradient ΔT across the sample and slowly vary the sample temperature *T*. The Seebeck coefficient, at each temperature of interest, is determined by sweeping a temperature gradient, ΔT, and measuring the corresponding Seebeck voltage, $\Delta V(=V_c-V_h)$. The slope of the line, $\Delta V/\Delta T$, extracted based on the best linear fit, yields S_{sample}-S_{lead}. For metals widely used for high temperature applications such as Cu, Ag, Au, Pt etc, the Seebeck coefficient data can be found in the literature [3.5].

R-type Pt vs Pt-Rh thermocouple is best known for its exceptional stability at high temperatures. Thus, it is a natural choice for measurements at high temperatures. Similar to the low temperature setup, Pt leg of the Pt vs Pt-Rh thermocouple is also used as the lead wire to pick up the resistive voltage of the sample. In this case, one needs a conducting adhesive which not only provides good thermal contact but also has low contact resistance. Through numerous trials, silver paste made by Ted-Pella Inc. is proven to be a good candidate. In regard to the reference junction, an Omega ice point chamber is capable of maintaining the temperature precisely at 0°C to within ±0.1°C. In theory, there should be little difference between measurements taken under vacuum and in an inert gas atmosphere. In practice, the percentage of Pt content in Pt-Rh thermocouple will change when the thermocouple is exposed to high temperature under vacuum condition. To prevent such a deteriorating effect and the formation of oxide layers on sample surfaces, the Seebeck measurement is taken under argon flow in our laboratory. Voltage signals (usually in the μV range) are measured by Keithley nano-voltmeters. Data collection and analysis process is automated by LabVIEW. The algorithm is discussed in 3.6 of this chapter.

3.4.2 Electrical Conductivity

The four-probe method is used to measure the electrical conductivity at high temperatures. Two copper leads inject the current through large-area ohmic contacts at the ends of a bar-shaped sample. As mentioned in 3.4.1, the resistive voltage along the longitudinal direction of the sample is measured using the Pt leg of the Pt vs Pt-Rh thermocouple. The voltage probes are held in place by small area contact using silver paint. The four probe configuration eliminates the contribution of lead wires and effects associated with contact resistance. To reduce error related to sample geometry, the typical size of a bar sample is 2-3mm for the width and thickness, and 10-12mm for the total length. To ensure uniform current flow through voltage probes, voltage leads should be positioned away from current leads. It is suggested to use sufficiently long samples.

There are some additional concerns that are related to the thermoelectric nature of the materials. Excessive Joule heating can impose unwanted thermal gradients ΔT across the

sample. Because of the large Seebeck coefficient S of thermoelectric materials, the induced Seebeck voltage $V_{Seebeck}$ is superposed on the resistive voltage V_I. In order to subtract and minimize $V_{Seebeck}$, the current flow should be reversed fast and data taken as the average of the two readings (see Eq. (3.4.2)).

$$V_R = \frac{1}{2}\left[(V_{(I+)} + V_{Seebeck}) - (V_{(I-)} + V_{Seebeck})\right];$$
$$V_{Seebeck} = S\Delta T \tag{3.4.2}$$

Moreover, ΔT is also generated by the Peltier effect at the current contacts. The Peltier effect (i.e. liberation or absorption of heat) occurs at the junction between two dissimilar materials, which in our case are the sample and the current leads in the setup, when applying current. Because the Peltier effect is linear in current, current reversal changes the sign of both the resistive voltage and the Peltier effect, which results in an increase in the actual resistive voltage. Since it takes a finite time to establish the thermal gradient due to the Peltier heat, one can deal with this Peltier contribution by switching the current polarity before the thermal gradient has time to build up. Fast pace data collection is among the many advantages automatic measurements offer. To eliminate error as much as possible, electrical conductivity is calculated from multiple measurements at different currents in both directions.

3.4.3 Thermal Conductivity

Radiation heat losses at and above the room temperature (300 K) are too large to make use of the steady-state longitudinal technique. Consequently, alternative methods of measurement must be used. The technique most favored to determine the thermal conductivity of bulk samples above room temperature is the laser flash thermal diffusivity – specific heat capacity method [3.6]. For this measurement, thin discs are cut from bulk samples. The typical thickness ranges from 1mm to 2mm. In this technique, one surface of a disc-shaped sample is irradiated by a short neodymium-glass laser pulse with an average duration of 300 μs. The temperature rise of the opposite side of the sample is recorded by an infrared InSb detector. The transient time of the heat through the

sample is much larger compared to the duration of the laser pulse. Both sample surfaces are coated with graphite to make them highly absorptive and emissive. This thin layer of graphite coating maximizes the thermal energy absorbed by the front surface and transmitted from the front surface to the rear surface, therefore the signal collected by the infrared detector. The thermal diffusivity α is calculated from the thermogram, which is the profile of the temperature rise versus time. Using the relation

$$\kappa = \rho C_p \alpha \tag{3.4.3}$$

where ρ is sample density and C_p is specific heat capacity. For solids, $C_p = C_v$. This technique can be used to determine thermal conductivity (κ) above room temperature. In our laboratory, thermal diffusivity α is measured using laser-flash system (Anter Flashline5000).

C_p is independently measured by a differential scanning calorimeter (Netzsch DSC 404C) using the ratio method. The sample holder for C_p measurement is made of platinum-rhodium with alumina lining, which prevents platinum alloying with metallic elements in the sample at high temperatures. The background signal of sample holder is subtracted from the combined signal when the sample is measured. C_p of a sample is computed from the ratio of the corrected signal of the sample to that of a standard with known C_p. For our measurements, the most frequently used standard is sapphire. Density ρ is defined as the ratio of m/V where m is the mass and V is the volume. m can be weighed directly by a scale. V can be calculated from the geometric dimensions or measured by applying Archimedes' principle.

3.5 Magnetic Property Measurements

The power factor $S^2\sigma$ of a thermoelectric material is typically optimized around carrier concentration in the range of 10^{17}-10^{20}cm^{-3}. For a given carrier concentration, carrier mobility should be large for good thermoelectric materials. Therefore, it is important to determine the carrier concentration and mobility in order to fully characterize a thermoelectric material. For semiconductors of single carrier type, both properties can be determined experimentally by Hall effect measurements.

The electrical resistivity and Hall effect were measured by a Linear Research AC bridge with 16 Hz (low frequency) excitation in a cryostat equipped with a superconducting magnet capable of fields up to 5 Tesla. Compared to a DC measurement, the AC method is more applicable because it has fewer corrections due to magneto-thermoelectric effect. A rectangular thin slab with an average size of 2mm x 1mm x 5mm is cut from the ingots for the Hall measurements. Fig. 3.3 shows the experimental setup.

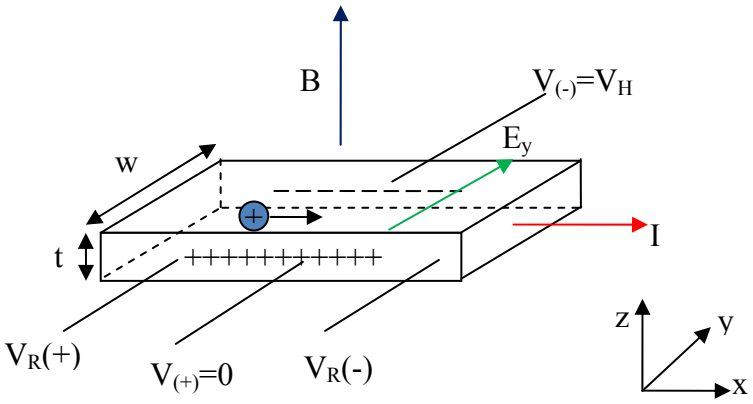

Fig. 3.3. Schematic of the Hall effect measurement

Charge carriers in a magnetic field B_z are subject to the Lorentz force $F_{Lorentz}$, given by

$$\vec{F}_{Lorentz} = q(\vec{v}_x \times \vec{B}_z) \tag{3.5.1}$$

where q is the charge of a carrier, and v_x is the velocity of carriers. Due to the Lorentz force, charge carriers deflect to one side of the slab (x-z plane), forming a transverse electric field E_y which opposes further deflection and accumulation. At the steady state, the electric force $F_{electric}$ (= qE_y) counterbalances the Lorentz force $F_{Lorentz}$, so enabling the continuous current flow as before. The required electric field E_y is

$$E_y = v_x B_z \tag{3.5.2}$$

For p-type carriers, the relationship between current density j_x and velocity v_x is

$$j_x = n_c q v_x \tag{3.5.3}$$

where n_c is the carrier concentration. Hence, we obtain

$$E_y = \frac{j_x}{n_c q} B_z \tag{3.5.4}$$

The Hall coefficient R_H is defined by the equation

$$E_y = R_H j_x B_z \tag{3.5.5}$$

Comparing (3.5.4) with (3.5.5), the Hall coefficient for *p*-type conduction is given by

$$R_H = \frac{1}{n_c q} \tag{3.5.6}$$

Eq. (3.5.6) is valid for metals and strongly degenerate semiconductors because the carriers occupy a narrow energy range in the order of k_BT around the Fermi level. Therefore, all carriers have nearly the same velocity and they will be deflected in a given magnetic field by approximately the same amount. For non-degenerate semiconductors, the carriers do not have the same velocities and they will be deflected in a magnetic field by different amounts. The correction can be accounted for by multiplying a constant A on the right hand side of Eq. (3.5.6). However, A is usually close to unity.

From (3.5.5), the transverse Hall voltage V_H is

$$V_H = wE_y = w(R_H j_x B_z) = R_H I_x B_z / t \tag{3.5.7}$$

where w and t are the width and thickness of the sample (Fig. 3.3). In Eq. (3.5.7), the ratio of V_H / I_x has the unit of resistance, measured by an AC bridge. From the relation (3.5.6), the carrier density n_c can be derived given R_{H}. Inserting (3.5.4) into Ohm's law $j_x = \sigma \cdot E_x$,

$$\sigma = n_c q \frac{v_x}{E_x} = n_c q \mu \tag{3.5.8}$$

μ is carrier drift velocity per unit electric field, also called carrier mobility. μ is independent of E within the validity of Ohm's law. Combined measurements of electrical conductivity σ and Hall coefficient R_H yields the mobility μ:

$$\mu = \left|R_H\right| \sigma \tag{3.5.9}$$

μ is positive regardless of the sign of R_H. Large values of mobility (μ) are desired for good thermoelectric materials.

If more than one type of carrier contributes to conduction, we need to treat the steady state as arising from the equality of currents instead of forces. The deflected current generated by magnetic field is balanced by the current due to the transverse electric field. For mixed conduction of holes (p) and electrons (n), a general expression of R_H valid for arbitrary magnetic fields B is [3.7]

$$R_H = -\frac{1}{q} \cdot \frac{\left(n\mu_n^2 - p\mu_p^2\right) + \mu_n^2 \mu_p^2 \left(n-p\right) B^2}{\left(n\mu_n + p\mu_p\right)^2 + \mu_n^2 \mu_p^2 \left(n-p\right)^2 B^2} \tag{3.5.10}$$

More information is needed in order to solve for the unknown quantities n, p, μ_n, μ_p individually.

3.6 Automation of High Temperature Apparatus

The high temperature measurement system is interfaced to a computer and the automatic data collection is enabled by a program coded in LabVIEW. This program communicates with the measurement instruments including three Keithley nanovolt meters and one DC power supply via GPIB interface. To verify the stability of the sample at high temperatures, a complete heating and cooling cycle should be selected for measurements. In addition to collecting numerical raw data, the program analyzes these data using resourceful mathematical packages in LabVIEW. The program stores analyzed electrical conductivity, Seebeck coefficient, and temperature of samples in data files. Other experimental parameters such as temperature gradient, current, and voltage are also recorded for reference.

3.6.1 Electrical Conductivity

The sample temperature T is considered to be the average of the two temperature readings measured by thermocouples. At each temperature of interest, multiple voltages V_R are taken by applying currents I_R that are increased by predetermined amounts set by users. The current is reversed before being increased at the next higher value. Users can also choose how short an interval they desire between the changes in the current. Two arrays of current I_R and voltage V_R are generated. Electrical resistance R is calculated from the linear fit function of V_R/I_R. R is converted to electrical conductivity σ from the relation $\sigma = l/(RA)$, where l is the distance between two resistive voltage probes and A is the cross-sectional area of sample. These geometric parameters are entered by users for analysis purposes, prior to the measurements.

3.6.2 Seebeck Coefficient

By pulsing the sample heater for an arbitrarily set time (~ a few minutes), the temperature gradient ΔT along the longitudinal direction of the sample continues to rise before it reaches a stable value which is recorded in the data file. Multiple values of Seebeck voltage ΔV and temperature gradient ΔT are stored in separate 1D arrays following the same order. According to the definition of Seebeck coefficient $S = \Delta V / \Delta T$, S is calculated by the linear fit function in LabVIEW. During the pulse period, the temperature of the sample increases by a small amount. To take this increase into consideration, the temperature of sample T is computed as the mean of the initial temperature and final temperature during the heating. To maintain a reasonable temperature gradient (~5%-10% of temperature of sample), the heater power is adjusted accordingly after one complete sequence of measurements. The measured Seebeck coefficient $S_{measured}$ is a superposition of the sample S_{sample} and the Pt Seebeck probe S_{Pt}. The Seebeck data for Pt were obtained from the literature for calibration over the temperature range [3.5].

Reference to Chapter III

3.1 T. M. Tritt, V. M. Browning, in Recent Trends in Thermoelectric Materials Research I, Semiconductors and Semimetals, Vol. **69**, edited by T. M. Tritt (Academic Press, San Diego, 2001), p. 25-49 and references therein
3.2 Z. Zhou, C. Uher, Rev. Sci. Instrum. **76**, 023901 (2005)
3.3 H. Kong, X. Shi, C. Uher, D. T. Morelli, J. Appl. Phys. **102**, 023702 (2007)
3.4 X. Shi, H. Kong, C. Li, C. Uher, J. Yang, J. R. Salvador, H. Wang, L. Chen, W. Zhang, Appl. Phy. Lett. **92**, 182101 (2008)
3.5 F. J. Blatt, P. A. Shroeder, C. L. Foiles, D. Greig: Thermoelectric Power of Metals (Plenum Press, New York, 1976)
3.6 R. Taylor, in CRC Handbook of Thermoelectrics, edited by D. M. Rowe (CRC Press, Boca Raton, 1995), p. 165-180 and references therein
3.7 E. H. Putley: The Hall Effect and Related Phenomena (Butterworths, London, 1960)

Chapter IV
Lead Chalcogenides

Lead chalcogenides are a group of semiconductors consisting of lead and elements of group VI (sulfur, selenium and tellurium in particular). Lead chalcogenides share many physical and chemical properties in common. They are isostructural, i.e. have the same crystal structure. They can be prepared and doped by similar methods. Some lead chalcogenide alloys, such as lead telluride and lead selenide, are established as good thermoelectrics. Atomic substitution in alloys can effectively scatter the short wavelength phonons, thereby significantly reducing the thermal conductivity up to the "alloy limit". It has been difficult to beat the alloy limit without creating excessive defects, dislocations, and voids, which decrease electrical conductivity, making it ineffective for increasing the material's thermoelectric figure-of-merit (ZT). Larger size impurities like nanoparticles can effectively scatter mid- and long wavelength phonons, resulting in a broader scattering spectrum and consequently, further reduction in the lattice thermal conductivity. In this chapter we demonstrate that nanoparticles embedded in lead chalcogenide-based alloys indeed reduce thermal conductivity significantly while maintaining good electrical transport. Much higher thermoelectric figure-of-merit is achieved in these nano-structured materials. The lead chalcogenide-based systems discussed in this chapter include $Pb_{9.6}Sb_{0.2}Te_{10-x}Se_x$ (where x = 0, 1, 2, 3, 4, 5, 6, 7, 8, 9, 10) with highest ZT of 1.2 at 650 K for x = 7, PbTe-x%M (where M = Bi, Sb, InSb and $2 \leq x \leq 16$) with lowest κ_L of 0.8 $Wm^{-1}K^{-1}$ for M = Sb and x = 2 at 300 K, $(Pb_{0.95}Sn_{0.05}Te)_{1-x}(PbS)_x$ (where x = 0.04, 0.08, 0.16) with highest ZT of 1.50 at 642 K for x = 0.08, and PbTe-x%Eu (where x = 0.5, 1, 2, 3) with moderate ZT of ~0.6.

4.1 Crystalline Structure

Lead chalcogenides form cubic sodium chloride (NaCl) lattice structure which belongs to $Fm\bar{3}m$ space group. As shown in Fig. 4.1, each Pb (Te) atom is surrounded by six Te (Pb) atoms. The Pb (Te) sublattice is of the face-centered cubic type. The structure is isotropic. Therefore, thermoelectric properties are the same in all directions.

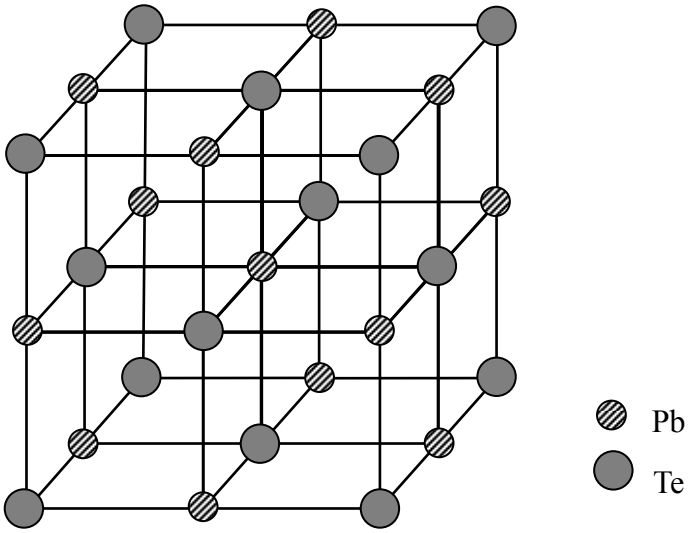

Fig. 4.1. Crystalline structure of PbTe.

Lead chalcogenides appear opaque and have a metallic luster. They are brittle and easily cleave along (100) plane. Wire saw is preferred for cutting PbTe-like ingots. The chemical binding in lead chalcogenides has both ionic and covalent components [4.1].

4.2 Carrier Scattering Mechanisms

Carriers in lead chalcogenides are in principle scattered by acoustic and optical phonons, by other carriers, and by impurities. The dominant scattering centers for carriers are point defects and thermal phonons. At very low temperatures, of the order of the liquid-helium temperatures, charge carriers are scattered predominantly by ionized impurities and charged vacancies. In the lightly-doped samples (i.e. carrier concentration n is on the order of 10^{18} cm^{-3} and lower), carriers are scattered by the Coulomb potential of charged

vacancies. In the heavily-doped samples (i.e. carrier concentration n is on the order of 10^{19} cm^{-3} and higher), the Coulomb potential is screened out and the short range potential of vacancies dominates. As the temperature increases, the influence of the charged vacancies weakens, and scattering by thermal phonons becomes dominant. Above Debye temperatures θ_D (θ_D > 300 K for PbTe and PbSe, and θ_D > 600 K for PbS), scattering by the deformation potential of acoustic phonons and polarization scattering by optical phonons are the most important contributions. The influence of acoustic phonon scattering gradually increases with the temperature. The scattering of acoustic phonons becomes dominant at higher temperatures where lead chalcogenides have their optimal thermoelectric performance.

4.3 Phonon Scattering Mechanisms

Recent experimental results have shown that nanostructuring thermoelectric materials can significantly reduce the thermal conductivity, while its effect on the electrical conductivity is minimal. As a result, ZT increases. In theory, embedded nanoparticles not only enhance boundary and interface scattering, but also provide additional scattering mechanism for the mid to long wavelength phonons. A simple expression for scattering cross section σ was proposed in Ref. [4.2]:

$$\sigma = \pi R^2 \left(\frac{\chi^4}{\chi^4 + 1} \right) \tag{4.3.1}$$

where R is the radius of a spherical scattering particle, and χ is the size parameter, defined as $\chi = 2\pi R/\lambda$, where λ is the phonon wavelength. When the size parameter χ approaches zero, the scattering cross section obeys the Rayleigh law. Therefore, in the Rayleigh scattering regime, the scattering cross section σ varies as:

$$\sigma \sim R^6/\lambda^4 \tag{4.3.2}$$

For atomic substitutions in alloys, R is on the scale of atomic size (Å). The above relation suggests that short-wavelength phonons are scattered much more effectively than the mid- and long-wavelength phonons for atomic-scale defects. By introducing nanometer-sized particles in the lattice medium, the mid- and long-wavelength phonons are also scattered; thus, the phonon scattering spectrum is extended. Consequently, the thermal

conductivity can be reduced below the alloy limit. Significant advances have been made to reduce the lattice thermal conductivity of PbTe-based alloys. Results of our studies on these materials have been published in several journal papers.

4.4 Transport Theory in PbTe

For the conduction and valence bands in PbTe, the Fermi surfaces are ellipsoids. The non-parabolic Kane's band model is introduced to describe the energy dispersion relation E vs k [4.3]

$$E\left(1+\frac{E}{E_g}\right)=\gamma(E)=\frac{\hbar^2}{2}\left(\frac{2k_t^2}{m_t^*}+\frac{k_l^2}{m_l^*}\right) \tag{4.4.1}$$

where E_g is the direct energy gap of PbTe, and k and m^* are the wavevector and effective mass (at $k = 0$) along the longitudinal (l) and transverse (t) direction of the ellipsoids. In the modified Kane model, the effective masses and the mass anisotropy coefficient of electrons and holes are equal. The constant energy surfaces are ellipsoids, and m_l^* and m_t^* have the same energy dependence. The density of states $g(E)$ is

$$g(E)=\frac{\sqrt{2}\left(m_d^*\right)^{3/2}}{\pi^2\hbar^3}\gamma'\sqrt{\gamma(E)} \tag{4.4.2}$$

where $\gamma'=\frac{d\gamma(E)}{dE}$; the density of states effective mass m_d^* is defined by the following expression in the multi-valley (many-ellipsoid) model ($N>1$):

$$m_d^*=N^{2/3}\left(m_t^{*2}m_l^*\right)^{1/3} \tag{4.4.3}$$

where N is the degree of degeneracy. For parabolic bands, the expression for the carrier scattering relaxation time τ is

$$\tau=\tau_0E^r \tag{4.4.4}$$

where r is the scattering parameter. r =-1/2 for carrier scattering by acoustic phonons; r =3/2 for scattering by ionized impurities. The density of state $g(E)\propto E^{1/2}$.

For non-parabolic bands in PbTe, the energy dependence of τ is given by [4.4]

$$\tau = \tau_0 \frac{\gamma(E)^r}{\gamma'(E)} \tag{4.4.5}$$

From the transport theory in Chapter II, the carrier concentration n is

$$n = \frac{\left(2m_d^* k_B T\right)^{3/2}}{3\pi^2\hbar^3} \int_0^\infty \gamma(\zeta)^{3/2} \left(-\frac{\partial f_0}{\partial \zeta}\right) d\zeta \tag{4.4.6}$$

where $\zeta = E/k_BT$, and f_0 is the Fermi-Dirac distribution function, i.e. $f_0=1/[1+\exp(E-E_f)/k_BT]$. The electrical conductivity σ is

$$\sigma = \frac{\left(2m_d^* k_B T\right)^{3/2}}{3\pi^2\hbar^3} \frac{e^2}{m_\alpha^*} \int_0^\infty \frac{\gamma(\zeta)^{3/2}}{\gamma'(\zeta)} \tau(\zeta) \left(-\frac{\partial f_0}{\partial \zeta}\right) d\zeta \tag{4.4.7}$$

where m_α* is the effective mass along the crystallographic direction of the sample studied, or the appropriate average mass for polycrystals, and $\gamma'(\zeta) = \frac{d\gamma(\zeta)}{d\zeta}$.

The Seebeck coefficient S is

$$S = \frac{k_B}{e} \left[\frac{\int_0^\infty \frac{\gamma(\zeta)^{3/2}}{\gamma'(\zeta)} \zeta\tau(\zeta) \left(-\frac{\partial f_0}{\partial \zeta}\right) d\zeta}{\int_0^\infty \frac{\gamma(\zeta)^{3/2}}{\gamma'(\zeta)} \tau(\zeta) \left(-\frac{\partial f_0}{\partial \zeta}\right) d\zeta} - \frac{E_f}{k_B T} \right] \tag{4.4.8}$$

In the low field limit (μB«1), the Hall coefficient R_H is:

$$R_H = \frac{A_K}{ne} \frac{\left[\int_0^\infty \frac{\gamma(\zeta)^{3/2}}{\left(\gamma'(\zeta)\right)^2} \tau^2(\zeta) \left(-\frac{\partial f_0}{\partial \zeta}\right) d\zeta\right] \left[\int_0^\infty \gamma(\zeta)^{3/2} \left(-\frac{\partial f_0}{\partial \zeta}\right) d\zeta\right]}{\left[\left[\int_0^\infty \frac{\gamma(\zeta)^{3/2}}{\gamma'(\zeta)} \tau(\zeta) \left(-\frac{\partial f_0}{\partial \zeta}\right) d\zeta\right]\right]^2} \tag{4.4.9}$$

where the anisotropy factor $A_K = \frac{3K(K+2)}{(2K+1)^2}$ and the effective mass anisotropy coefficient $K = m_l^*/m_t^*$.

4.5 Established Nano-structured Bulk Lead Chalcogenides

In recent years, both *n*-type and *p*-type lead chalcogenides have been developed for thermoelectric applications in the intermediate temperature range of 600 K to 900 K. A

leading candidate among *n*-type chalcogenides is $(PbTe)_m$-$AgSbTe_2$, often abbreviated as LAST ((lead, antimony, silver, tellurium)-*m* system. On average, these quaternary compounds adopt the same structure as bulk PbTe. These compounds are not solid solutions but unique heterogeneously nano-structured systems. High resolution TEM images exhibit Ag-Sb rich nanostructures embedded in the PbTe lattice [4.5].These nanostructures in the PbTe lattice are considered to be responsible for reducing the thermal conductivity remarkably, through interface and mid-to-long wavelength phonon scattering.

The existence of Ag-Sb clusters could be justified by the coulomb interaction. In a simple ionic model, we can assume the Pb ion to have the valence 2+, Te ion 2−, Ag ion 1+, and Sb ion 3+. In the Pb sublattice, two Pb ions can be replaced by one Ag ion and one Sb ion. Therefore, we can assign effective valence states of −1, +1 and 0 to Ag, Sb, and Pb ions, respectively. The Coulomb attraction between +1 and −1 charges drives the Ag and Sb ions to come together and form clusters. In agreement with the microscopic images, theoretical calculations show that a typical low temperature structure of $(PbTe)_m$-$AgSbTe_2$ is a self-assembled nanostructure with layers of $AgSbTe_2$ arranged in a particular fashion in the PbTe lattice [4.6]. Specifically, these micro-structural arrangements of Ag-Sb in PbTe show a common feature: when Sb replaces Pb, Sb *p* states hybridize with Te *p* states, forming strong covalent bonding. These states are resonant with the PbTe conduction band (CB) and extend into the PbTe band gap. When Ag replaces Pb, the *p* states of Te atoms which are the nearest neighbors of Ag are strongly perturbed. These states are resonant with the PbTe valence band (VB) and extend into the PbTe band gap. Due to these distinct resonant states, Ag-Sb arrangements have a more rapidly increasing density of states near the band gap as opposed to PbTe. Therefore, the electronic structure of $(PbTe)_m$-$AgSbTe_2$ systems have a high sensitivity to micro-structural arrangements of Ag and Sb atoms. Transport calculations show that the enhanced density of states effective mass (m_d^*) near the band gap of LAST-*m* systems relative to that of PbTe gives rise to a slight enhancement in the power factor $S^2\sigma$ [4.3].

Due to a combination of a small enhancement of the power factor and a strong reduction in the thermal conductivity, large *ZT* values of the LAST-12 (~1.2) and LAST-18 (~1.8) systems are observed. The LAST-18 sample reportedly has a power factor of 33.7 μW/

$cm \cdot K^2$ and a thermal conductivity of 2.3 W/m·K at room temperature [4.5]. These n-type bulk nano-composite LAST-*m* samples show an innovative way how to improve the thermoelectric performance of PbTe-based alloys. Nanostructures are introduced into a series of PbTe-based systems using different methods. Properties of some of these materials are discussed in section 4.6.

An efficient thermoelectric module requires both *n*-type and *p*-type materials of high *ZT* (see 1.4). One of the *p*-type counterparts to LAST-*m* is $(Pb_{1-y}Sn_yTe)_m$-$AgSbTe_2$, the so-called LASTT (lead, antimony, silver, tin, tellurium)-*m* system [4.7]. Although the solid solution of PbTe/SnTe is an *n*-type material, $(Pb_{1-y}Sn_yTe)_m$-$AgSbTe_2$ system exhibits consistent *p*-type behavior for the regime $8 \leq m \leq 36$ and $0.1 \leq y \leq 0.6$ studied. Transport studies show that the thermoelectric properties of this system can be fine-tuned by two compositional parameters, which are Pb/Sn ratio and $AgSbTe_2$ content. Substituting Sn for Pb appears to enhance electrical conductivity. For a selection of *y* and *m*, the electrical conductivity is a power function of the temperature T^{-n} ($1.8 \leq n \leq 2.25$) from room temperature to 640 K. The thermopower varies approximately as a linear function of *y*. The LASTT system has very low thermal conductivity. For $Ag_{0.5}Pb_6Sn_2Sb_{0.2}Te_{10}$, the thermal conductivity κ is 1.4 $Wm^{-1}K^{-1}$ at 300 K as opposed to 2.3 $Wm^{-1}K^{-1}$ reported for *p*-type PbTe [4.8]. It decreases rapidly to 0.8 $Wm^{-1}K^{-1}$ at 650 K. The highest *ZT* of this composition is close to 1.45 at 627 K.

An example of excellent *p*-type PbTe-based material is $(PbTe)_m$-$Na_{1-x}Sb_yTe_2$ [4.9]. In this system, Na ion shares the same valence state as Ag ion in $(PbTe)_m$-$AgSbTe_2$. The Coulomb interaction between Na and Sb ions drives the system to form sodium and antimony-rich clusters in the Pb sublattice. TEM images clearly demonstrate dispersed nanoscale features in $(PbTe)_m$-$Na_{1-x}Sb_yTe_2$. Similar to $(PbTe)_m$-$AgSbTe_2$, these nanostructures are favorable to phonon scattering, thus lowering the thermal conductivity. The thermal conductivity drops from 1.8 $Wm^{-1}K^{-1}$ at 300 K to a minimum of 0.85 $Wm^{-1}K^{-1}$ at 675 K, the lattice contribution of which is 0.55 $Wm^{-1}K^{-1}$, comparable to the record low value (0.33 $Wm^{-1}K^{-1}$) of the superlattice thin films of $PbSe_{0.98}Te_{0.02}$/PbTe [4.10]. Due to the low thermal conductivity and high power factor, ZT of $(PbTe)_{20}$-$Na_{0.95}SbTe_2$ exceeds unity at 475 K, and reaches its maximum value of 1.7 at 650 K, higher than ZT = 1.2 at 700 K reported for TAGS system ($AgSbTe_2$-GeTe) [4.11].

4.6 Results and Discussions

Typically, the thermal conductivity of a material can be reduced by large mass mismatch at one atomic position of its lattice such as random-alloy disorder, point defects, and grain boundaries. Incorporating nanometer scale inclusions into bulk semiconductor materials appears to induce stronger phonon scattering than conventional mechanisms [4.5, 4.7, 4.9, 4.12, 4.13]. The lattice thermal conductivity as well as the total thermal conductivity can be significantly reduced. Using this technique, the thermoelectric performance of PbTe-based materials has been greatly improved. Several materials in the lead chalcogenides family have been developed into prospective thermoelectrics recently (in 4.4). Intense efforts have been made to explore prospective candidates in this category.

4.6.1 Sb-doped Lead Telluride/Lead Selenide

Theoretical studies suggest that the inclusions of Sb impurities may enhance the thermopower of lead telluride [4.14]. Since Sb has low solubility in the solid phase of PbTe, part of Sb content is expected to precipitate when the phase segregation between PbTe and Sb occurs upon cooling. In the solid solution of $PbTe_{1-x}Se_x$, Se atom substitutes at the Te sites. Due to the large mass difference between Te and Se, $PbTe_{1-x}Se_x$ exhibits much lower lattice thermal conductivity than PbTe. Embedding Sb precipitates in $PbTe_{1-x}Se_x$ should further reduce its lattice thermal conductivity. The enhanced thermopower and reduced thermal conductivity lead to higher figure of merit ZT ($= S^2\sigma T/\kappa$).

Polycrystalline ingots of composition $Pb_{9.6}Sb_{0.2}Te_{10-x}Se_x$ (x = 0 to 10) were prepared by Dr. Pierre F. P. Poudeu using high temperature solid-state reaction. Thermoelectric properties were measured from 300 K to 700 K. Fig. 4.2 shows that the lattice thermal conductivity κ_L of $Pb_{9.6}Sb_{0.2}Te_{10-x}Se_x$ is lower than those of $PbTe_{1-x}Se_x$ solid solutions with the same Se concentration x at 300 K [4.15-4.16]. The lattice thermal conductivity of $Pb_{9.6}Sb_{0.2}Te_{10-x}Se_x$ decreases with x to a minimum value at x = 7 and then starts increasing with x. Clearly, in addition to the mass difference between Se and Te, Sb doping has induced stronger phonon scattering in the $PbTe_{1-x}Se_x$ alloy.

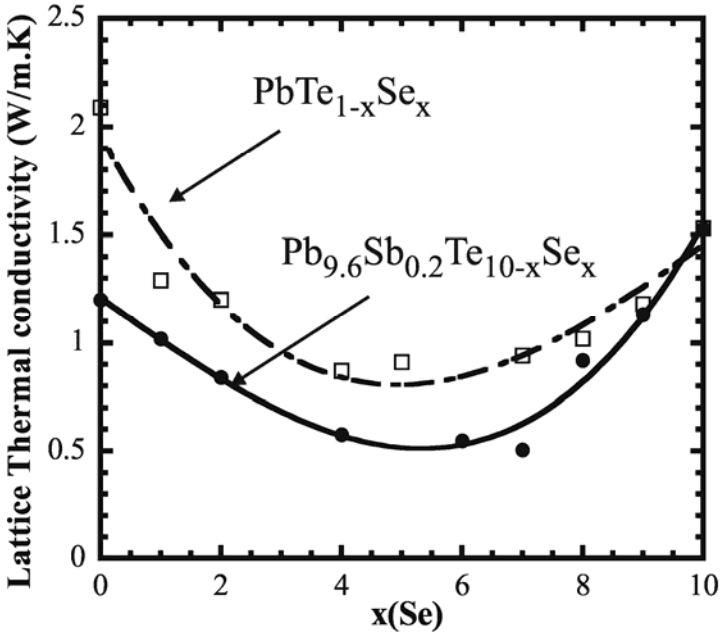

Fig. 4.2. Comparison of the lattice thermal conductivity of $Pb_{9.6}Sb_{0.2}Te_{10-x}Se_x$ with those of the $PbTe_{1-x}Se_x$ solid solutions at 300 K.

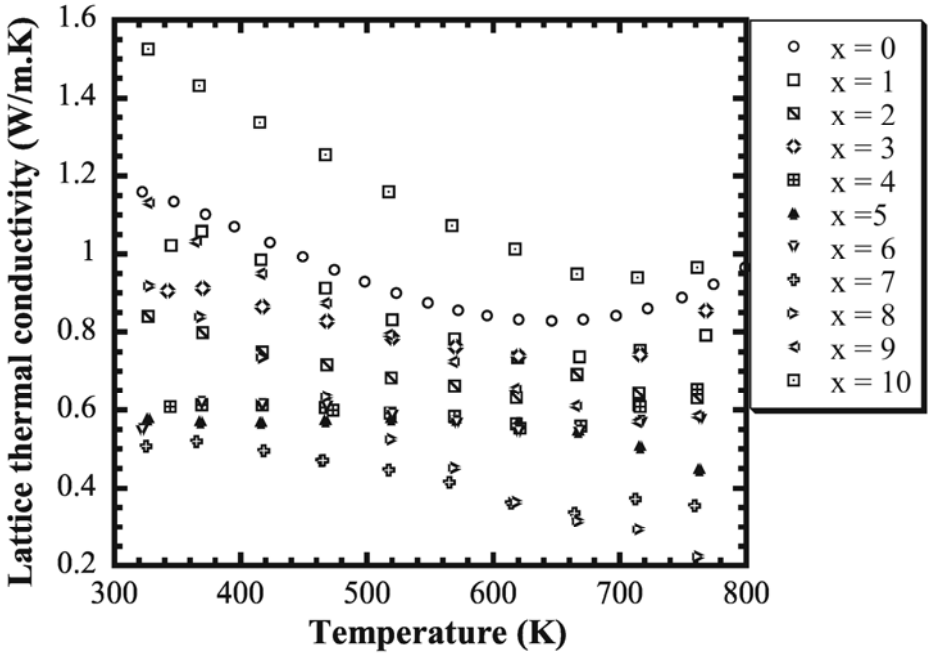

Fig. 4.3. Temperature dependence of the lattice thermal conductivity of $Pb_{9.6}Sb_{0.2}Te_{10-x}Se_x$ (x = 0 to 10) samples from 300 K to 800 K.

The lattice thermal conductivity is plotted over a temperature range of 300 K to 800 K in Fig. 4.3. Among various compositions of $Pb_{9.6}Sb_{0.2}Te_{10-x}Se_x$, x = 4, 6, 7 show the lowest lattice thermal conductivity over the entire range. For $Pb_{9.6}Sb_{0.2}Te_{10-x}Se_x$ (x = 4 and 6), κ_L is approximately 0.6 W/m·K at 300 K and remains flat with increasing temperature. This value is ~ 33% lower than that of $PbTe_{1-x}Se_x$ with the same x [4.16]. The composition with x = 7 shows the lowest κ_L ~ 0.5 W/m·K at 300 K and reduces to 0.4 W/m·K at 750 K. The strong reduction of the lattice thermal conductivity is attributed to the widely distributed Sb-rich nanoparticles in the lattice, which were observed by the high resolution TEM images of these samples [4.15]. Short wavelength phonons are scattered by atomic disorder, while the long wavelength phonons are effectively scattered at the grain boundaries. These Sb-rich nanocrystals scatter mid-to-long wavelength phonons.

The strong reduction of lattice thermal conductivity κ_L leads to a significant enhancement of the dimensionless figure of merit ZT. Fig. 4.4 plots ZT of $Pb_{9.6}Sb_{0.2}Te_{10-x}Se_x$ against PbTe from 300 K to 700 K. Among all the compositions, $Pb_{9.6}Sb_{0.2}Te_3Se_7$ (x = 7) has the highest ZT ~ 1.2 at 650 K. This value is 50% higher than the figure of merit of PbTe at 650 K. For samples with x = 0, 2, 4, 5, 6, 8, the maximum ZT is 1.1, 0.82, 0.93, 1.17, 0.96, and 1.18 at 700 K, respectively. Most compositions in the $Pb_{9.6}Sb_{0.2}Te_{10-x}Se_x$ system have good thermoelectric performance as expected.

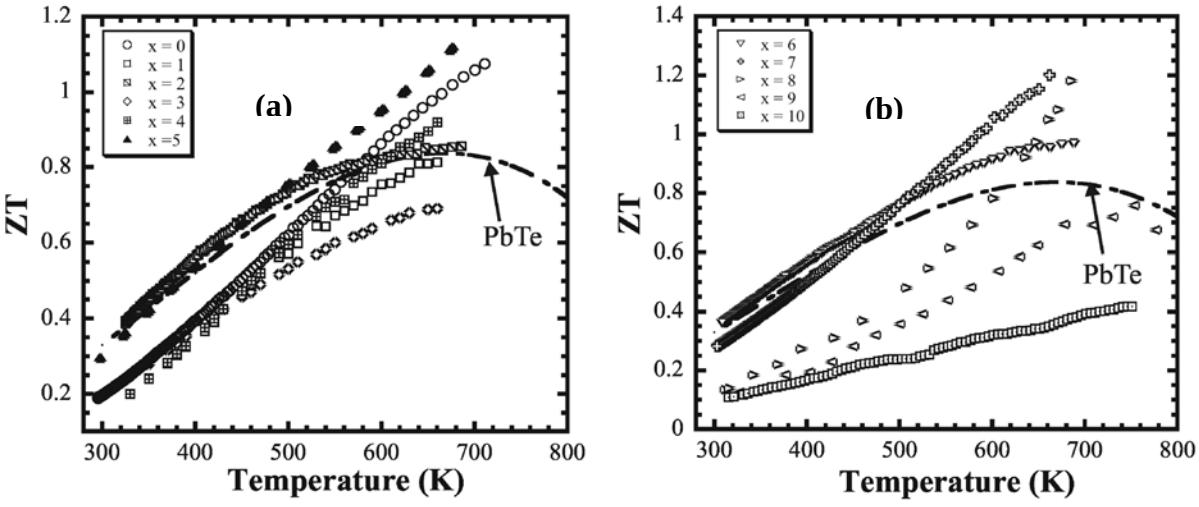

Fig. 4.4. Temperature dependence of the dimensionless figure-of-merit ZT of $Pb_{9.6}Sb_{0.2}Te_{10-x}Se_x$ for (a) x = 0 to 5; (b) x = 6 to 10, compared to PbTe.

4.6.2 Bi/Sb/InSb-doped Lead Telluride

Several PbTe samples embedded with nanoparticles of Sb, Bi and InSb were prepared by Joseph R. Sootsman, using a liquid matrix encapsulation technique [4.17-4.18]. Just like Sb, Bi and InSb have low solubility in PbTe [4.19]. Samples with fairly low concentration of dopants are more likely to form smaller sized precipitates, which promote phonon scattering. Sb nanoparticles were revealed in TEM images of Sb-doped PbTe (see Fig. 4.5). The quantity and size of the nanoparticles increased with concentration of Sb. Fig. 4.5 (C) and (D) are from the PbTe-rich region. Microscale studies showed that μm-sized Sb regions appear in the PbTe matrix at Sb fractions higher than 4% [4.18].

The thermal conductivity was determined by measuring thermal diffusivity and specific heat capacity seperately. The lattice thermal conductivity was obtained by subtracting the electronic component from the total thermal conductivity using the Wiedemann-Franz law. Nanoparticles (e.g. Sb, InSb) which have larger mass contrast with PbTe achieve stronger scattering of acoustic phonons. The inset of Fig. 4.6 shows the lattice thermal conductvity κ_{lat} of PbTe with 4% Bi, Sb, and InSb from 300 K to 700 K. InSb has the largest mass contrast with Pb and exhibits the lowest lattice thermal conductivity (~ 45% lower than PbTe at 300 K [4.20]). Similarly, Sb nanoparticles also cause considerable reduction (~27%) of κ_{lat} relative to PbTe. Since Bi has nearly the same atomic mass as Pb, the sample with 4% Bi showed no reduction compared to PbTe.

The concentration of dopants influences the size and quantity of nanoparticles formed from precipitation on cooling, thereby affecting the lattice thermal conductivity. The relation between the two was studied for the PbTe-Sb system. Fig. 4.6 shows that, among three samples with 2%, 4% and 16% Sb concentration respectively, the 2% sample exhibits the lowest thermal conductivity of 0.8 $Wm^{-1}K^{-1}$ and the 16% sample exhibits the highest lattice thermal conductivity closer to that of pure PbTe. These results indicate that a significant reduction of the thermal conductivity can be achieved provided the nanosized phase (e.g. Sb, InSb) is properly chosen to enhance phonon scattering in PbTe lattice. There exists an optimum concentration beyond which the lattice thermal

conductivity starts to increase with concentration of nanoparticles. Experimental results suggest that the optimum concentration of Sb in PbTe is below 2%.

Theoretical studies suggest that nanoparticles effectively scatter mid- and long-wavelength phonons, while atomic scale defects effectively scatter short-wavelength phonons. Sb and InSb nanoparticles act as effective scattering centers for mid-to-long wavelength phonons in the PbTe lattice.

As a followup to this study, nanostructured composite PbTe with excess of both Pb and Sb metal inclusions has been studied. The original paper is listed in Appendix.

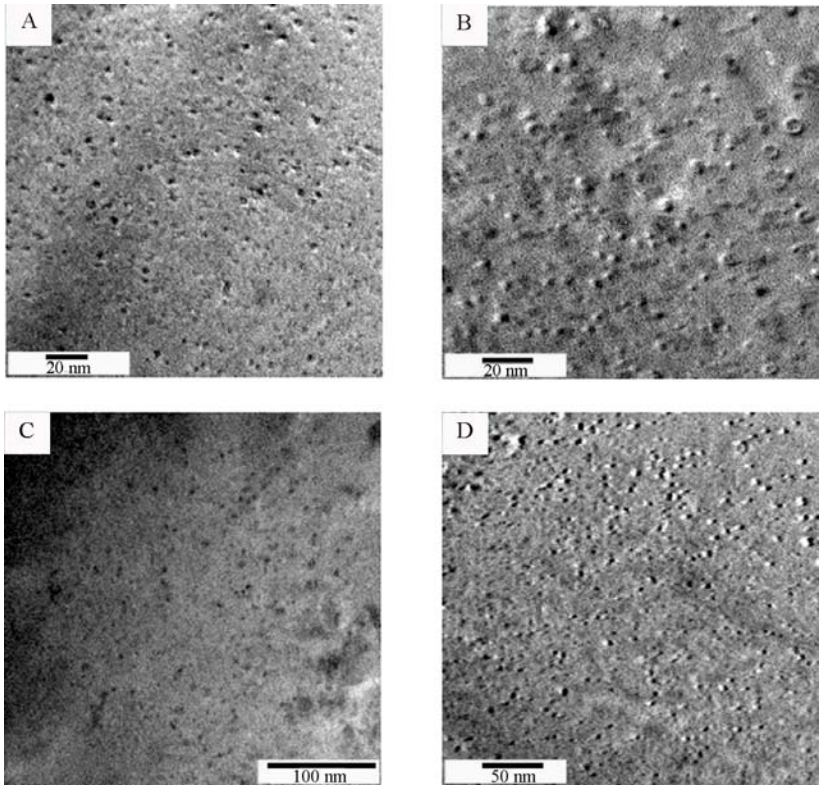

Fig. 4.5. TEM images of (A) PbTe-Sb(2%) (B) PbTe-Sb(4%) (C) PbTe-Sb(8%) (D) PbTe-Sb(16%) showing nanocrystals of Sb.

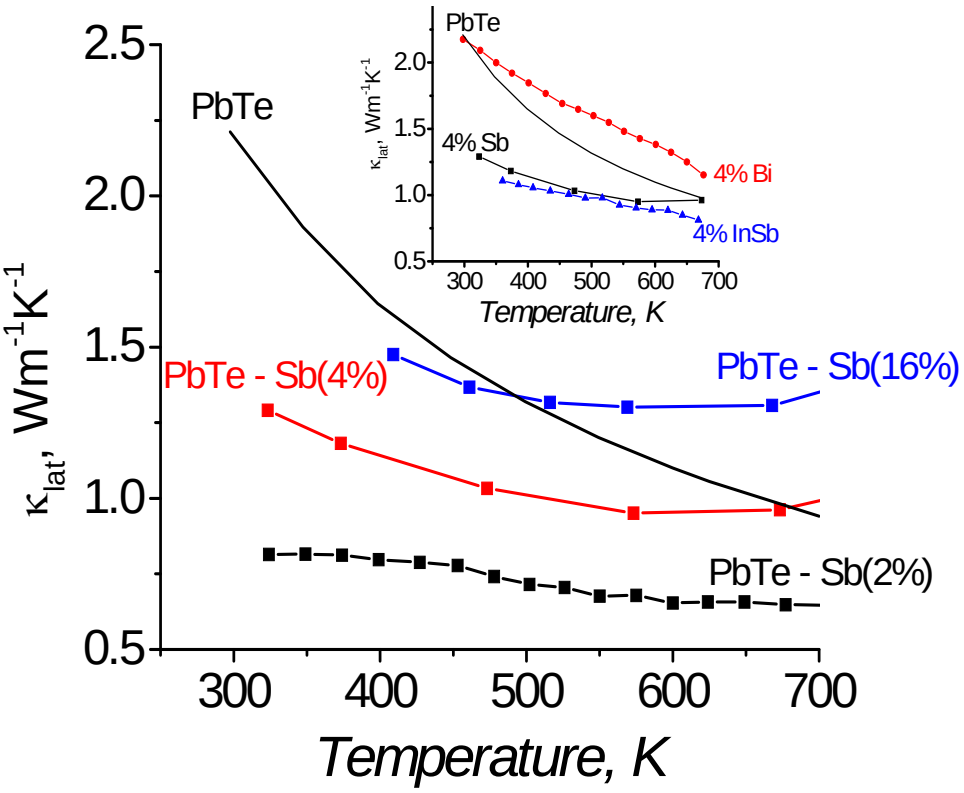

Fig. 4.6. Lattice thermal conductivity for PbTe with 2%, 4%, and 16% Sb concentration. The inset plots lattice thermal conductivity for 4% inclusion phase Sb, Bi, and InSb compared to pure PbTe (black solid line).

4.6.3 Nanostructured Lead Tin Telluride – Lead Sulfide

$(Pb_{0.95}Sn_{0.05}Te)_{1-x}(PbS)_x$ were prepared by Dr. John Androulakis and Dr. Chia-Her Lin using the technique of spinodal decomposition and nucleation-growth [4.21-4.22]. Adding small amount of Sn removes gas pockets without changing transport properties. The system is not a normal solid solution and has two phases segregated partially by spinodal decomposition: PbTe-rich and PbS-rich region, creating periodical compositional fluctuation on a global scale [4.23]. Phase segregation by nucleation-growth leads to local compositional fluctuation [4.24]. Both mechanisms produce coherent nanoscale heterogeneities. The lattice thermal conductivity is reduced significantly due to the acoustic impedance (mass) mismatch between the PbTe-rich and PbS-rich regions. The degree of spinodal decomposition increases with the fraction of PbS in PbTe (x).

$(Pb_{0.95}Sn_{0.05}Te)_{1-x}(PbS)_x$ system exhibits very low lattice thermal conductivity. Fig. 4.6 displays the total, electronic and lattice thermal conductivity of $(Pb_{0.95}Sn_{0.05}Te)_{1-x}(PbS)_x$ for x = 0.04, 0.08, 0.16. The total thermal conductivity κ_{tot} is measured by the laser flash diffusivity – heat capacity method. The electronic component κ_{el} is calculated using the Wiedemann-Franz law with the Lorenz number equal to 2.44×10^{-8} V^2/K^2 for degenerate semiconductors. The lattice thermal conductivity κ_{lat} is determined by subtracting κ_{el} from κ_{tot}.

As shown in Fig. 4.7, the lattice thermal conductivities κ_{lat} at room temperature are 0.84, 0.38, 0.40 $Wm^{-1}K^{-1}$ for PbTe with 4%, 8%, 16% PbS, respectively. All three values are much lower than κ_{lat} of bulk PbTe (2.10 $Wm^{-1}K^{-1}$). The lattice thermal conductivity κ_{lat} of the 8% and 16% samples are remarkably low, comparable to that of PbTe/PbSe thin-film superlattice (0.33 $Wm^{-1}K^{-1}$). TEM images indicate that nanostructures formed by nucleation/growth are more prominent in the 8% and 16% sample than the 4% sample [4.22]. Compared to spinodal decomposition, nucleation/growth mechanism creates larger compositional fluctuation of smaller size, giving rise to larger mass mismatch between the PbTe-rich and PbS-rich regions. This may explain more significant reduction of κ_{lat} in the 8% and 16% sample than in the 4% sample.

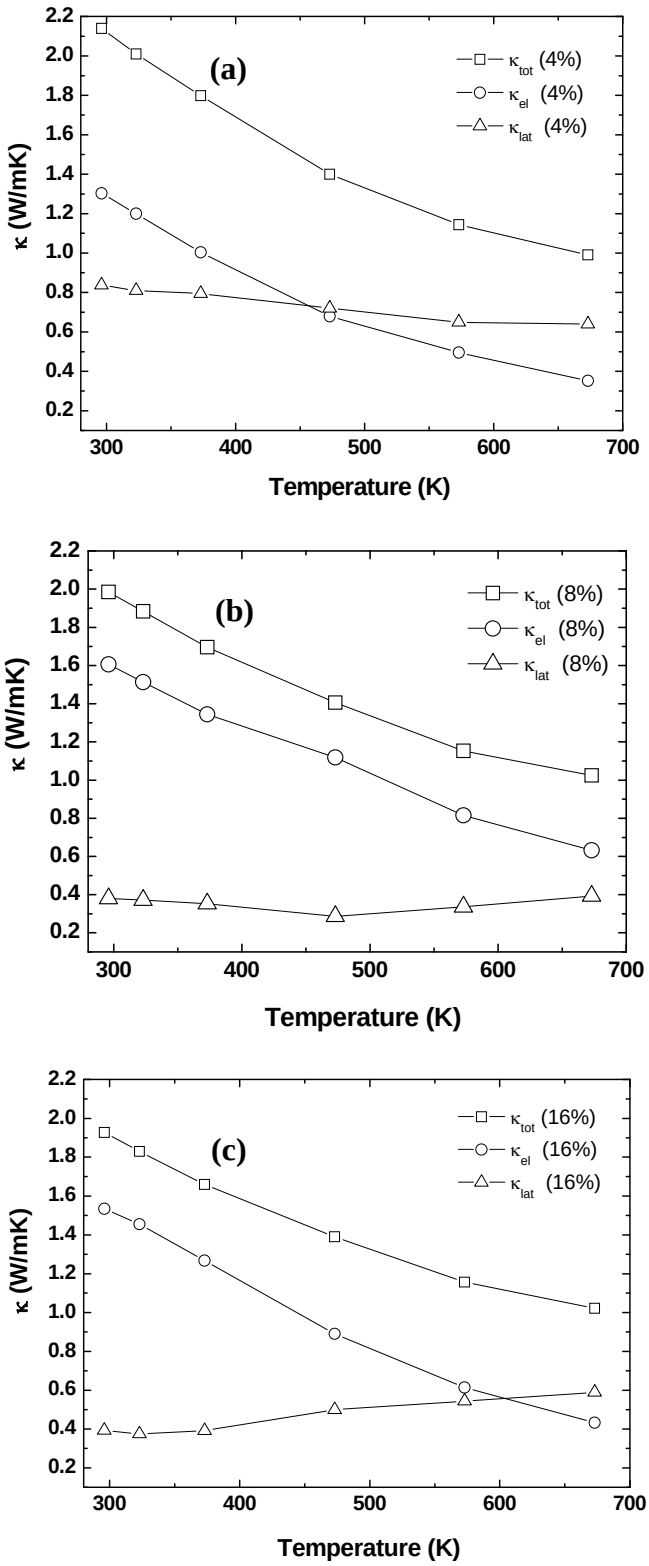

Fig. 4.7. Total (squares), electronic (circles), and lattice (triangles) thermal conductivity of PbTe with (a) 4%; (b) 8%; (c) 16% PbS.

Fig. 4.8 and 4.9 show electrical conductivity and Seebeck coefficient of PbTe with 4%, 8%, and 16% PbS. All three samples are doped with 0.055mol% PbI_2 to make them *n*-type. They show very high electrical conductivity at room temperature and retain decent values close to 700 K. In Fig. 4.9, the negative sign of Seebeck coefficient indicates *n*-type semiconductor conduction. Fig. 4.8 also shows the onset of intrinsic conduction occurs beyond 700 K, where Seebeck coefficient reaches a maximum and then decreases. As a result, this system provides a broad operational range. The highest power factor ($S^2\sigma$) achieved is 22 $\mu Wcm^{-1}K^{-2}$ at 642 K for the 8% sample.

The dimensionless figure of merit ZT is calculated from 300 K to 800 K for x = 4%, 8%, and 16%, Fig. 4.10. The highest ZT are approximately 1.10 at 642 K for 4%, 1.50 at 642 K for x = 0.08, and 1.28 at 660 K for x = 0.16.

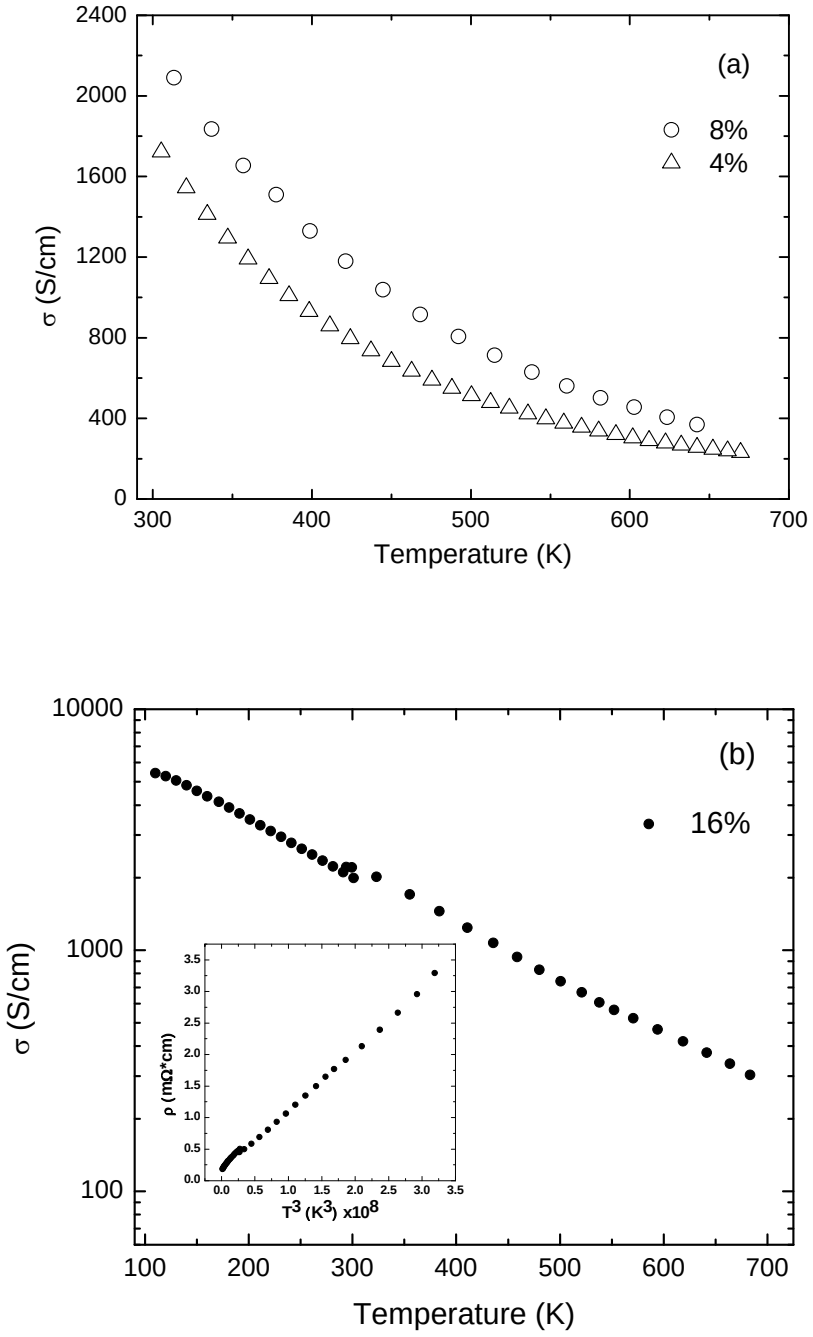

Fig. 4.8. Electrical conductivity of PbTe with (a) 4 and 8%, (b) 16% PbS as a function of temperature. The discontinuity around 300 K is due to the change of measurement apparatuses from low to high temperatures. The inset plots resistivity as a function of T^3.

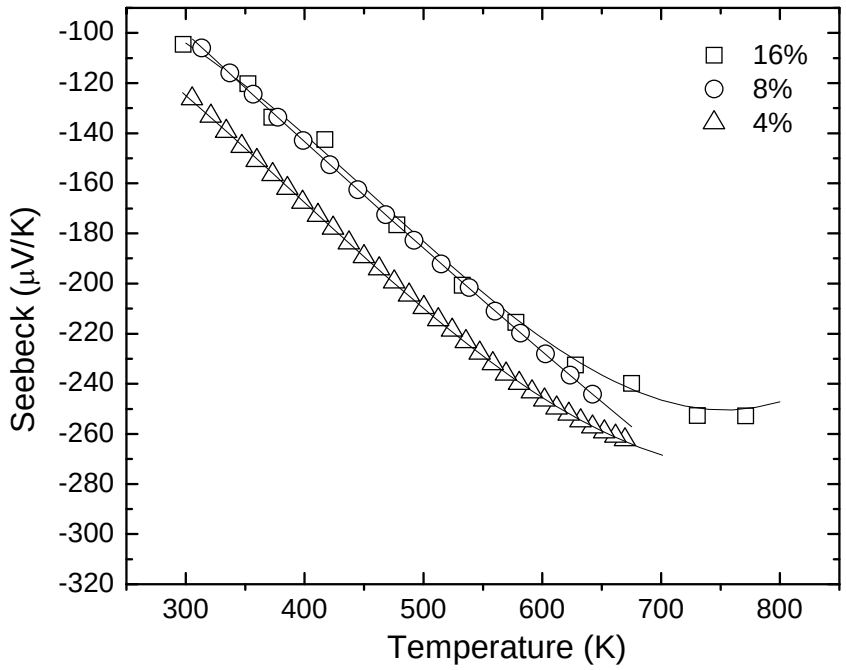

Fig. 4.9. Seebeck coefficient of PbTe with 4%, 8%, 16% PbS as a function of temperature from 300 K to 800 K.

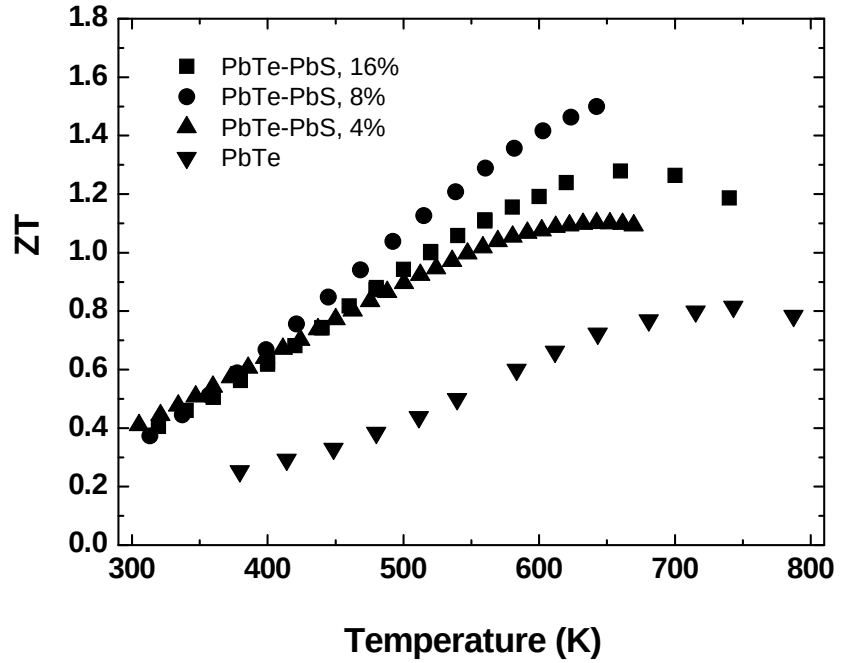

Fig. 4.10. The dimensionless figure of merit ZT of PbTe with 4%, 8%, 16% PbS as a function of temperature from 300 K to 800 K.

4.6.4 Europium-doped Lead Telluride

Eu-doped PbTe system is another attempt to chemically insert nanoparticles into bulk PbTe. Ingots with nominal composition PbTe + x% Eu (x = 0.5, 1, 2 and 3) were synthesized by Dr. Pierre F. P. Poudeu. The intention of adding Eu is to form nanoparticles to reduce lattice thermal conductivity. However, instead of Eu nanoparticles, traces of Pb particles are observed in the $Pb_{1-x}Eu_xTe$ alloys using several different experimental methods such as X-ray powder diffraction, differential thermal analysis and SEM images (Fig. 4.13). Results also indicate that the density of Pb particles increases with Eu concentration. One explanation is that Eu^{2+} replaces Pb^{2+} upon cooling. This notion is supported by the facts that Eu can easily form solid solution with PbTe and EuTe has much higher melting point (1526^{o}C) than that of PbTe (924^{o}C). The effect of Eu concentration and segregated Pb particles on thermoelectric properties is discussed.

The melting behavior of Pb secondary phase in the PbTe-rich alloy was studied using differential scanning calorimetry (DSC). Specific heat capacity is plotted as a fuction of temperatuare for PbTe with 0.5, 1, 2, 3% Eu in Fig. 4.11. A peak around 600 K is observed for all four samples. This temperature coincides with the melting point of Pb metal. This observation is a direct evidence of the presence of metallic Pb particles. The intensity of the peak is an indication of the concentration of Pb particles. Presumably, higher concentration of Eu results in more Pb precipitates. But the relationship is not exactly linear. Since Pb particles precipitate upon cooling, it is quite possible that the formation of Pb particles depends on the cooling rate. For slowly cooled samples, the intensity of the C_p peak follows the same order as the concentration of Eu except for x = 0.5%. No significant shift of the melting temperature of the Pb secondary phase is observed for different concentration of Eu, suggesting uniform size of Pb particles in all samples.

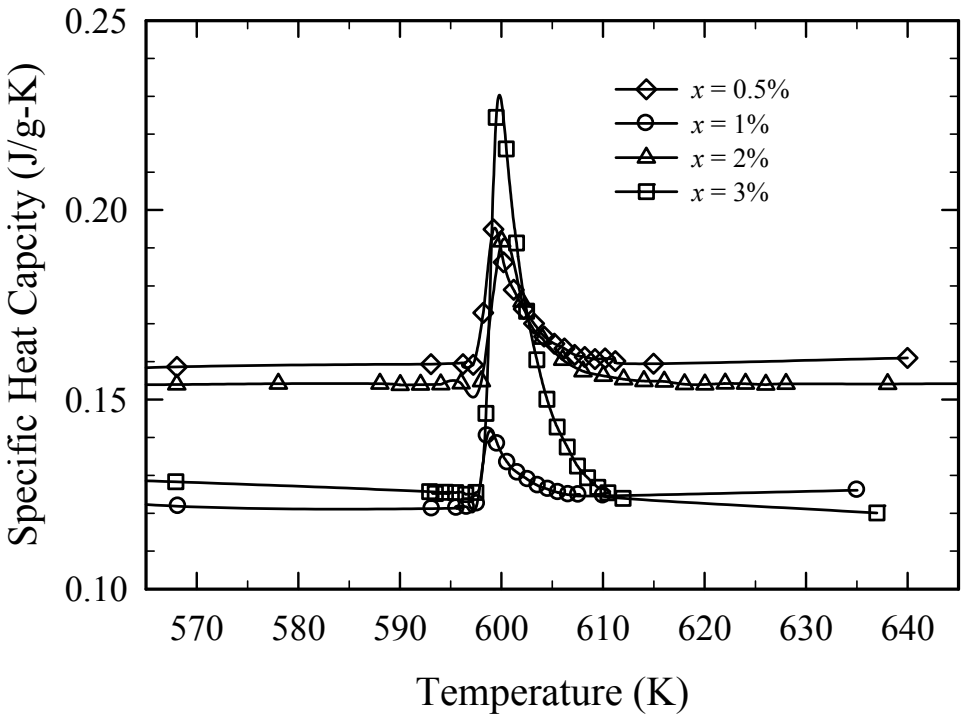

Fig. 4.11. Specific heat capacity of PbTe + *x*% Eu (*x* = 0.5, 1, 2, 3) prepared by slow cooling as a function of temperature.

Because Eu^{2+} ($4f^7$) has half filled *f* shell electrons, the PbTe + *x*% Eu alloy is expected to be magnetic. Fig. 4.12 plots the temperature dependence of magnetic susceptibility and its inverse for PbTe + *x*% Eu per mole of composition $PbTeEu_{0.02x}$. The magnetic susceptibility increases with concentration of Eu. The Curie-Weiss law yields moments of 7.94 and 7.91 Bohr magnetons for the 1% and 3% samples, respectively, close to the spin-only effective magnetic moment for Eu^{2+} of 7.94 Bohr magnetons. These results evidence that Eu^{2+} substitutes for Pb^{2+}.

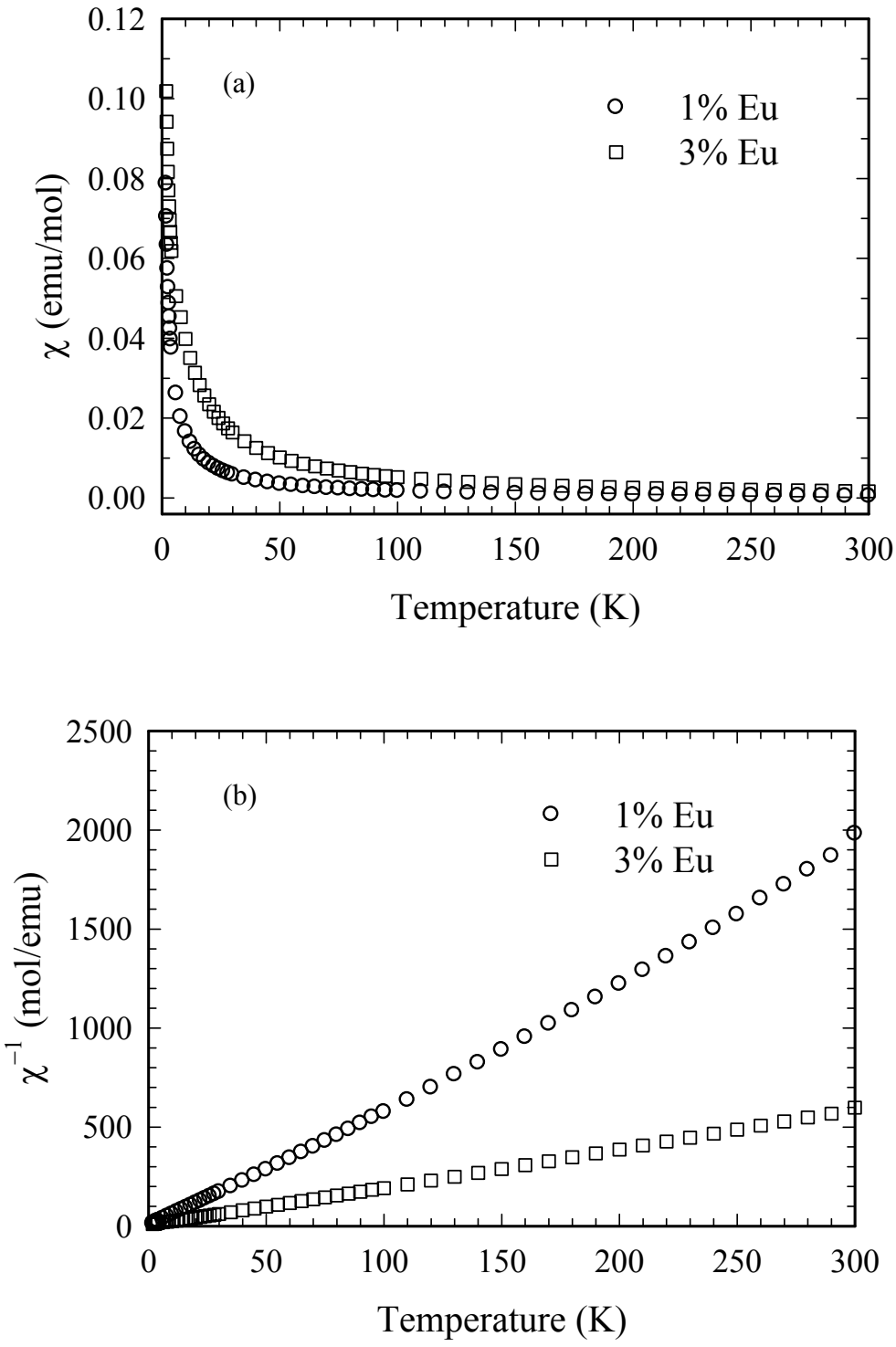

Fig. 4.12. Magnetic susceptibility and its inverse as a function of temperature for PbTe + *x*% Eu (a) *x* = 1; (b) *x* = 3.

Fig. 4.14 plots the thermoelectric properties for slowly-cooled PbTe with 0.5, 1, 2, 3% Eu as a function of temperature. In Fig. 4.14 (b), thermopower decreases with concentration of Eu. Like specific heat capacity, thermopower is also sensitive to the phase transition such as the melting of Pb particles. The plot (b) shows a noticeable discontinuity around 600K for all four samples, which corresponds to the melting temperature of Pb. This observation is consistent with DSC results, providing further evidence of the melting of metallic Pb particles. In Fig. 4.14 (c), at 300 K, the lattice thermal conductivity κ_{latt} ranges from 1.4 W/m-K to 2.4 W/m-K. κ_{latt} drops rapidly with increasing temperature and reaches a minimum value of 0.8 W/mK around 650 K. This is a significant reduction as compared to the value of 2.1 W/mK observed for pure PbTe [4.23]. Since the alloy is PbTe rich, the precipitated Pb particles have almost no mass contrast with the medium. In other words, Pb particles have very little contribution to the scattering of short-wavelength phonons due to the atomic disorder. SEM images reveal rod–shaped Pb particles in all samples, which are 1 – 3 μm thick and up to 50μm in length (Fig. 4.13). They are randomly oriented in the crystalline $Pb_{1-x}Eu_xTe$ lattice. The larger size of Pb particles inhibits them from scattering mid-to-long wavelength phonons effectively. Therefore, the atomic mass difference between Pb^{2+} and Eu^{2+} in the $Pb_{1-x}Eu_xTe$ alloy may account mostly for the reduction in the lattice thermal conductivity. The electrical conductivity is moderate. Overall, ZT is not as good as we might have hoped it would be (Fig. 4.14).

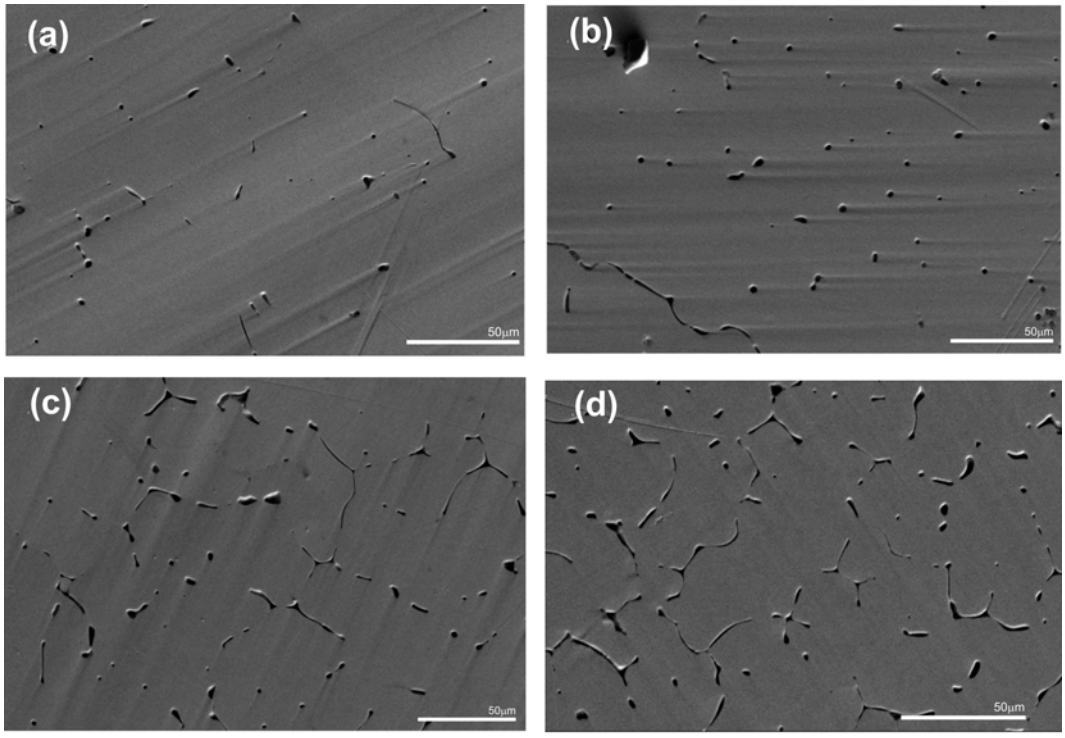

Fig. 4.13. Back scattering SEM images of PbTe + *x*%Eu samples. (a) $x = 0.5$; (b) $x = 1$; (c) $x = 2$; (d) $x = 3$.

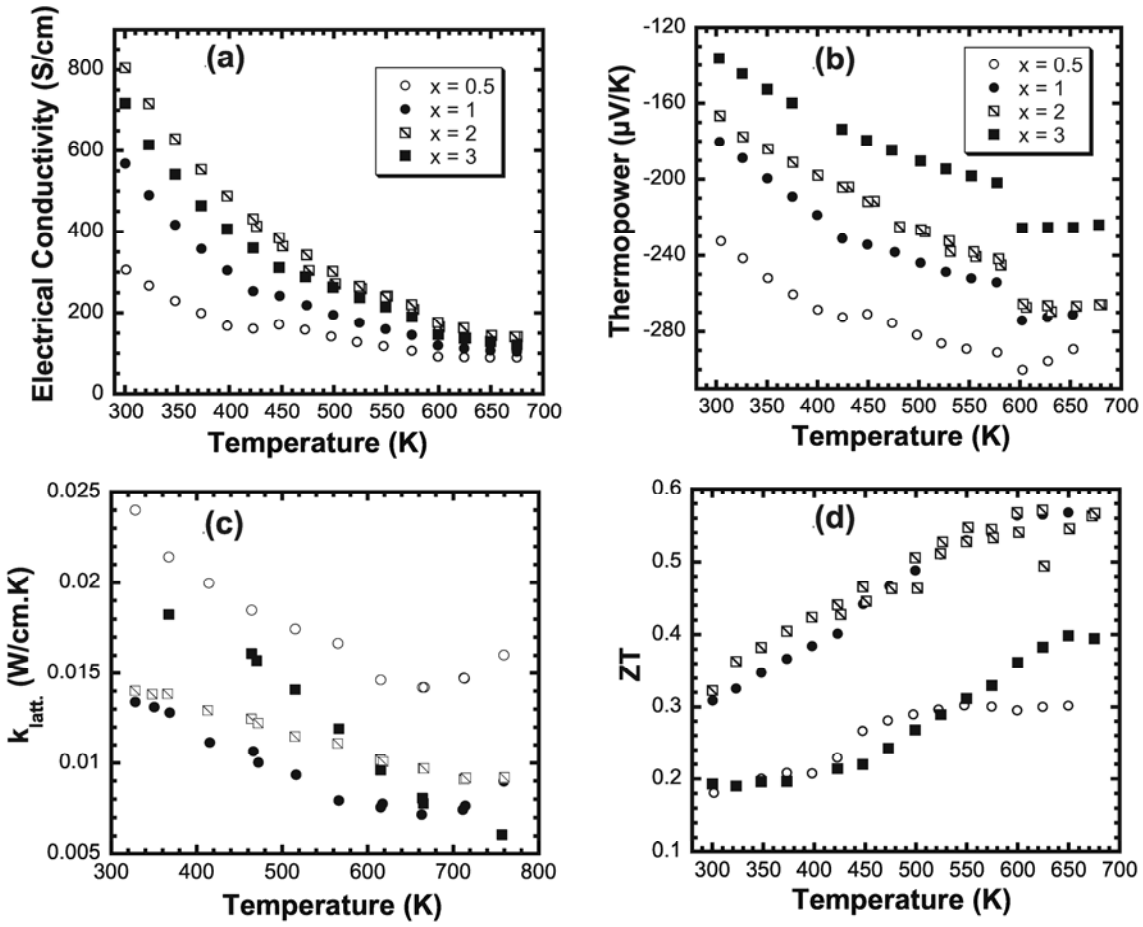

Fig. 4.14. Temperature dependence of the thermoelectric properties of PbTe + *x*%Eu (*x* = 0.5, 1, 2, 3) samples. (a) electrical conductivity; (b) thermopower; (c) lattice thermal conductivity (κ_{latt}); (d) dimensionless figure of merit (ZT).

4.7 Conclusions

By incorporating a small percentage of impurities into the matrix in the form of nanostructures, dimensionless figure-of-merit (ZT) of lead chalcogenide-based compounds is greatly enhanced compared to PbTe. The compounds are macroscopically homogeneous but phases segregate on a nanometer scale. The electronic properties are nearly intact. Nanoparticles scatter phonons of wavelength comparable to nanosize, which is longer than atomic size. Due to the extended phonon scattering spectrum, the compounds have very low lattice thermal conductivity, which is the main reason for the improved ZT. For example, ZT values of 1.50 and 1.2 are achieved for $(Pb_{0.95}Sn_{0.05}Te)_{0.92}(PbS)_{0.08}$ and $Pb_{9.6}Sb_{0.2}Te_3Se_7$, respectively. As a follow up to this study, analogs to the lead telluride-based compounds such as tin telluride and cadmium telluride have also been explored.

Reference to Chapter IV

4.1 Yu.I. Ravich, B. A. Efimova, I. A. Smirnov: Semiconducting lead chalcogenides, edited by L. S. Stil'bans (Plenum Press, New York, 1970)

4.2 W. Kim, A. Majumdar, J. App. Phys. **99**, 084306 (2006)

4.3 D. Bilc, S. D. Mahanti, M.G. Kanatzidis, Phys. Rev. B **74**, 125202 (2006)

4.4 J. P. Heremans, C. M. Thrush, D. T. Morelli, Phys. Rev. B **70**, 115334 (2004)

4.5 K. F. Hsu, S. Loo, F. Guo, W. Chen, J. S. Dyck, C. Uher, T. Hogan, E. K. Polychroniadis, M. G.. Kanatzidis, Science **303**, 818 (2004)

4.6 D. Bilc, S. D. Mahanti, E. Quarez, K. F. Hsu, R. Pcionek, M.G. Kanatzidis, Phys. Rev. Lett. **93**(14), 146403 (2004)

4.7 J. Androulakis, K. F. Hsu, R. Pcionek, H. Kong, C. Uher, J. J. D'Angelo, A. Downey, T. Hogan, M. G. Kanatzidis, Adv. Mater. **18**, 1170 (2006).

4.8 A. F. Ioffe: Semiconductor Thermoelements and Thermoelectric Cooling (Infosearch, London, 1957)

4.9 P. F. P. Poudeu, J. D'Angelo, A. D. Downey, J. L. Short, T. P. Hogan, M. G. Kanatzidis, Angew. Chem. **118**, 3919 (2006)

4.10 T. C. Harman, P. J. Taylor, M. P. Walsh, B. E. LaForge, Science **297**, 2229 (2002)

4.11 E. A. Skrabek, D. S. Trimmer, in CRC Handbook of Thermoelectrics, edited by D. M. Rowe (CRC Press, Boca Raton, 1995), p. 267

4.12 W. Kim, J. Zide, A. Gossard, D. Klenov, S. Stemmer, A. Shakouri, A. Majumdar, Phys. Rev. Lett. **96**, 045901 (2006)

4.13 X. Y. Zhao, X. Shi, L. D. Chen, W. Q. Zhang, S. Q. Bai, Y. Z. Pei, X. Y. Li, T. Goto, Appl. Phys. Lett. **89**, 092121 (2006)

4.14 S. D. Mahanti, D. Bilc, J. Phys.: Condens. Matter, **16**, S5277 (2004)

4.15 P. F. P. Poudeu, J. D'Angelo, H. Kong, A. Downey, J. L. Short, R. Pcionek, T. P. Hogan, C. Uher, M. G. Kanatzidis**,** J. Amer. Chem. Soc. **128**, 14347 (2006)

4.16 E. D. Devyatkova, V. V. Tikhonov, Sov. Phys. Solid State, **7**, 1427 (1965)

4.17 L. E. Brus, J. Phys. Chem. **90**, 2555 (1986)

4.18 J. Sootsman, R. J. Pcionek, H. Kong, C. Uher, M. G. Kanatzidis, Chem. Mater. **18**, 4993 (2006**)**

4.19 G. W. Henger, E. A. Peretti, J. Less-Common Met. **8**, 124 (1965)

4.20 V. I. Fedorov, V. I. Machuev, Sov. Phys. Solid State, USSR **11**, 1116-1120 (1969)

4.21 J. W. Cahn, J. Chem. Phys. **42** (1), 93 (1965),

4.22 J. Androulakis, C. H. Lin, H. Kong, C. Uher, C. I. Wu, T. Hogan, B. A. Cook, T. Caillat, K. M. Paraskevopoulos, M. G.. Kanatzidis, J. Amer. Chem. Soc. **129**, 9780 (2007)

4.23 V. Leute, N. Z. Volkmer, Phys. Chem. Neue Folge **144**, 145-155 (1985)

4.24 C. R. M. Grovenor, H. T. G. Hentzell, D. A. Smith, Acta Metall. **32** (5), 773-781(1984)

Chapter V
Double-filled Cobalt Tri-Antimonide

Skutterudites have been widely studied for their potential applications in thermoelectric power generation at intermediate temperatures from 600 K to 900 K. Since 1977, filling of skutterudites has been proposed as an effective method of reducing the lattice thermal conductivity κ_L of binary skutterudites [5.1-5.2]. Various metal atoms such as rare earths, alkaline earths, and alkalis are introduced into the large interstitial voids of the skuterudite structure [5.3-5.15]. These weakly bound filler ions behave as independent oscillators, often referred as "rattlers". The phonon modes of the "rattlers" interfere with normal phonon modes of the lattice. As a result, the "rattlers" strongly scatter the low frequency (acoustic) phonons that are responsible for most of the heat conduction in solids, thus reducing κ_L [5.1].

We selected filled cobalt triantimonide ($CoSb_3$) as the candidate for skutterudite host because it has the lowest thermal conductivity of binary skutterudites and because it is relatively inexpensive [5.16]. Much study has been done on the filling fraction limit and resonant frequency of different fillers for $CoSb_3$ [5.17-5.18]. Double-filled skutterudites scatter broader spectra of acoustic phonons than single-filled ones do, and therefore have lower lattice thermal conductivity. Based on theoretical studies of the potential fillers for $CoSb_3$, Ba and Yb differ most in the resonant frequency among them [5.17]. Filling the large interstitial voids of $CoSb_3$ structure with both Ba and Yb could enhance phonon scattering more than the other combinations of two fillers. As demonstrated in this chapter, excellent thermoelectric performance is achieved in a series of *n*-type $Ba_xYb_yCo_4Sb_{12}$ compounds (where $0.03 \le x \le 0.15$ and $0 \le y \le 0.12$). Highest ZT obtained in this system is 1.36 at around 800 K for $x = 0.08$ and $y = 0.09$.

5.1 Skutterudite Structure

In addition to lead telluride-based alloys, another class of efficient thermoelectric materials called skutterudites is studied as part of the thesis work. Skutterudites are binary compounds with a general composition of MX_3, where M is one of the group 9 transition metals Co, Rh, or Ir, and X is one of the pnicogens P, As, or Sb. This series of compounds has the same body-centered-cubic crystal structure in the space group *Im3*.

Fig. 5.1 displays a crystallographic unit cell of binary skutterudite MX_3, which consists of eight units of MX_3. Eight metal atoms (M) occupy the *c*-sites, forming a simple cubic sublattice. 24 pnicogen atoms (X) are situated at the *g*-sites of the structure. Four X atoms are located at the corners of a square ring (X_4). Six planar X_4 rings are arranged with two each oriented in the xy-plane, the yz-plane, and the zx-plane, where x, y, and z are the cubic crystallographic axes. The structure can be uniquely specified by the lattice constant and two positional parameters *y* and *z* that denote the *g* sites.

Both M-X and X-X distances are close to the sum of the covalent radii, indicating strong covalent bonding among them. M-M distance is much larger, and M has no nearest neighbor metal atoms, implying weak bonding between M atoms [5.1]. The interstitial voids are located at the 2*a* positions (12-coordinated) in the crystal lattice. The crystallographic unit cell can be represented by $\square_2M_8X_{24}$, where $\square$ stands for a void in the structure. Filled skutterudites are formed by inserting guest atoms such as rare-earth, alkali or alkaline-earth into these voids. As shown in Fig. 5.2, corner-sharing MX_6 octahedrals form an irregular dodecahedral (12-fold) cage. The filler atom is enclosed in this cage. Slack predicted that these guest atoms rattle inside the lattice, scatter low frequency acoustic phonons, and therefore can effectively reduce the lattice thermal conductivity [5.2]. The concept was subsequently demonstrated experimentally [5.3-5.4]. This mechanism is explained in section 5.2.

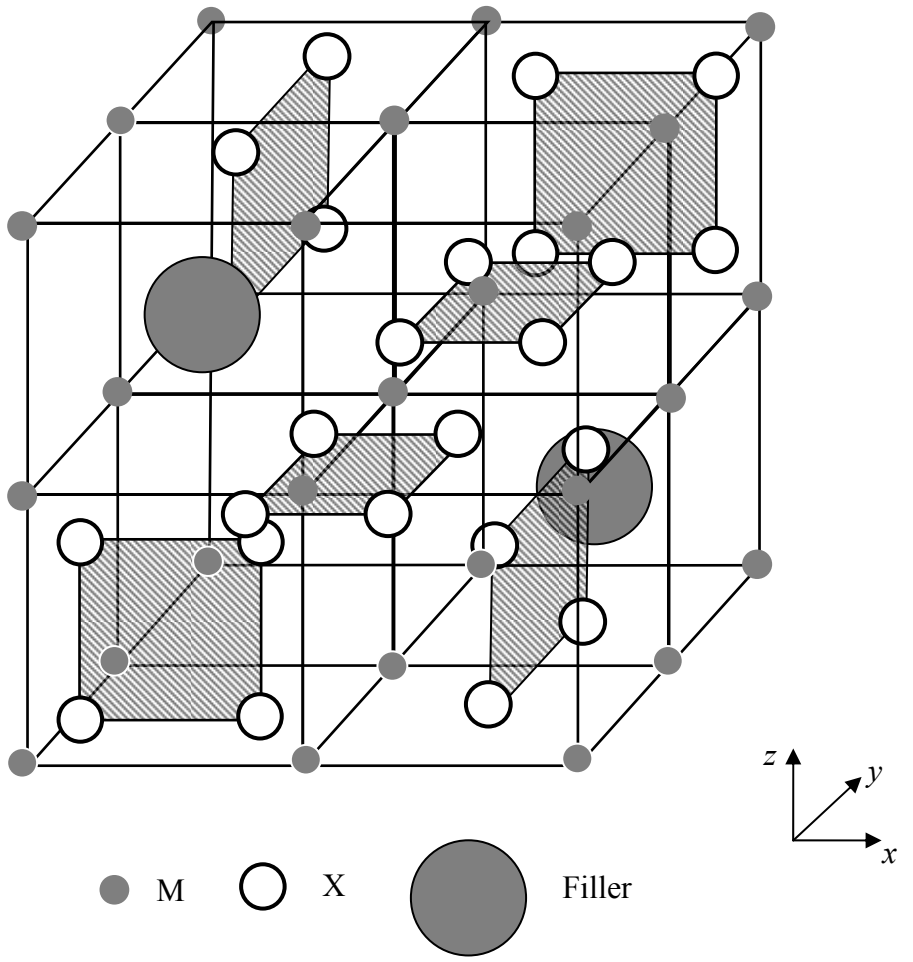

Fig. 5.1. The crystal structure of binary skutterudite MX_3 depicting two filler ions at the 2*a* positions.

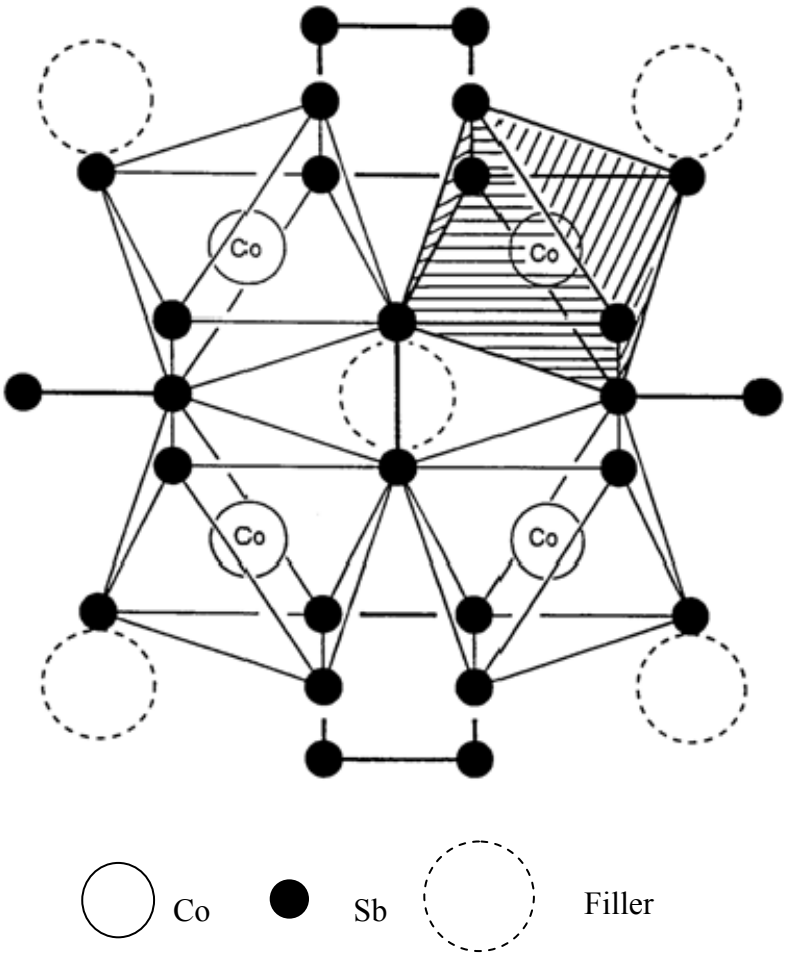

Fig. 5.2. A unit cell of $CoSb_3$ highlighting the corner-sharing $CoSb_6$ octahedrons that form a cage to accommodate a filler ion at the center.

5.2 Resonant Phonon Scattering

The loosely bound filler ions rattle inside the large interstitial voids, verified by their large atomic displacement parameter [5.4]. These rattlers induce local vibrational modes, which are mostly harmonic (Einstein oscillators). The localized phonon modes interact with normal phonon modes of the lattice, and thus lower the lattice thermal conductivity. The relationship between the filled skutterudite structure and the reduction of the lattice thermal conductivity has been successfully explained by the resonant phonon scattering mechanism [5.16]. Each filler ion acts as a resonant phonon scattering center with a particular frequency. Only those normal phonon modes with frequencies close to local resonant frequencies can interact strongly with the vibration modes of the fillers. Filling the skutterudite structure with multiple ions of different localized frequencies can scatter a broad wavelength spectrum of phonons, and thus significantly reduce lattice thermal conductivity. The difference in phonon resonant frequencies among fillers seems to be related to their chemical nature. Ba and Yb have larger difference in both spring constants and resonant frequencies than most of the other double-filler pairs for $CoSb_3$ [5.17]. Therefore, filling Ba and Yb into the voids of $CoSb_3$ should be most effective in scattering lattice phonons. Moreover, the filling fraction limits for Ba and Yb in $CoSb_3$ are well studied experimentally and theoretically, and both elements yield high ZTs as single-fillers [5.12][5.13][5.18].

5.3 Results and Discussions

In collaboration with Dr. Xun Shi, I studied thermoelectric properties of polycrystalline $Ba_xYb_yCo_4Sb_{12}$ compounds from 300 to 800 K. We found that double filling with Ba and Yb is more efficient in scattering lattice phonons than single-filled and other double-filled skutterudites, and hence leading to an enhanced ZT.

The pure constituent elements of $Ba_xYb_yCo_4Sb_{12}$ were weighed based on their stoichiometric compositions and melted in quartz tubes under vacuum. The skutterudite structure was formed using solid state reaction followed by a long annealing. The materials were condensed by spark plasma sintering after that. X-ray powder diffraction

spectra and EPMA analyses show nearly single phase except traces of a few percent of ytterbium oxide. Electrical conductivity, thermopower, and thermal conductivity measurements were carried out over the temperature range from 300K to 800K. High temperature electrical conductivity and Seebeck coefficient were measured in a home-built apparatus under protective argon atmosphere using R-type Pt-Pt/Rh thermocouples with the Pt legs serving also as resistive voltage probes. In the temperature range covered, fine thermocouple wires can be conveniently attached to the sample with silver paste. Thermal conductivity was determined from measurements of the thermal diffusivity in conjunction with the measurements of the specific heat and the sample density. The disks for the thermal diffusivity measurements were cut at places adjacent to the rectangular samples used for the resistivity and Seebeck coefficient. The Hall effect was measured from 5 to 300 K in a cryostat equipped with a 5.5 T superconducting magnet in order to determine the carrier concentration of the samples. More details regarding experimental setup of the measurements can be found in Chapter III.

The room temperature values of electronic and thermal transport properties of $Ba_xYb_yCo_4Sb_{12}$ samples are listed in Table 5.1. Fig. 5.3-5.5 display electrical conductivity, thermopower, and power factor of $Ba_xYb_yCo_4Sb_{12}$ from 300 to 800K. Fig. 5.6 and Fig. 5.7 show the temperature dependence of the Hall coefficient R_H and the carrier concentration n obtained from the relation $R_H=1/(ne)$. All the samples show heavily doped semiconductor behavior except $Ba_{0.03}Co_4Sb_{12}$. In Fig. 5.3, concentration of Ba seems to have more influence on electrical conductivity than that of Yb. The highest electrical conductivity values are obtained at the highest filling fractions of Ba with x close to 0.1. Increasing concentration of Ba has a small detrimental effect on the thermopower, as shown in Fig. 5.4. Due to the very low filling fraction of Ba, the compound of $Ba_{0.03}Co_4Sb_{12}$ has low carrier concentration of $0.50\times10^{20}cm^{-3}$ (see Fig. 5.7). It exhibits an early onset of the intrinsic regime of conduction at only 450 K (see Fig. 5.4). Double-filled samples have higher carrier concentration, causing a shift in the onset of intrinsic conduction to beyond 750 K. Overall, the power factor is greatly enhanced due to the double-filling, as shown in Fig. 5.5. The power factors of $Ba_{0.05}Yb_{0.09}Co_4Sb_{12.13}$ and $Ba_{0.08}Yb_{0.09}Co_4Sb_{12.12}$ reach close to 45 $\mu W/cm\text{-}K^2$ at about 750 K. Therefore, filling Ba in $CoSb_3$ is favorable to the electrical transport.

Table 5.1. Actual composition (measured by EPMA), thermal conductivity, lattice thermal conductivity, electrical conductivity, thermopower and electron density of $Ba_xYb_yCo_4Sb_{12}$ at 300K.

Actual composition	σ S/cm	S μV/K	$S^2\sigma$ μW/cm-K^2	κ W/m-K	κ_L W/m-K	n 10^{20}cm^{-3}	μ_H cm^2/V-s
$Ba_{0.03}Co_4Sb_{12.05}$	399	-219.6	19.2	5.41	5.11	0.50	58.5
$Ba_{0.15}Yb_{0.01}Co_4Sb_{12.08}$	1798	-125.2	28.2	4.34	3.02	2.79	38.4
$Ba_{0.11}Yb_{0.03}Co_4Sb_{12.07}$	1787	-114.9	23.6	3.21	1.89	3.65	31.6
$Yb_{0.12}Co_4Sb_{12.11}$	765.1	-145.8	16.3	2.72	2.16	2.34	20.1
$Ba_{0.05}Yb_{0.09}Co_4Sb_{12.13}$	1126	-157.6	28.0	2.82	1.99	2.91	24.2
$Ba_{0.08}Yb_{0.09}Co_4Sb_{12.12}$	2068	-125.9	32.8	2.52	1.00	3.18	35.6
$Ba_{0.11}Yb_{0.08}Co_4Sb_{12.08}$	2114	-107.3	24.3	2.40	0.86	4.36	31.1

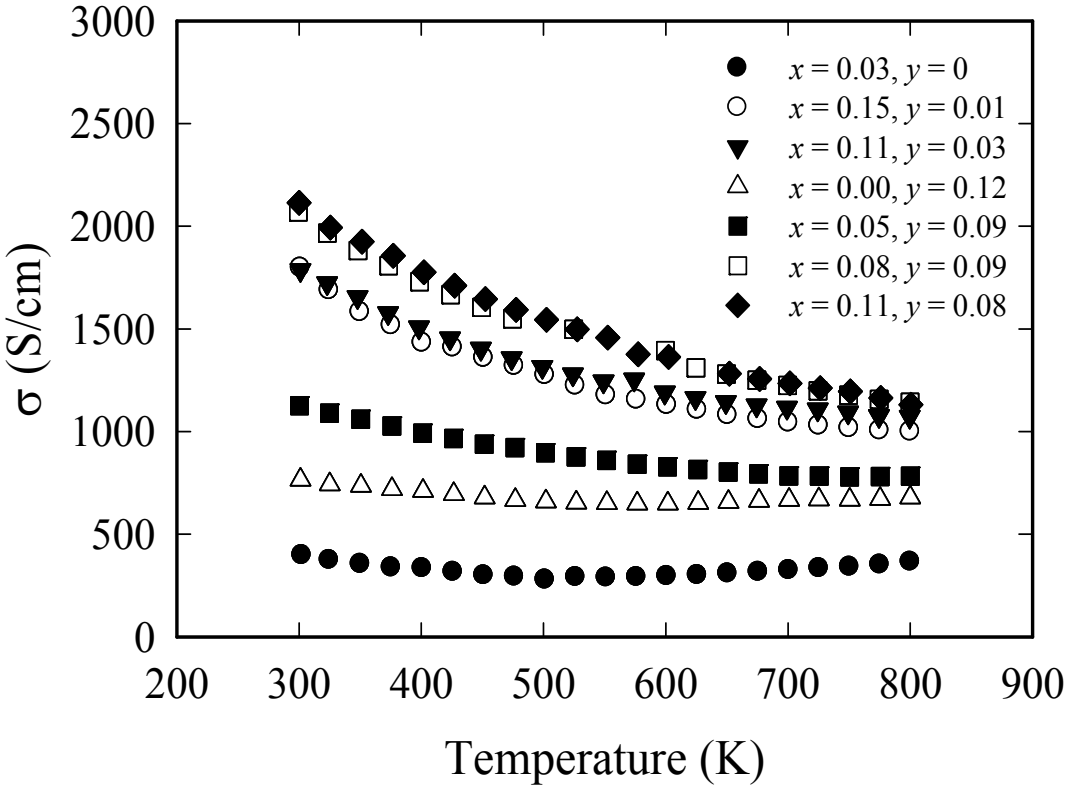

Fig. 5.3. Electrical conductivity of $Ba_xYb_yCo_4Sb_{12}$ skutterudites as a function of temperature from 300K to 800K.

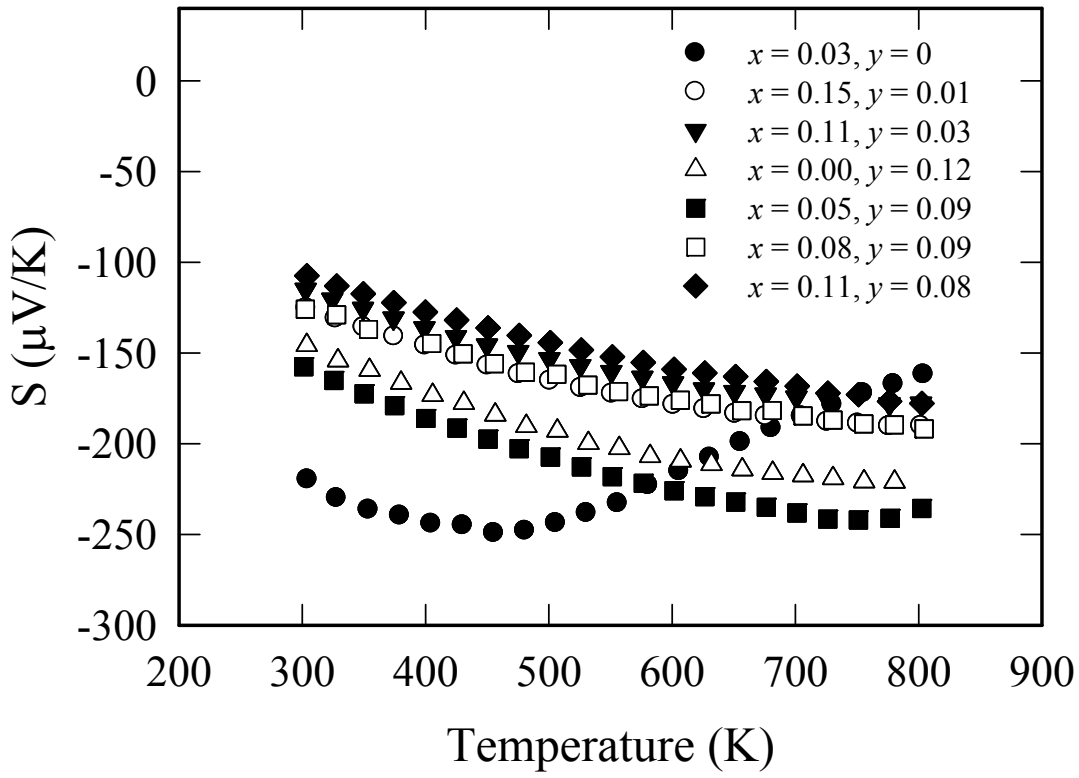

Fig. 5.4. Thermopower of $Ba_xYb_yCo_4Sb_{12}$ skutterudites as a function of temperature from 300K to 800K.

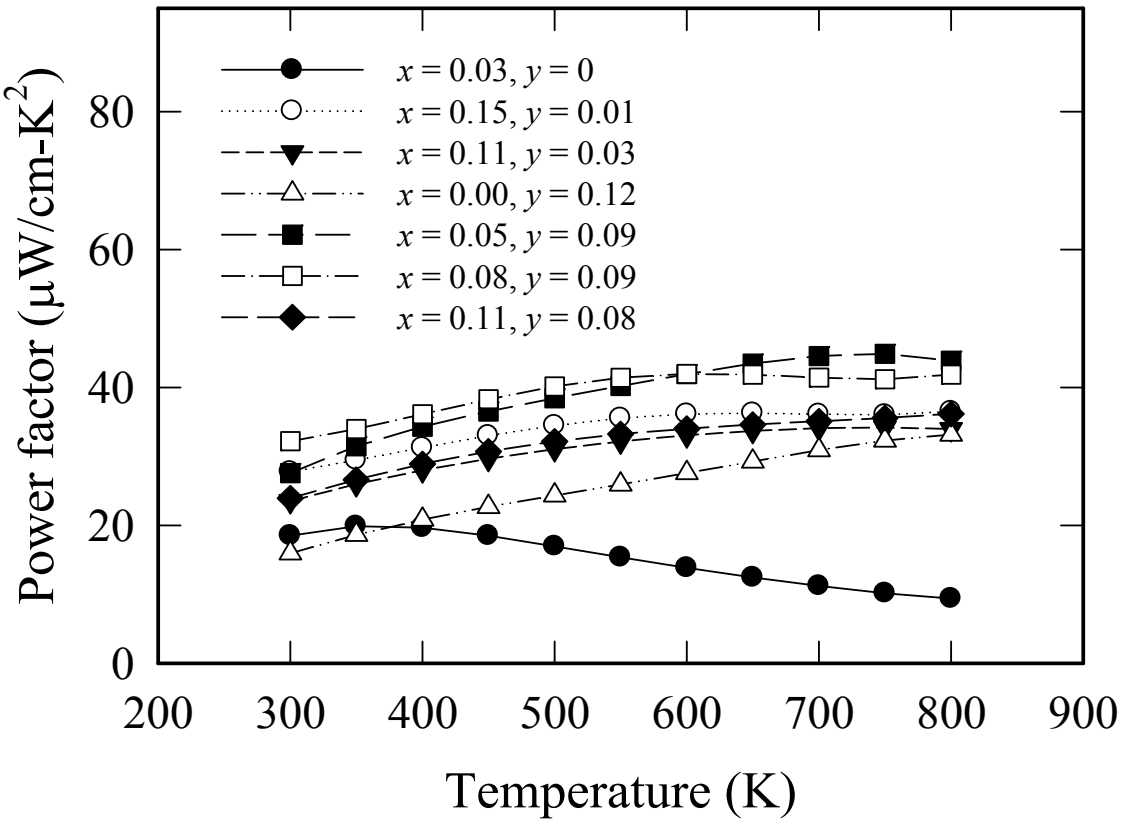

Fig. 5.5. Power factor of $Ba_xYb_yCo_4Sb_{12}$ skutterudites as a function of temperature from 300K to 800K.

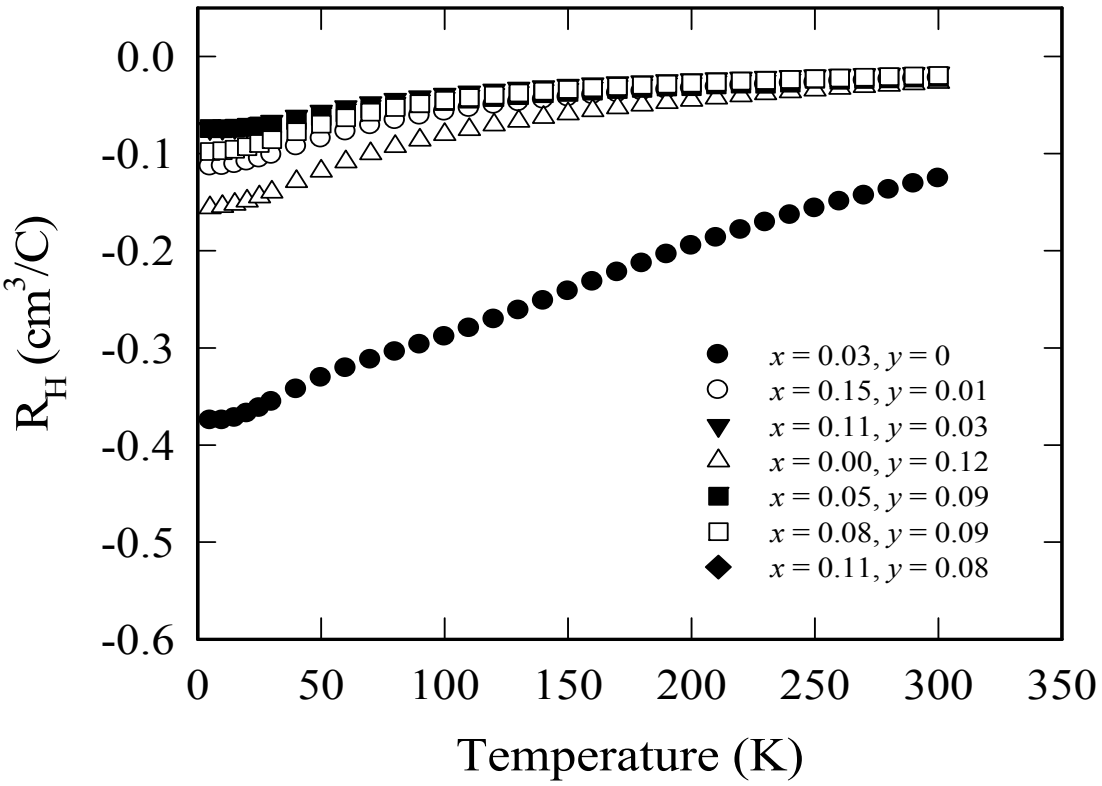

Fig. 5.6. Hall coefficient of $Ba_xYb_yCo_4Sb_{12}$ skutterudites as a function of temperature from 2K to 300K.

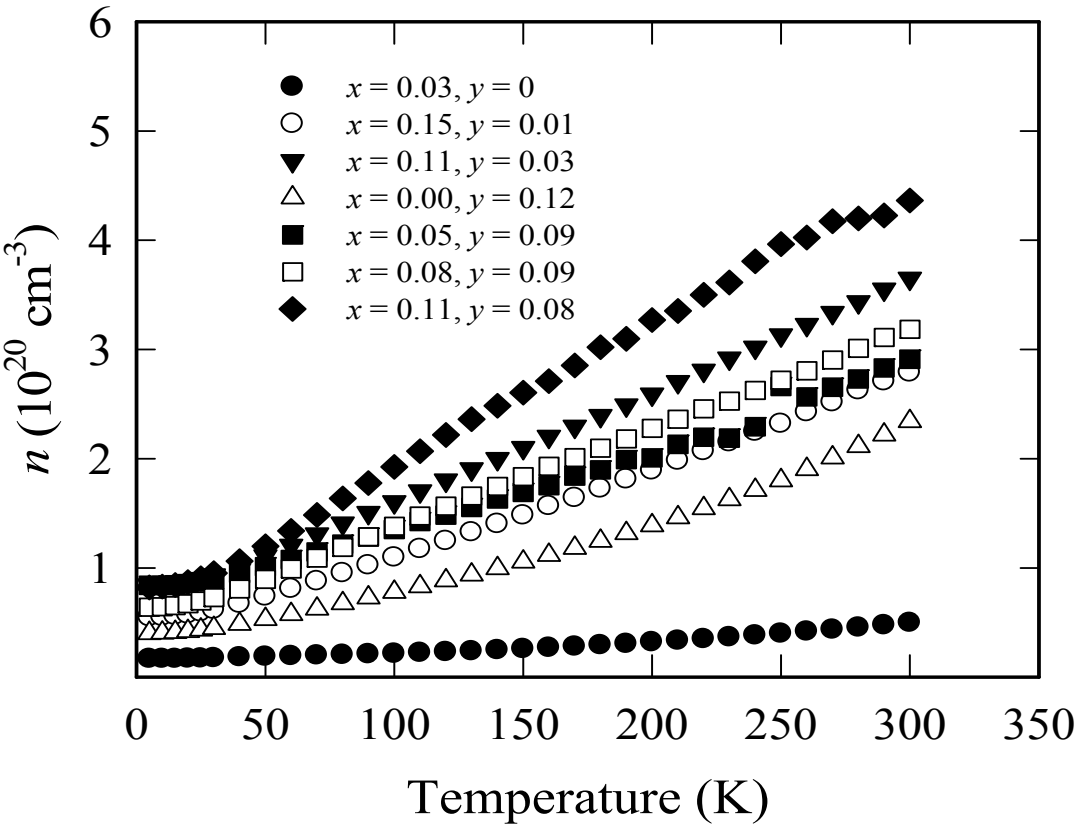

Fig. 5.7. Electron concentration of $Ba_xYb_yCo_4Sb_{12}$ skutterudites as a function of temperature from 2K to 300K.

Fig. 5.8 shows the total thermal conductivity as a function of temperature. The thermal conductivity is dominated by concentration of Yb. Samples with highest filling fraction of Yb ($y \sim 0.1$) possess the lowest thermal conductivity. The lattice thermal conductivity (κ_L) is computed by subtracting the electronic term from the total thermal conductivity (κ), in Table 5.1. The electronic term is calculated using the Wiedemann-Franz law with the Lorenz number equal to 2.45×10^{-8} V^2/K^2 for degenerate semiconductors. The lattice thermal conductivity of the Ba single-filled skutterudite is much higher, above 5 W/m-K for $Ba_{0.03}Co_4Sb_{12.05}$, than that of the Yb single-filled skutterudite, about 2.2 W/m-K for $Yb_{0.12}Co_4Sb_{12.11}$. In single-filled skutterudites, Yb is expected to be more effective than Ba in scattering low frequency (acoustic) phonons that dominate the heat conduction in solids due to the smaller ionic size of Yb [5.10, 5.12, 5.19]. The data also suggests that the combination of the two fillers, Ba and Yb, reduces the lattice thermal conductivity much more than single-filled ones. In double-filled skutterudites, Ba is observed to be quite effective in scattering phonons. For the last 3 double-filled samples (see Table 5.1) with similar Yb concentration ($y \sim 0.09$), the lattice thermal conductivity decreases significantly as the Ba concentration increases. For low Yb content samples such as $Ba_{0.15}Yb_{0.01}Co_4Sb_{12.08}$, its lattice thermal conductivity is quite high, above 3 W/m-K at room temperature (Table 5.1). Low Yb concentration in double-filled skutterudites appears to result in high lattice thermal conductivity.

Figure 5.9 plots the lattice thermal conductivity κ_L as a function of the total filling fraction $x+y$ in $Ba_xYb_yCo_4Sb_{12}$ double-filled skutterudites. Although we subtract the highest possible value of the electronic thermal conductivity as implied by the fully degenerate value of the Lorenz number, the resulting lattice thermal conductivity is useful for cross comparison purposes. We observe a monotonic decrease in κ_L with an increasing filling fraction ($x+y$) for all double-filled skutterudite samples except $Ba_{0.15}Yb_{0.01}Co_4Sb_{12.08}$. The thermal conductivities of other double-filled skutterudites reported in Ref. 5.17 are also included in the plot for comparison. $Ba_xYb_yCo_4Sb_{12}$ samples have smaller lattice thermal conductivity than other double-filled skutterudites. The calculated resonance frequencies for Ba and Yb in $CoSb_3$ are 42 cm^{-1} and 93 cm^{-1} in the [1 1 1] direction, and 43 cm^{-1} and 94 cm^{-1} in the [1 0 0] direction, respectively [5.17]. The resonant frequencies of the two species differ in both directions by more than a factor

of two. This large difference in resonance frequencies broadens the spectrum of phonons that undergo scattering, hence reducing lattice thermal conductivity. Our data also suggest that there is interplay in phonon scattering by Ba and Yb fillers in $CoSb_3$. This is originated from the coulombic nature of the primary interaction between the fillers in the skutterudite structure [5.18]. An additional reduction in κ_L could presumably be achieved by multiple filling using ions covering a wide range of resonant frequencies and strong correlations among various filler ions.

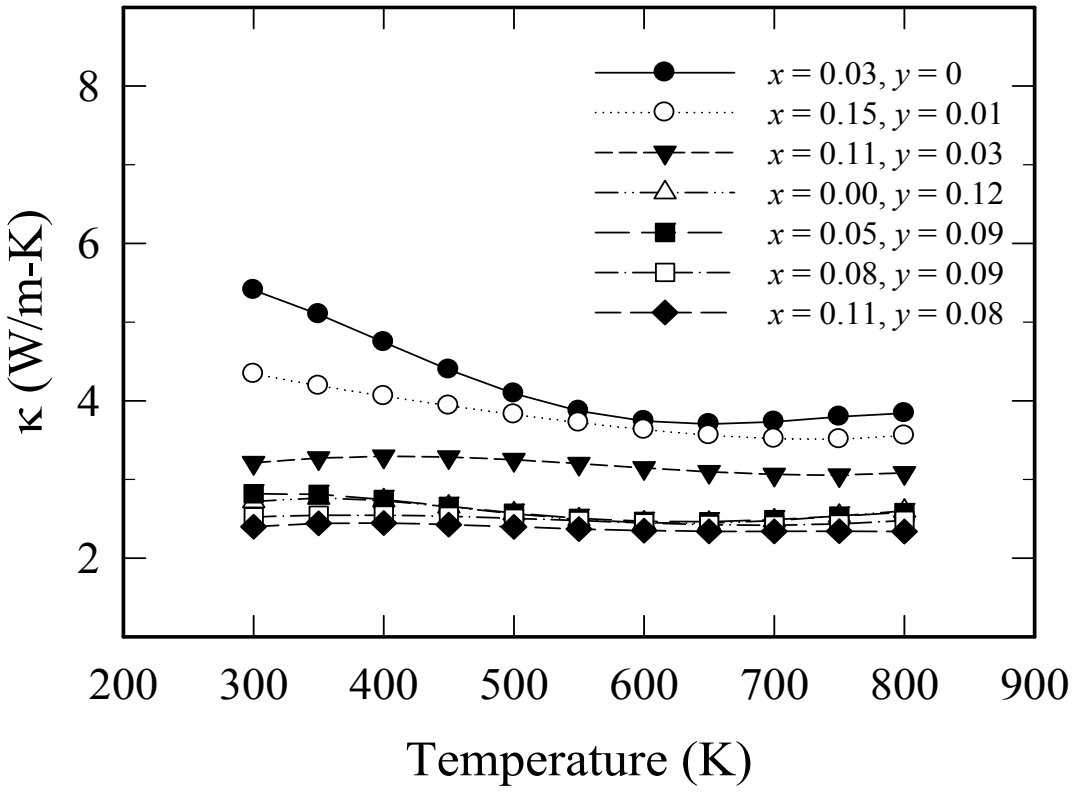

Fig. 5.8. Total thermal conductivity of $Ba_xYb_yCo_4Sb_{12}$ skutterudites as a function of temperature from 300K to 800K.

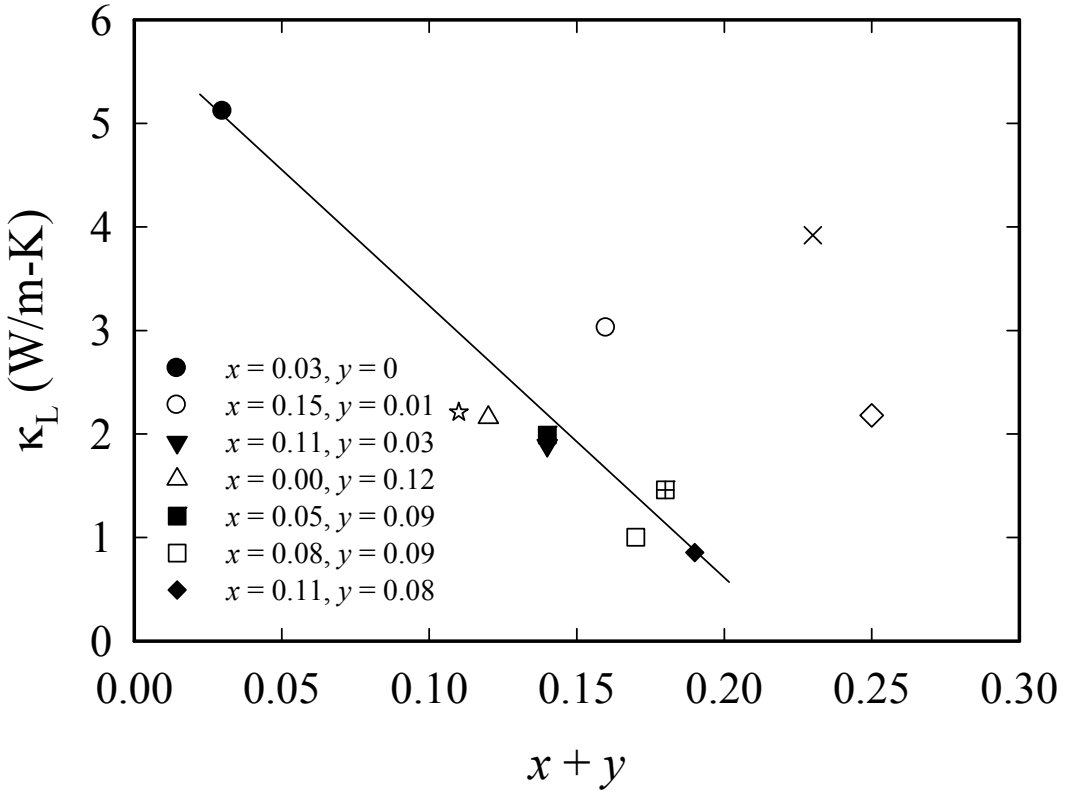

Fig. 5.9. Lattice thermal conductivity as a function of total filling fraction (x+y) for $Ba_xYb_yCo_4Sb_{12}$ skutterudites. The solid line is a guide for eyes. The thermal conductivities of $Ba_{0.23}Co_4Sb_{12.10}$ (×), $Ba_{0.07}La_{0.04}Co_4Sb_{12.08}$ (☆), $Ba_{0.12}Ce_{0.06}Co_4Sb_{12.08}$ (⊞), and $Ba_{0.17}Sr_{0.08}Co_4Sb_{12.07}$ (◇) from Ref. 5.17 are also shown in the above figure.

Compared to filling the voids of $CoSb_3$ with Ba or Yb only, filling with both Ba and Yb leads to higher power factors ($S^2\sigma$) and much lower thermal conductivity (κ). The dimensionless thermoelectric figure of merit (ZT) of $Ba_xYb_yCo_4Sb_{12}$ is calculated from the relation $ZT = S^2\sigma T/\kappa$ from 300 K to 800 K, as shown in Fig. 5.10. In particular, $Ba_{0.08}Yb_{0.09}Co_4Sb_{12.12}$ exhibits a ZT of 1.0 at 600 K, and 1.36 at 800 K. The ZT of $Ba_{0.05}Yb_{0.09}Co_4Sb_{12.13}$ reaches the maximum of 1.35 at 800 K. Both compounds have higher ZT than Ba single-filled and Yb single-filled skutterudites [5.12-5.13]. Filling multiple ions with different resonant frequency in cage-like structures such as skutterudites, is demonstrated to be effective in reducing the lattice thermal conductivity in $Ba_xYb_yCo_4Sb_{12}$.

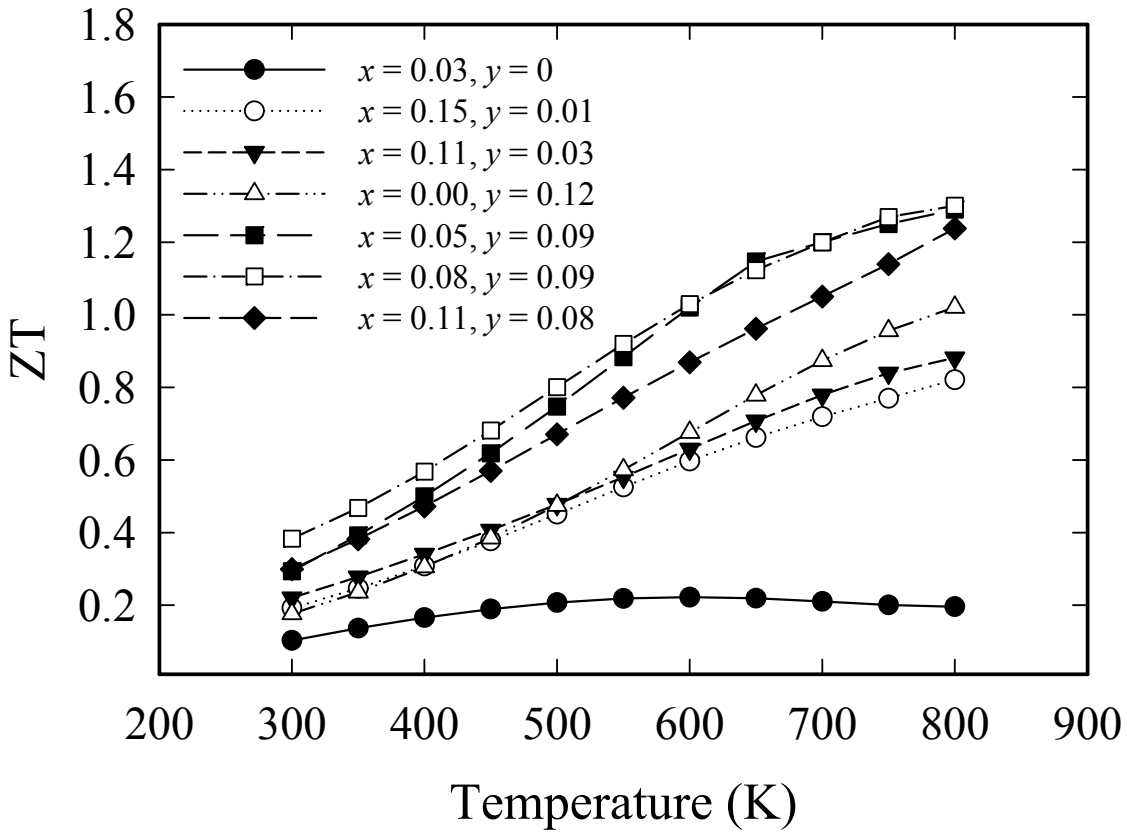

Fig. 5.10. The dimensionless figure-of-merit ZT of $Ba_xYb_yCo_4Sb_{12}$ skutterudites as a function of temperature from 300K to 800K.

5.4 Conclusions and Future Work

The high temperature thermoelectric properties are studied for a series of $Ba_xYb_yCo_4Sb_{12}$ double filled skutterudites. These materials exhibit very good electronic transport properties and very low lattice thermal conductivity. The dimensionless figure of merit ZT increases to 1.36 by double-filling the voids of the $CoSb_3$ lattice with Ba and Yb. Lattice thermal conductivity appears to decrease with the total filling fraction $x+y$ for $Ba_xYb_yCo_4Sb_{12}$. To further reduce lattice thermal conductivity, higher filling fractions for both Ba and Yb are desired. There is still space for improvements within the filling fraction limit.

Besides Yb, other rare earth atoms also have large difference in phonon resonant frequency with respect to Ba. The calculated resonance frequencies for Ce and Eu in $CoSb_3$ are 54 cm^{-1} and 58 cm^{-1} in the [1 1 1] direction, and 55 cm^{-1} and 59 cm^{-1} in the [1 0 0] direction, respectively [5.17]. As noted previously, the calculated resonance frequencies for Ba are 93 cm^{-1} in the [1 1 1] direction and 94 cm^{-1} in the [1 0 0] direction. Both Ce and Eu differ in two directions by a factor of 1.7 with Ba. They can be tried as alternatives to Yb in double-filled $CoSb_3$. Based on the same principle as double-filling, a third filler atom could be introduced into the voids of $CoSb_3$ lattice in order to expand the resonant phonon scattering spectrum further. Therefore, tri-filled skutterudites may achieve lower lattice thermal conductivity than their double-filled counterparts. The third filler also contributes extra valence electrons, which may improve power factor. Complications such as filling fraction limits and secondary phases are, however, likely to arise from adding multiple fillers in $CoSb_3$.

References to Chapter V

5.1 C. Uher, in Recent Trends in Thermoelectric Materials Research I, Semiconductors and Semimetals, Vol. **69**, edited by T. M. Tritt (Academic Press, San Diego 2001), p. 139-253 and references therein
5.2 G. A. Slack, V. G. Tsoukala, J. Appl. Phys. **76**, 1665 (1994)
5.3 D. T. Morelli and G. P. Meisner, J. Appl. Phys. **77**, 3777 (1995)
5.4 B. C. Sales, D. Mandrus, and R. K. Williams, Science **272**, 1325 (1996)
5.5 B. Chen, J. Xu, C. Uher, D. T. Morelli, G. P. Meisner, J. Fleurial, T.Caillat, and A. Borshchevsky, Phys. Rev. B **55**, 1476 (1997)
5.6 V. L. Kuznetsov, L. A. Kuznetsova, D. M. Rowe, J. Phys.: Condens. Matter **15**, 5035 (2003)
5.7 G. S. Nolas, J. L. Cohn, G. A. Slack, Phys. Rev. B **58**, 164 (1998)
5.8 G. A. Lamberton, Jr., S. Bhattacharya, R. T. Littleton IV, M. A. Kaeser, R. H. Tedstrom, T. M. Tritt, J. Yang, G. S. Nolas, Appl. Phys. Lett. **80**, 598 (2002)
5.9 D. T. Morelli, G. P. Meisner, B. Chen, S. Hu, C. Uher, Phys. Rev. B **56**, 7376 (1997)
5.10 J. Yang, D. T. Morelli, G. P. Meisner, W. Chen, J. S. Dyck, C. Uher, Phys. Rev. B **67**, 165207 (2003)
5.11 Y. Z. Pei, L. D. Chen, W. Zhang, X. Shi, S. Q. Bai, X. Y. Zhao, Z. G. Mei, X. Y. Li, Appl. Phys. Lett. **89**, 221107 (2006)
5.12 G. S. Nolas, M. Kaeser, R. T. Littleton IV, T. M. Tritt, Appl. Phys. Lett. **77**, 1855 (2000).
5.13 L. D. Chen, T. Kawahara, X. F. Tang, T. Goto, T. Hirai, J. S. Dyck, W. Chen, C. Uher, J. Appl. Phys. **90**, 1864 (2001)
5.14 M. Puyet, B. Lenoir, A. Dauscher, P. Pécheur, C. Bellouard, J. Tobola, J. Hejtmanek, Phys. Rev. B **73**, 035126 (2006)
5.15 M. Puyet, B. Lenoir, A. Dauscher, M. Dehmas, C. Stiewe, E. Müller, J. Appl. Phys. **95**, 4852 (2004)
5.16 G. J. Long, R. P. Hermann, F. Grandjean, E. E. Alp, W. Sturhahn, C. E. Johnson, D. E. Brown, O. Leupold, R. Rüffer, Phys. Rev. B **71**, 140302 (R) (2005)
5.17 J. Yang, W. Zhang, S. Q. Bai, Z. Mei, L. D. Chen, Appl. Phys. Lett. **90**, 192111 (2007)
5.18 X. Shi, W. Zhang, L. D. Chen, J. Yang, Phys. Rev. Lett. **95**, 185503 (2005)
5.19 N. R. Dilley, E. D. Bauer, M. B. Maple, B. C. Sales, J. Appl. Phys. **88**, 1948 (2000)

Chapter VI
Rare Earth-Ruthenium-Germanium Compounds

In chapter V, I discussed that skutterudites are excellent thermoelectric materials which have optimized performance at intermediate temperatures from 600 K to 900 K. By filling their cage-like structure with different foreign atoms, we have demonstrated that ZT can be increased up to about 1.4. Other bulk materials such as clathrate compounds have been shown to possess similar structures [6.1-6.7]. A family of ternary germanides, $R_3T_4Ge_{13}$ (R = Rare Earth, T = Transition Metal) were first studied for its superconducting properties [6.8]. Since $R_3T_4Ge_{13}$ adopts structures similar to filled skutterudites, we were interested in exploring the potential of these compounds as prospective thermoelectrics. Some of the compounds in the R-Ru-Ge system exhibit magnetism attributed to the unpaired *f*-shell electrons of rare earth atoms. Thus, I also studied the magnetic properties of these compounds. In this chapter, the systems of $R_3Ru_4Ge_{13}$ (where R = Y, Ho, Dy, Lu) and $Y_3(Ru_{1-x}Co_x)_4Ge_{13}$ (where x = 0, 0.1, and 0.2) are discussed.

6.1 Crystal Structure

The rare earth-ruthenium-germanium ($R_3Ru_4Ge_{13}$) compounds crystallize in the space group $Pm3n$ with the $R_3T_4Sn_{13}$ (R = rare earth, T = transition metal) structure-type [6.9]. The Ge1, *R*, Ru, and Ge2 atoms occupy the 2*a*, 6*d*, 8*e*, and 24*k* sites, respectively [6.10-6.11]. The $R_3Ru_4Ge_{13}$ structure consists of three substructures: edge-sharing $Ge1(Ge2)_{12}$ icosahedra, *R*-centered cuboctahedra $R(Ge2)_{12}$, and corner-sharing $Ru(Ge2)_6$ trigonal prisms. The corner-sharing $Ru(Ge2)_6$ trigonal prisms create "cages" containing a Ge1 atom. A structure like this is analogous to the TPn_6 (T = transition metal; Pn = pnicogen atom) octahedral arrangement found in filled skutterudite compounds such as $LaFe_4P_{12}$ [6.9]. This interesting feature is favorable to low thermal conductivity as demonstrated in

filled skutterudites [6.12]. Therefore, it was of interest to find out whether the rare earth-ruthenium-germanium compounds might possess good thermoelectric properties as well.
As discussed in Ref. 6.13, a substitution of a germanium atom for one of the rare earth atoms in $R_3Ru_4Ge_{13}$ is possible and, in fact, this compound represents the end composition of the continuous solid solution between $R_3Ru_4Ge_{13}$ and $RRuGe_3$, i.e., $R_{4-x}Ru_4Ge_{12+x}$ ($0 < x < 1$). Furthermore, these compounds seem to display some kind of internal disorder. Large values of anisotropic x-ray displacement (thermal) parameters were observed for both Ge1 (2*a*) and Ge2 (24*k*) sites, indicating a partial disordering of the $Ge1(Ge2)_{12}$ icosahedra holes [6.8]. Both the internal "disorder" and cage-like structure are favorable to low lattice thermal conductivity in these compounds.

6.2 Experimental Methods

Two sets of samples were synthesized by arc melting. The first set consisted of samples of composition $R_3Ru_4Ge_{13}$ with R = Y, Dy, Ho, and Lu; the second set of samples were of composition $Y_3(Ru_{1-x}Co_x)_4Ge_{13}$ with x = 0, 0.1, and 0.2. For each of these samples, stoichiometric quantities of the elements were placed on a water cooled hearth and remelted at least six times under flowing argon to ensure the sample's homogeneity. Following the procedures reported in Ref. 6.11, the resulting buttons were sealed in quartz tubes under vacuum and annealed for a period of two weeks at 900 °C before quenching in cold water. The heat treatment effectively removes the impurity phases.
For susceptibility measurements, a small piece of each sample (~50 mg) was placed in polyethylene capsule inside a straw and positioned inside a Quantum Design magnetometer. Susceptibility was measured as a function of temperature using an applied field of 0.1 Tesla except for the Dy and Ho-based samples for which the applied field was 0.01 Tesla; the straw and empty capsule were measured separately in order to apply a background correction to the data. Smaller magnetic fields were selected for Dy and Ho-based samples because the signals for these two were much stronger than other samples.
Thermal and electrical transport properties were measured over the temperature range of 2 K – 800 K using two separate systems. Below room temperature we used a steady state method to measure thermal conductivity and thermopower; electrical resistivity and Hall

coefficient were measured using a low frequency AC bridge on samples placed in a liquid helium cryostat equipped with a superconducting magnet. High temperature values of electrical resistivity and Seebeck coefficient were obtained using an in-house apparatus. The sample is located in the center of a cylindrical oven that is enclosed under a glass bell jar evacuated and backfilled with argon gas. The bar-shaped sample is sandwiched between tungsten pillars with the aid of silver paint that serve as current contacts. The top tungsten pillar holds a small wire-wound heater with which one can establish a temperature gradient along the sample length. The temperatuare gradient is measured with fine R-type (Pt–Pt/Rh) thermocouples (Omega) and the Pt legs are used to pick up the longitudinal voltages (Seebeck voltage and resistive voltage, respectively). The measured temperatures are referenced to an Omega Ice Point Calibration Cell. The data collection process is automated by a LabVIEW program. To check the consistency, samples are measured for both heating and cooling cycles.

Since the samples prepared by arc melting were made with rather small quantities of the material, the button-shaped samples were too small to cut out disks of suitable size to measure thermal diffusivity which, in conjunction with the sample density and specific heat, would allow us to determine high temperature thermal conductivity. These properties were later studied for other batches in this series which were fabricated in the same fashion. More details regarding the experimental methods can be found in Chapter II.

6.3 Results and Discussions of $R_3Ru_4Ge_{13}$ (R = Y, Dy, Ho, and Lu) Samples

6.3.1 Structural Characterization

Powder X-ray diffraction data is collected using a SCINTAG X-ray diffractometer with Cu K_α radiation, wavelength λ = 1.540562 Å. The spectrum of $R_3Ru_4Ge_{13}$ samples revealed that all specimens after annealing were nearly single phase. The measured lattice constants are in good agreement with previously published values [6.8, 6.13]. For $Y_3Ru_4Ge_{13}$, the measured lattice constant a = 8.967 ± 0.001 Å, very close to the

published value 8.962 Å. EPMA analyses on the samples identified the secondary phases as Ru_2Ge_3 and pure Ge.

Table 6.1. The nominal composition and the measured lattice constants for $R_3Ru_4Ge_{13}$ (R = Y, Ho, Dy, and Lu) compounds.

Nominal Composition	Lattice constant a (Å)
$Y_3Ru_4Ge_{13}$	8.967
$Ho_3Ru_4Ge_{13}$	8.941
$Dy_3Ru_4Ge_{13}$	8.939
$Lu_3Ru_4Ge_{13}$	8.914

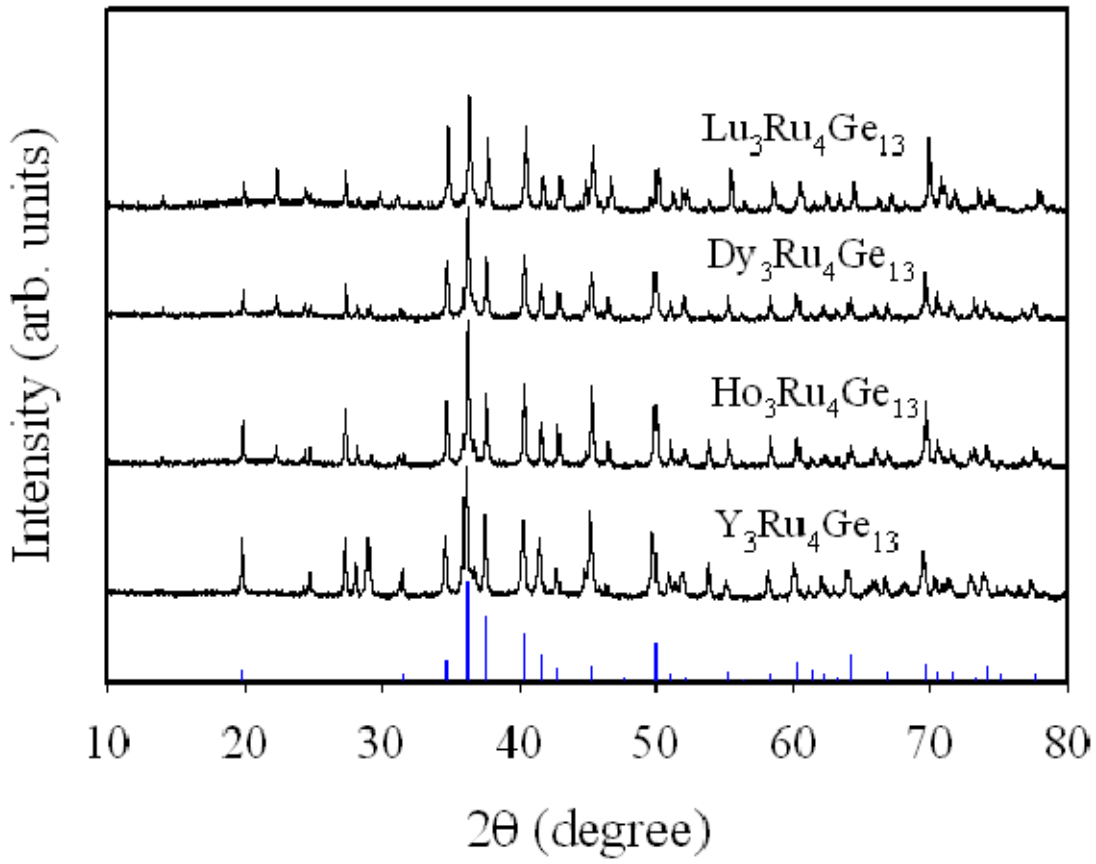

Fig. 6.1. The X-ray powder diffraction pattern of different samples $R_3Ru_4Ge_{13}$ (R = Y, Ho, Dy, and Lu). For comparison, the calculated pattern (blue) based on the crystal structure is plotted at the bottom. The results show that the sample is nearly single phase.

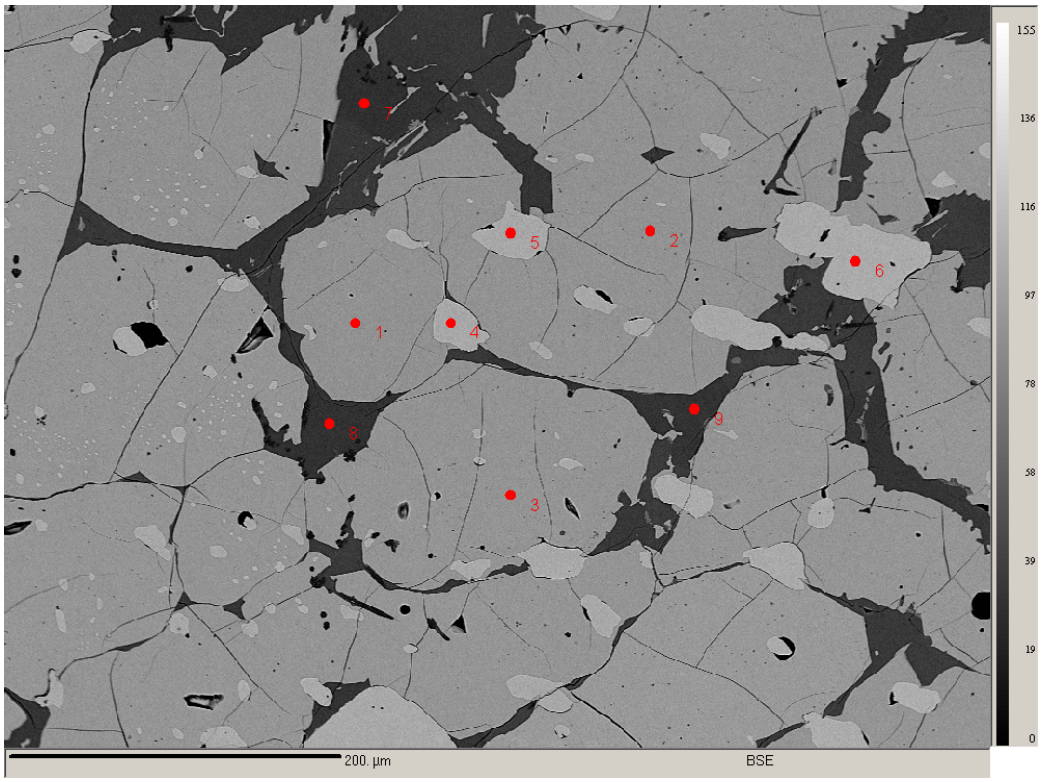

Fig. 6.2. The electron microprobe image of the sample $Y_3Ru_4Ge_{13}$. The grey areas (mapped by point 1, 2, 3) represent the primary phase of $Y_3Ru_4Ge_{13}$; the milky white areas (mapped by point 4, 5, 6) represent Ru_2Ge_3; the dark areas (mapped by point 7, 8, 9) represent pure Ge.

6.3.2 Magnetic Susceptibility

Figures 6.3, 6.4 and 6.5 show the magnetic susceptibility per gram of sample and its inverse per mole of *R* ion as a function of temperature for our samples. The Dy- and Ho-based compounds are paramagnetic obeying the Curie-Weiss law

$$\chi^{-1} = \frac{3k_B}{N\mu_{eff}^2}\left(T - \theta_{cw}\right) \tag{6.3.1}$$

where χ is the magnetic susceptibility; N is the number of magnetic ions (N = Avogadro's constant per mole of R ion); μ_{eff} is the effective magnetic moment per magnetic ion; and θ_{cw} is the Curie-Weiss temperature. From the linear fits of the inverse of the magnetic susceptibility using Currie-Weiss law, the calculated μ_{eff} for the Dy- and Ho-based samples are 10.5 and 11.6 Bohr magnetons (μ_B) per R ion, respectively, which are close to the theoretical value of 10.6 μ_B for the free trivalent ion R^{3+}. These observed values, in good agreement with Ref. 6.8, suggest that Dy and Ho ions are most likely in a trivalent state. As shown in Fig. 6.5, the Y-based sample is diamagnetic throughout the temperature range, and the Lu-based sample is diamagnetic through most of the temperature range, with a weak Curie "tail" which is almost 3 orders of magnitude lower than Dy- and Ho-based samples. We think it is due to the presence of another rare earth at an impurity level. We conclude that for the Dy- and Ho-based samples, the R ion is in the trivalent state.

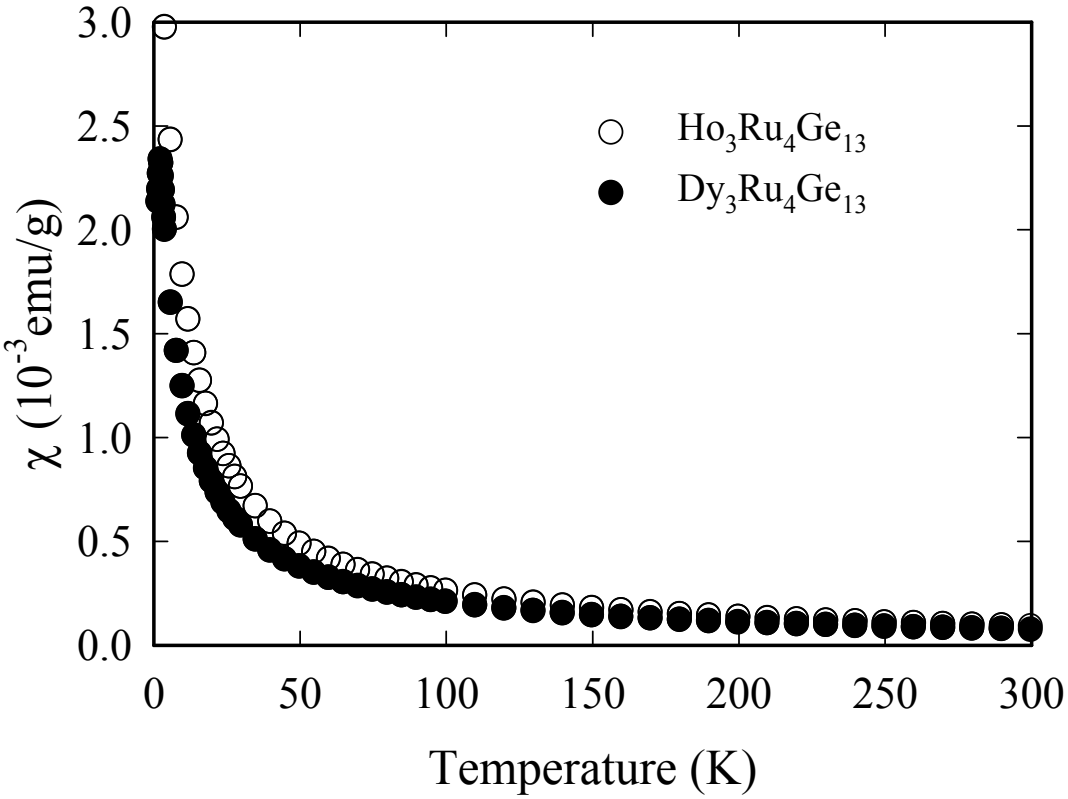

Fig. 6.3. Magnetic susceptibility at 0.01 T applied field of $Ho_3Ru_4Ge_{13}$ and $Dy_3Ru_4Ge_{13}$ as a function of temperature from 2 K to 300 K.

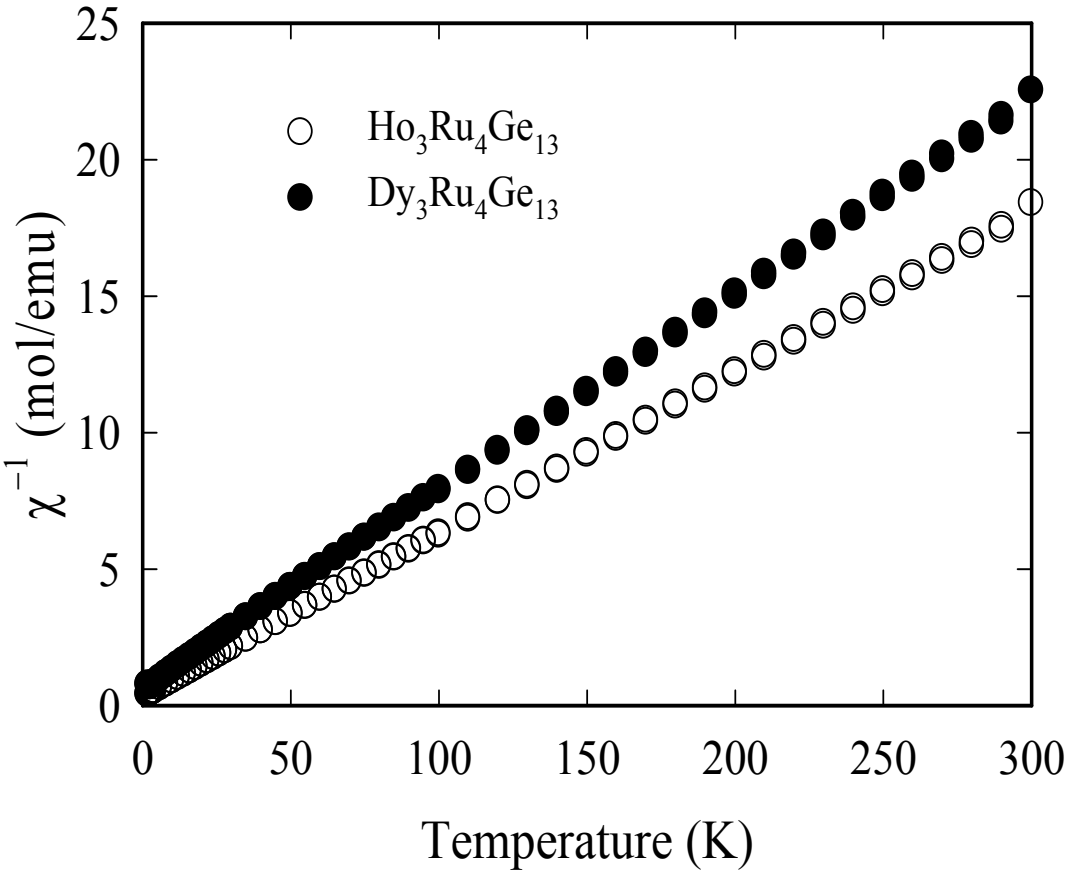

Fig. 6.4. The inverse of magnetic susceptibility at 0.01 T applied field of $Ho_3Ru_4Ge_{13}$ and $Dy_3Ru_4Ge_{13}$ as a function of temperature from 2 K to 300 K.

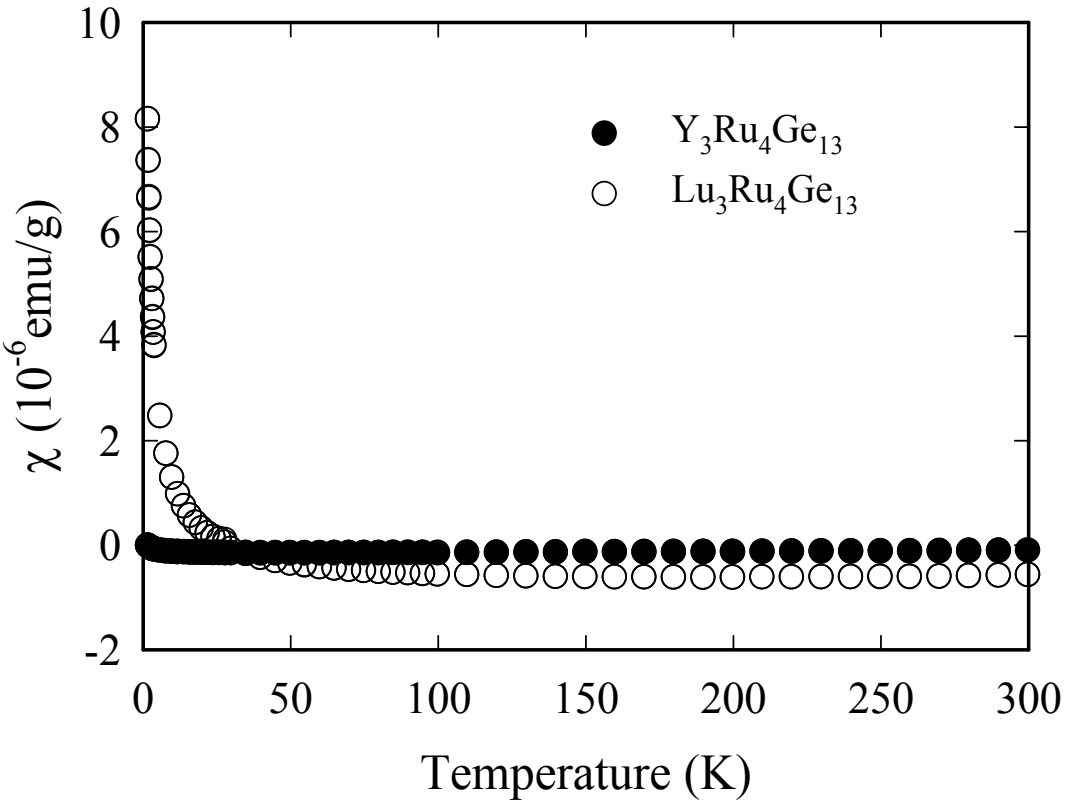

Fig. 6.5. Magnetic susceptibility at 0.1 T applied field of $Y_3Ru_4Ge_{13}$ and $Lu_3Ru_4Ge_{13}$ as a function of temperature from 2 K to 300 K.

.

6.3.3 Thermoelectric Properties

Figure 6.6 displays the electrical resistivity of our samples from 2 to 300 K. In agreement with Ref. 6.11, we observe a rise in resistivity with decreasing temperature on all samples, which indicates a semiconducting behavior. The magnitude of the resistivity is much larger than a typical metal and is similar to that of a heavily doped semiconductor or semimetal. The Hall coefficient measured at 1 T for these samples is on the order of +0.005 cm^3 C^{-1} except Lu sample has much higher value (in Fig. 6.10). This is reasonable because the extra valence electrons Lu donates offset the hole concentration. For a single carrier system, carrier concentration n can be obtained from the relation $R_H = \frac{1}{ne}$, which gives a hole concentration of approximately 10^{21} cm^{-3}. However, these materials are possibly semimetals and the small Hall coefficient may arise from a partial cancellation of electron and hole contributions. Further work in this area is required. In Fig. 6.7, we also observe a positive and modestly large Seebeck coefficient for all compounds that tends to saturate near 300 K at values between +35 and +40 μV/K.

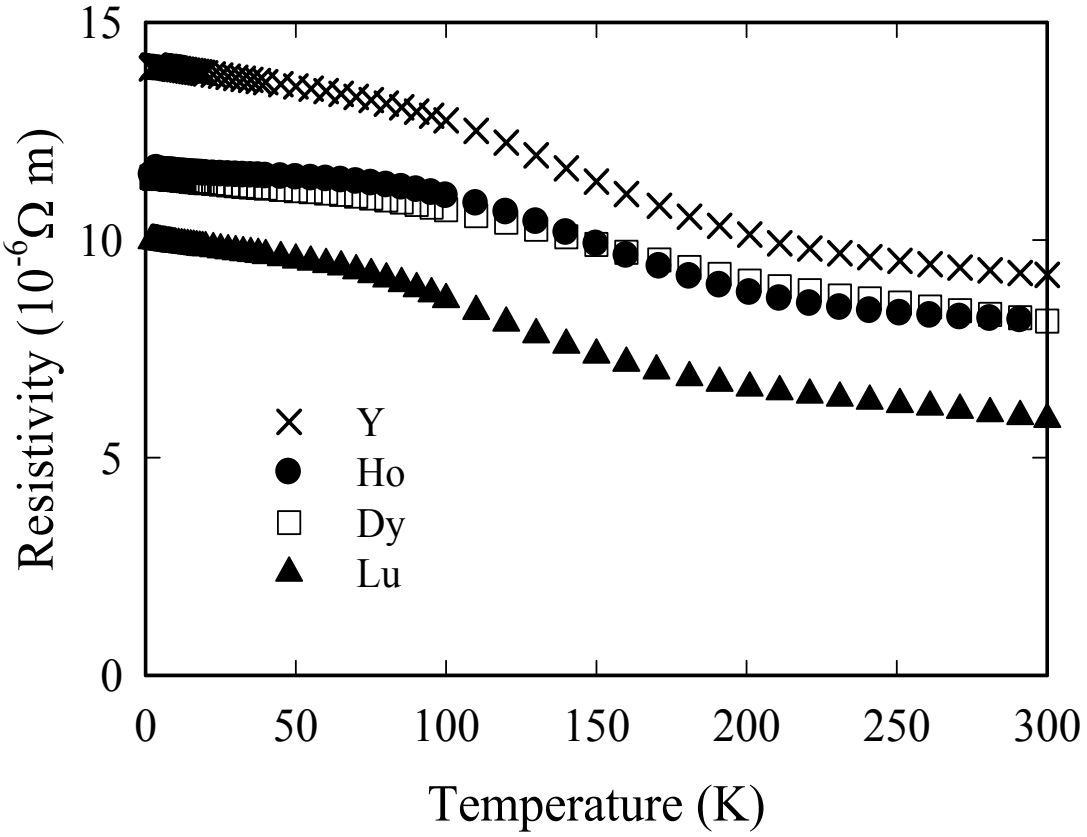

Fig. 6.6. Electrical resistivity of four different $R_3Ru_4Ge_{13}$ compounds as a function of temperature from 2 K to 300 K.

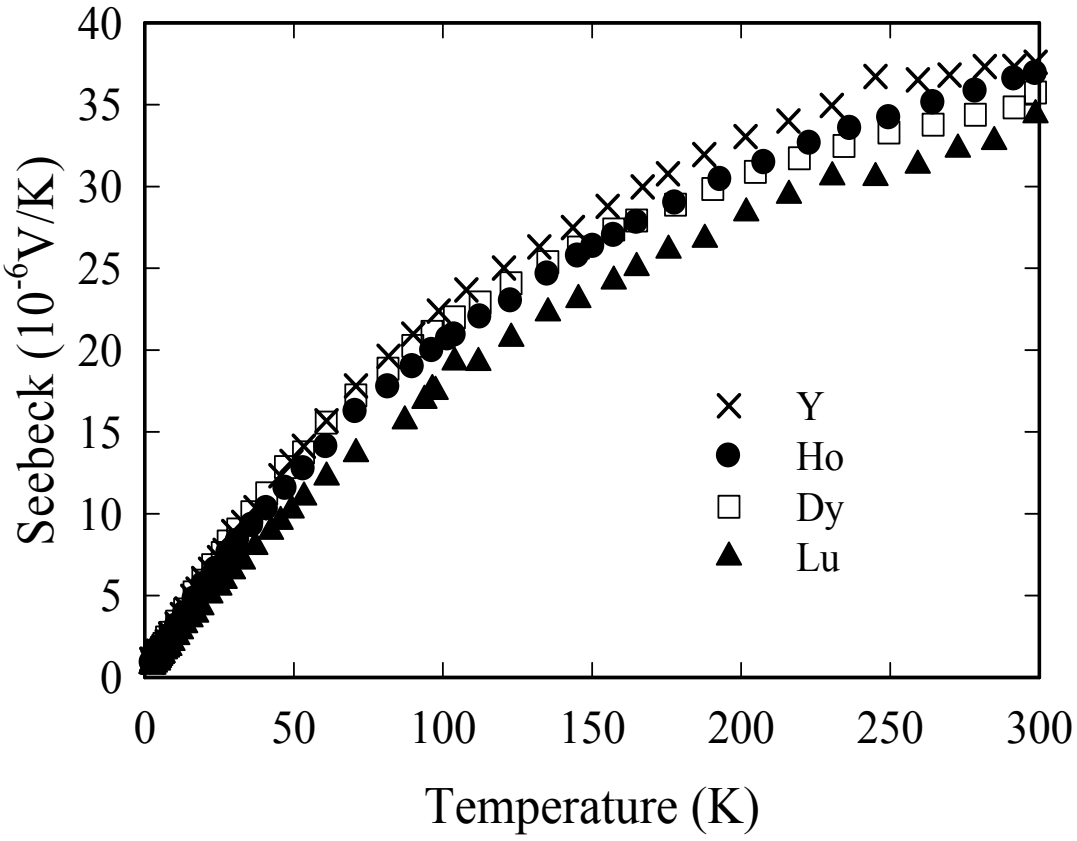

Fig. 6.7. Seebeck coefficient of four different $R_3Ru_4Ge_{13}$ compounds as a function of temperature from 2 K to 300 K.

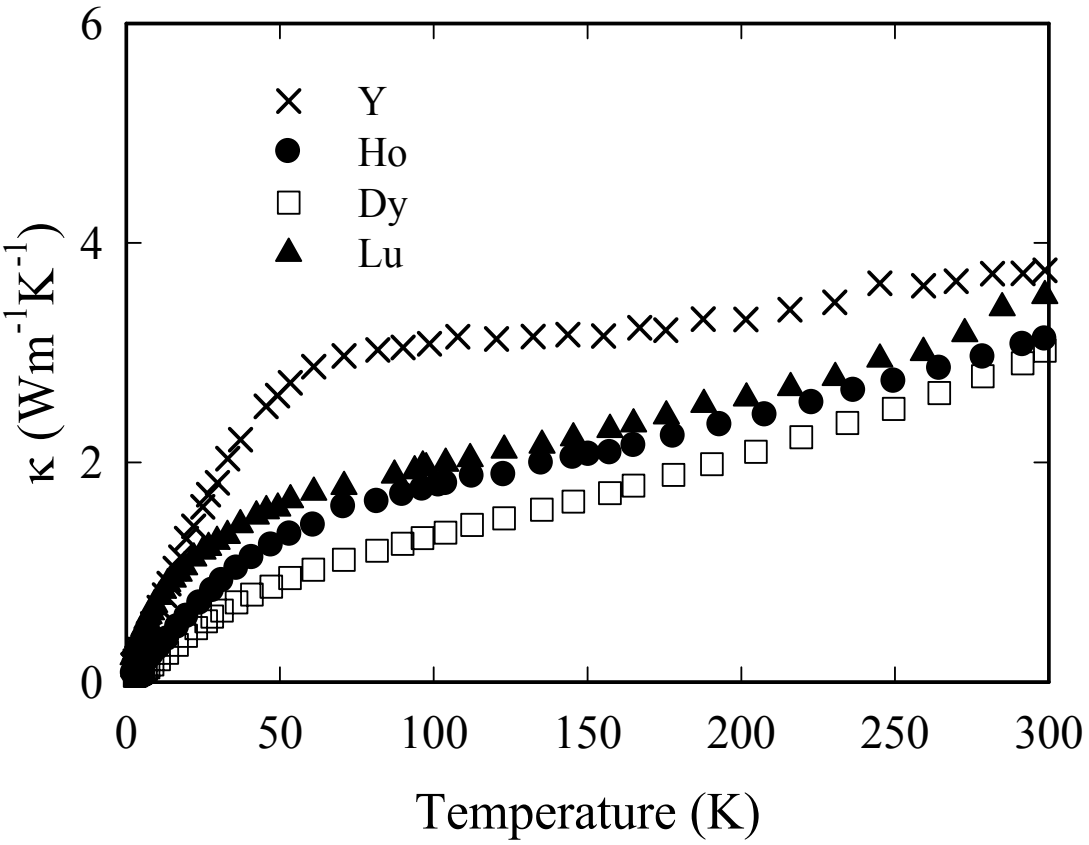

Fig. 6.8. Total thermal conductivity of four different $R_3Ru_4Ge_{13}$ compounds as a function of temperature from 2 K to 300 K.

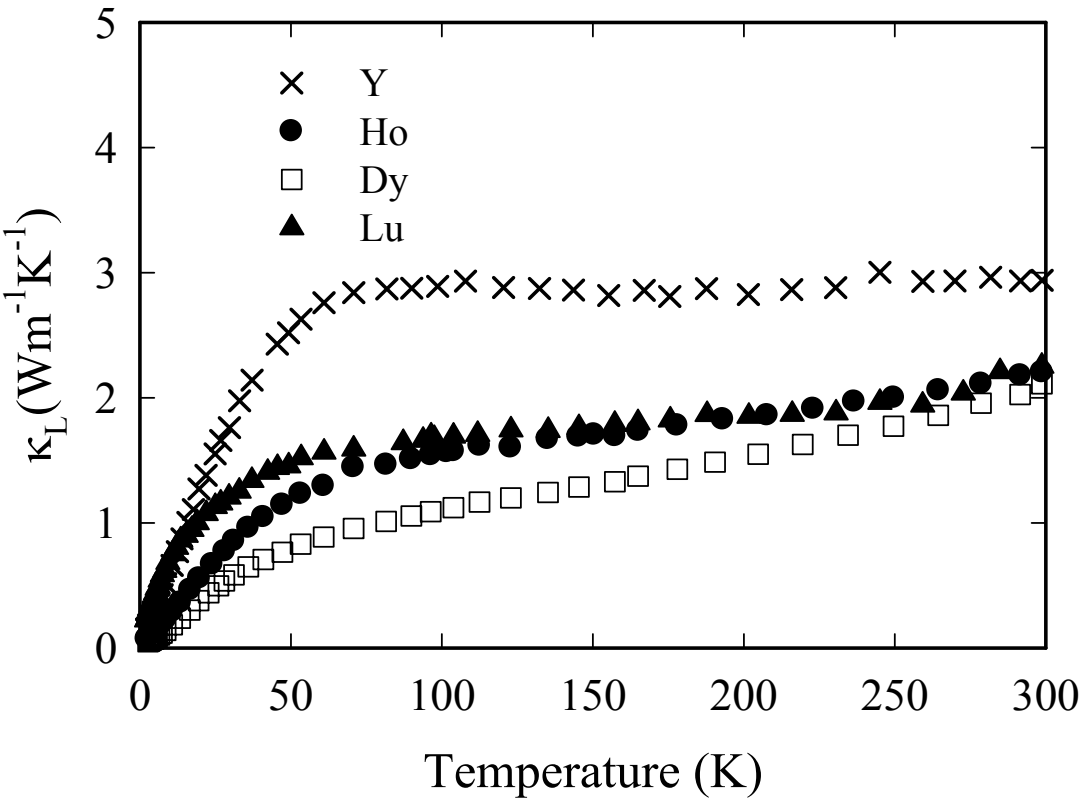

Fig. 6.9. Lattice thermal conductivity of four different $R_3Ru_4Ge_{13}$ compounds as a function of temperature from 2 K to 300 K.

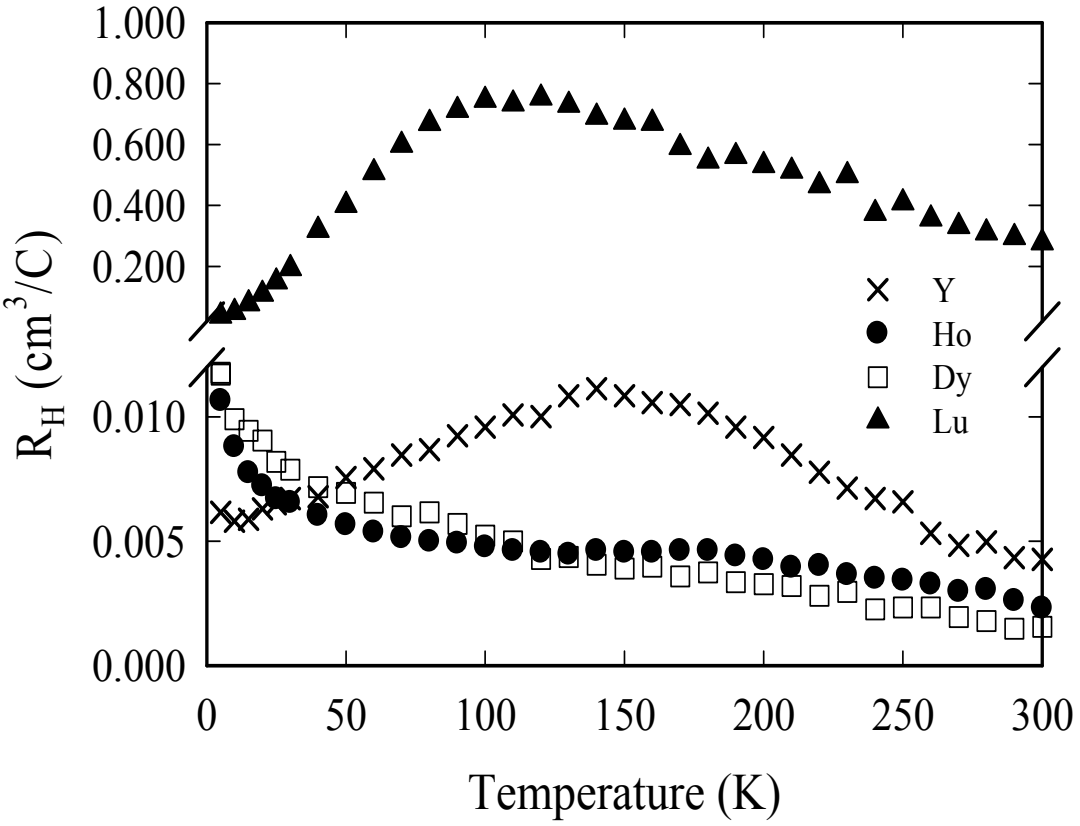

Fig. 6.10. Hall coefficient of different samples $R_3Ru_4Ge_{13}$ (R = Y, Ho, Dy, and Lu) as a function of temperature from 2 K to 300 K.

The thermal conductivity of our samples is displayed in Fig. 6.8 as a function of temperature from 2 K to 300 K. The upward rise at high temperatures is due to an electronic component. We have estimated the electronic component from the electrical conductivity using the Wiedemann-Franz law with Lorenz number equal to 2.45×10^{-8} V^2/K^2 and subtracted it from the total to determine the lattice thermal conductivity (κ_L) of our samples (Fig. 6.9). κ_L is in the range of 2.11-2.94 W/m-K at room temperature. We see that κ_L is remarkably similar to that of many filled skutterudite compounds. Compared to the quintessential thermoelectric materials, the magnitude at room temperature is on the order of that of PbTe (2.1 W/m-K) and about twice that of Bi_2Te_3 (1.5 W/m-K) [6.14-6.15]. Additionally, there is no evidence of a dielectric peak in the lattice thermal conductivity; instead, it displays very flat temperature dependence above 100 K. This very low, nearly temperature independent thermal conductivity may arise from the built-in internal disorder of the $R_3Ru_4Ge_{13}$ structure and is a very desirable feature for thermoelectric applications.

Figures 6.11 and 6.12 display the electrical resistivity and Seebeck coefficient, respectively, as a function of temperature between 300 and 800 K. The offset between the low and high temperature data sets at the overlap temperature (300 K) is about 10% and is within the combined experimental error of the two measurement techniques. The Seebeck coefficient of all samples appears to pass through a maximum near room temperature, suggesting that the minority carrier (electron) transport begins to become important at higher temperatures. This falloff in Seebeck coefficient, however, is not strong and all samples retain *p*-type character to the highest temperatures measured (~800 K). By comparing the samples having *f*-shell valence electrons (Dy, Ho, and Lu) with the one where the *f*-shell is absent (Y), the trends of temperature dependence are similar. It appears that the transport in these compounds is relatively independent of the presence or absence of levels or bands originating from the *f*-shell containing ions.

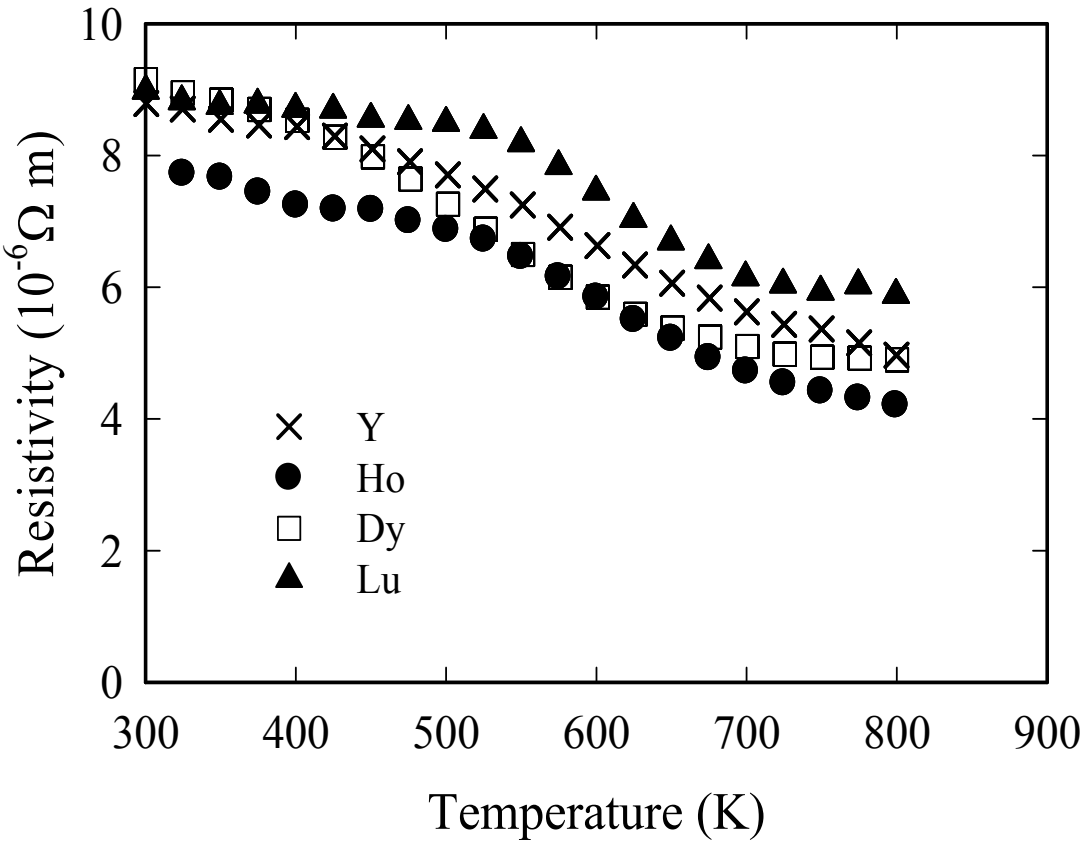

Fig. 6.11. Electrical resistivity of four $R_3Ru_4Ge_{13}$ (R = Y, Ho, Dy, and Lu) compounds as a function of temperature from 300 K to 800 K.

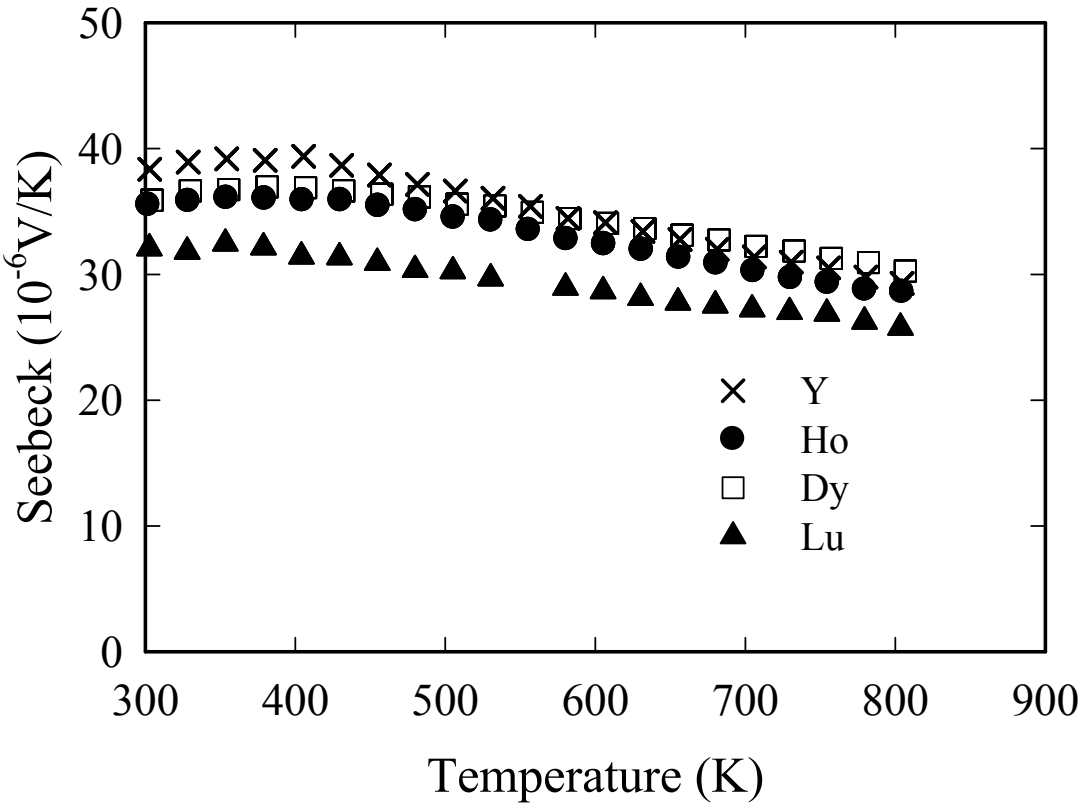

Fig. 6.12. Seebeck coefficient of four $R_3Ru_4Ge_{13}$ (R = Y, Ho, Dy, and Lu) compounds as a function of temperature from 300 K to 800 K.

6.4 Results and Discussions of $Y_3(Ru_{1-x}Co_x)_4Ge_{13}$ (x = 0, 0.1, and 0.2) Samples

In an attempt to influence the electronic and thermal properties of these compounds, we have partially substituted Co for Ru in $Y_3Ru_4Ge_{13}$. The compound $Y_3Co_4Ge_{13}$ is isostructural with $R_3Ru_4Ge_{13}$ [6.16]. Our resistivity results for $Y_3(Ru_{1-x}Co_x)_4Ge_{13}$ with x = 0, 0.1, and 0.2 are shown in Fig. 6.13. The electrical resistivity values increase with increasing Co fraction x and the low temperature rise becomes steeper. Hall coefficient measurements suggest a decrease in the hole concentration of Co-containing samples as compared to $Y_3Ru_4Ge_{13}$, as shown in Fig. 6.15 and Fig. 6.16. This could be caused by the additional valence electrons Co brings into the system. As shown in Fig. 6.14, the Seebeck coefficient also increases quite sharply at low temperature. The slope at low temperatures increases by a factor of 3.4 in going from x = 0 to x = 0.2. However, all samples show a maximum in Seebeck coefficient followed by a decrease at higher temperatures.

If rattling or internal structural disorder is affecting the lattice thermal conductivity, such a process would dominate over any additional scattering due to the mass mismatch between Co and Ru. This is probably the reason why the lattice thermal conductivities (Fig. 6.18) do not differ greatly from the values found in $R_3Ru_4Ge_{13}$ (R = Y, Dy, Ho, and Lu) samples.

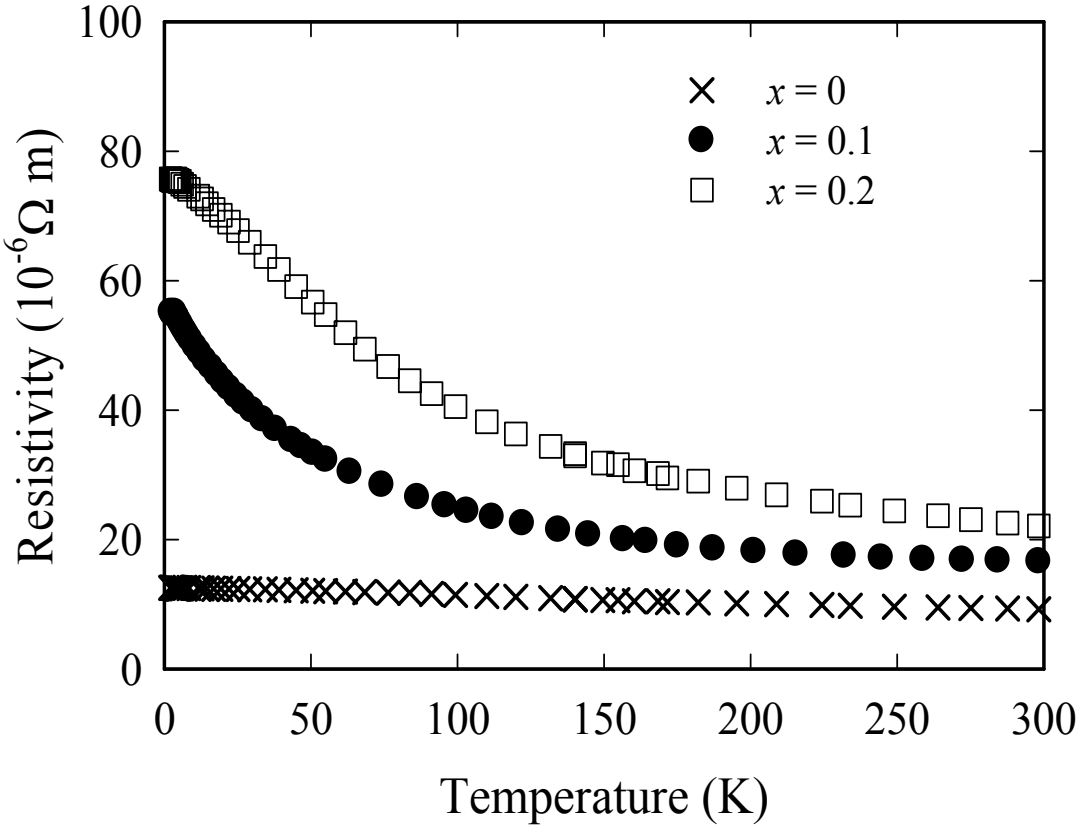

Fig. 6.13. Electrical resistivity of $Y_3(Ru_{1-x}Co_x)_4Ge_{13}$ for x =0, 0.1, 0.2 as a function of temperature from 2 K to 300 K.

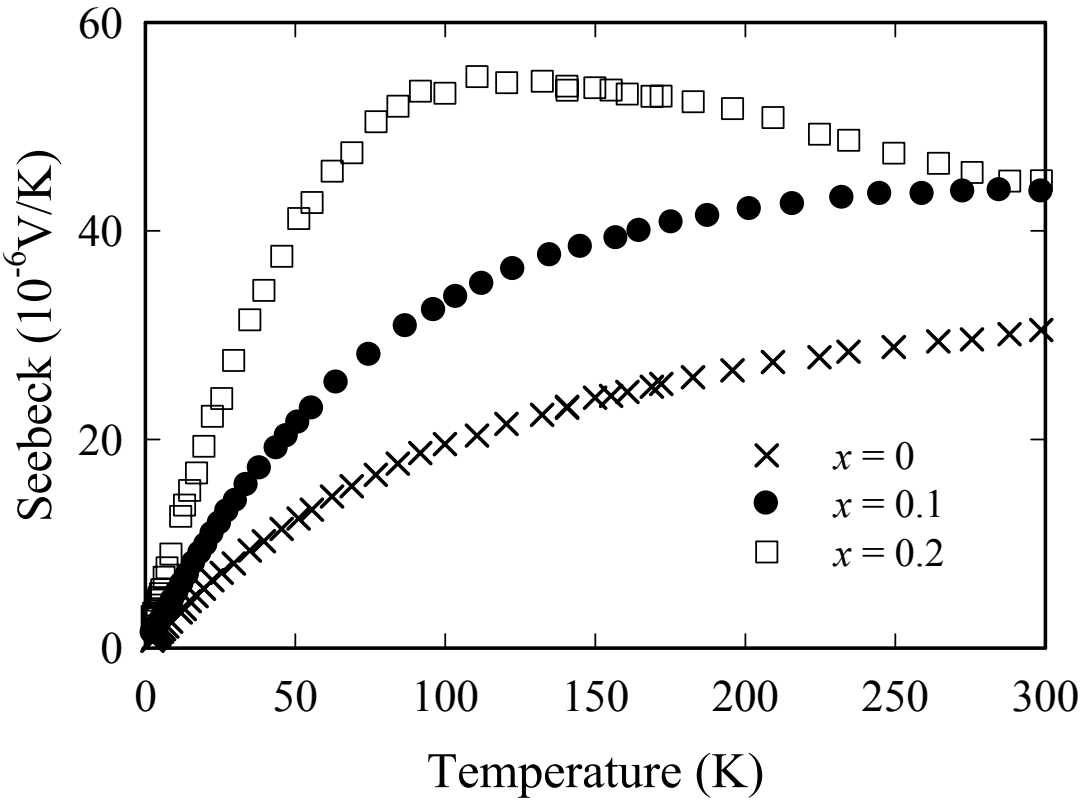

Fig. 6.14. Seebeck coefficient of $Y_3(Ru_{1-x}Co_x)_4Ge_{13}$ for x = 0, 0.1, 0.2 as a function of temperature from 2 K to 300 K.

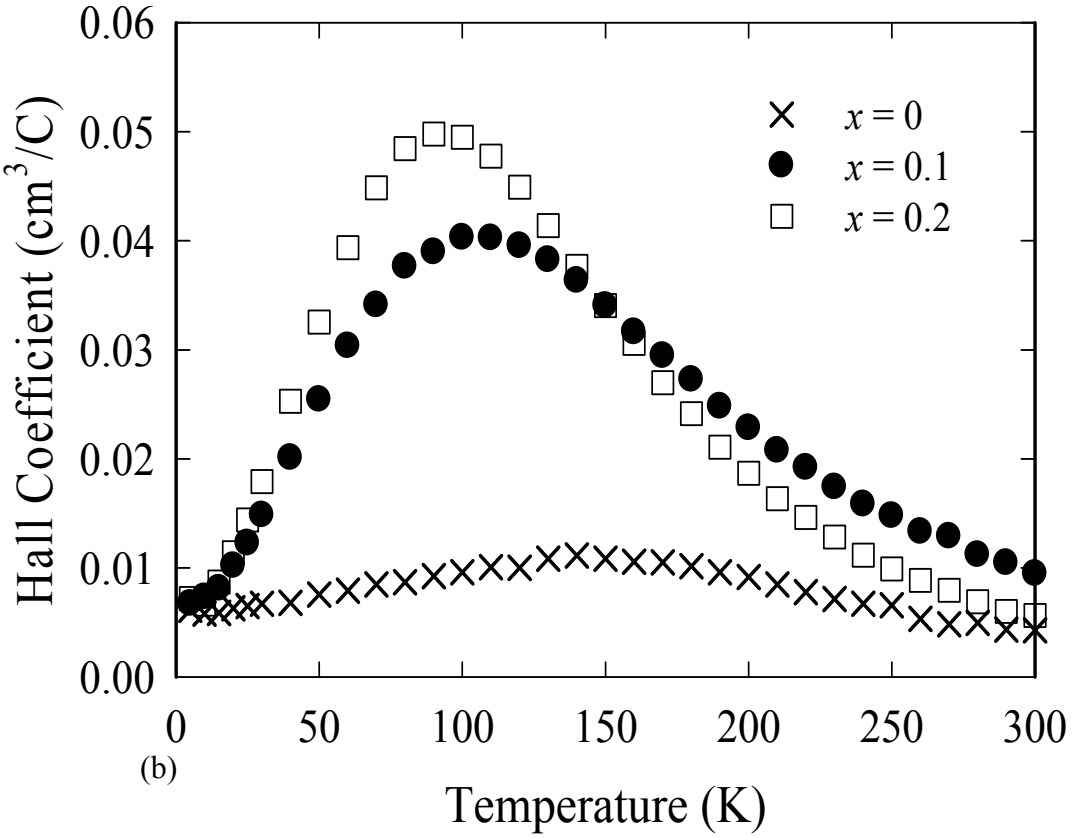

Fig. 6.15. Hall coefficient of $Y_3(Ru_{1-x}Co_x)_4Ge_{13}$ for x =0, 0.1, 0.2 as a function of temperature from 2 K to 300 K.

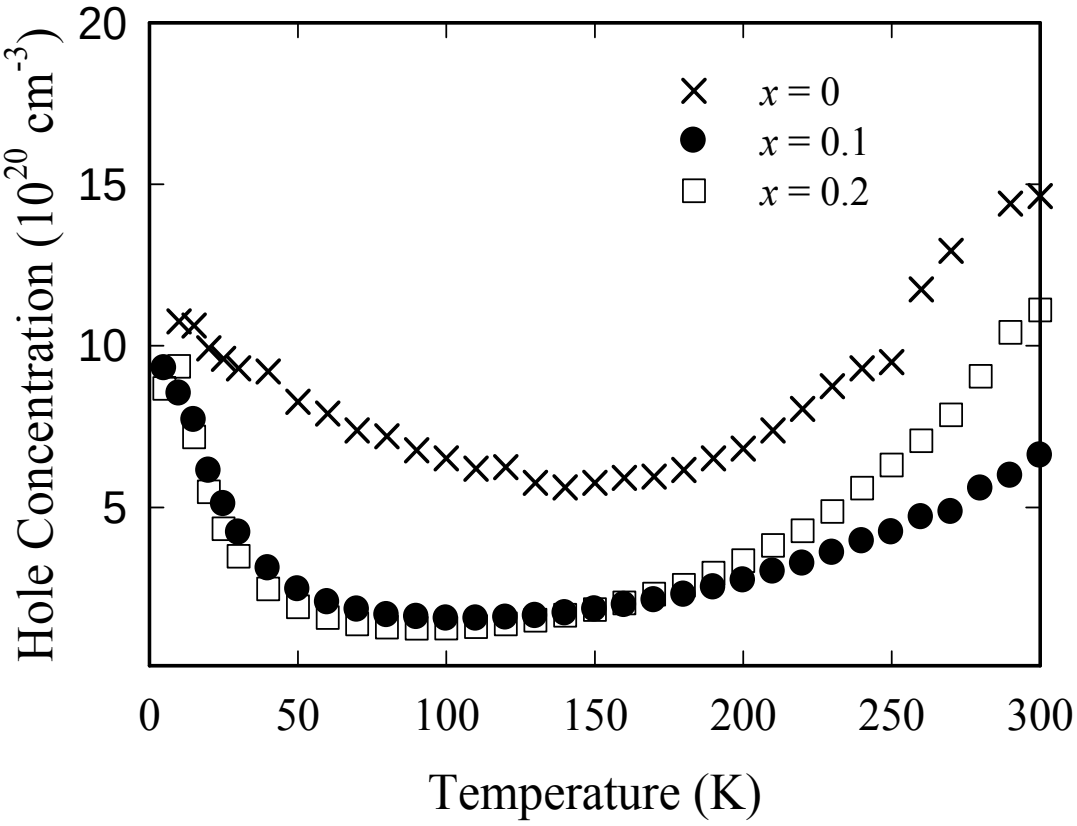

Fig. 6.16. Hole concentration of $Y_3(Ru_{1-x}Co_x)_4Ge_{13}$ for x =0, 0.1, 0.2 as a function of temperature from 2 K to 300 K.

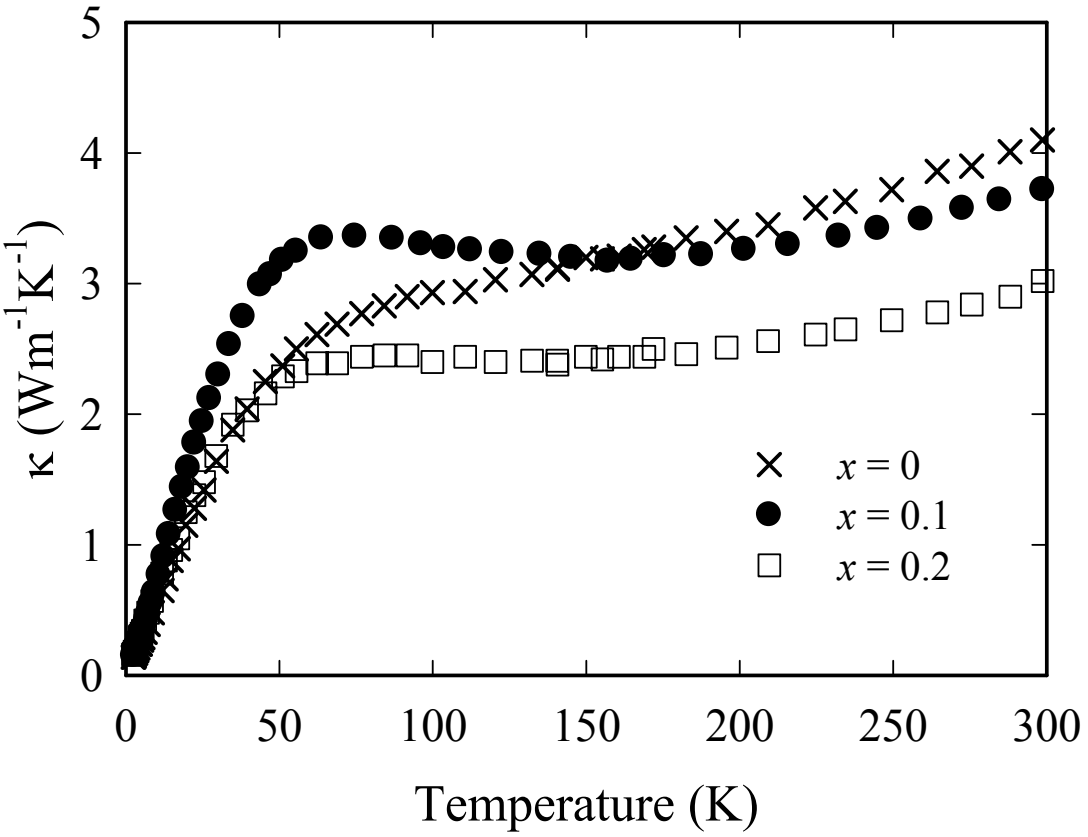

Fig. 6.17. Total thermal conductivity of $Y_3(Ru_{1-x}Co_x)_4Ge_{13}$ for x = 0, 0.1, 0.2 as a function of temperature from 2 K to 300 K.

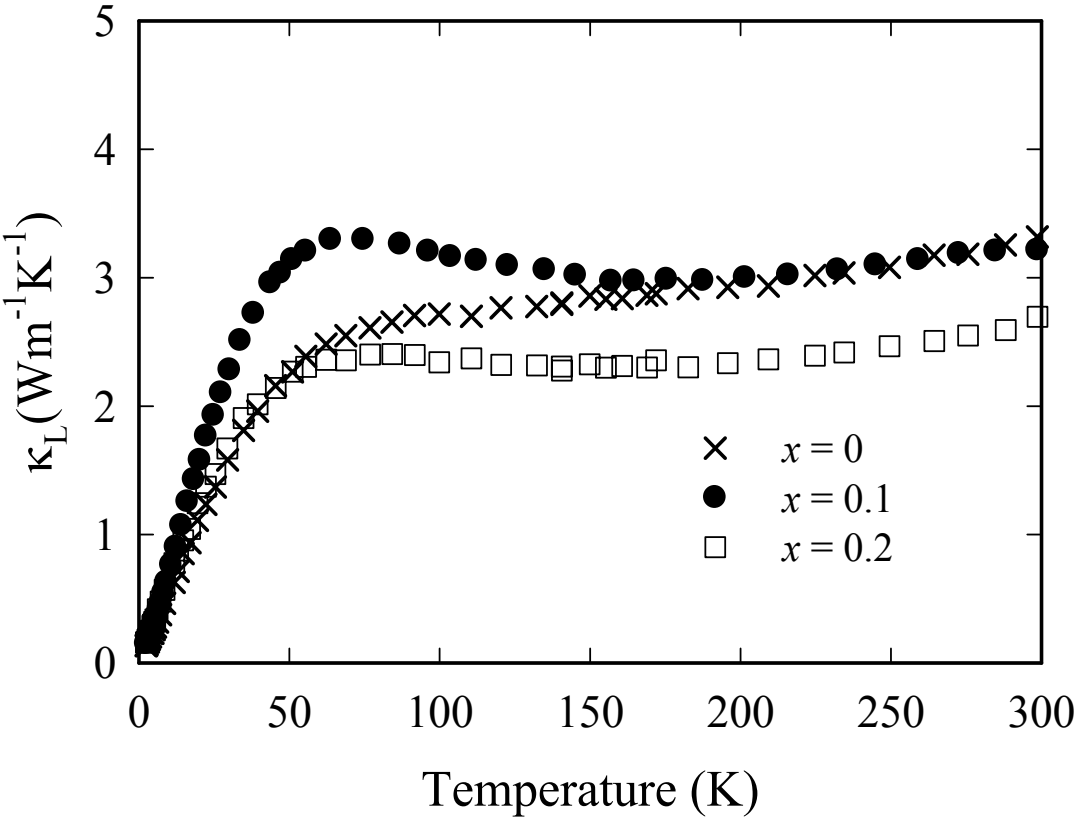

Fig. 6.18. Lattice thermal conductivity of $Y_3(Ru_{1-x}Co_x)_4Ge_{13}$ for x = 0, 0.1, 0.2 as a function of temperature from 2 K to 300 K.

6.5 Conclusions

Similar to filled skutterudites, the compounds of $R_3Ru_4Ge_{13}$ have favorable structure for low thermal conductivity. Lattice thermal conductivity κ_L is in the range of 2.11-2.94 W/m-K at room temperature, comparable to quintessential thermoelectric materials such as PbTe and Bi_2Te_3. Filled skutterudites have optimized ZT at temperatures from 600 K to 900 K. The next step is to determine ZT of $R_3Ru_4Ge_{13}$ up to this temperature range. Co substitution for Ru produces more pronounced semiconducting behavior at low temperatures but does not improve the thermoelectric properties near room temperature. The reduction in lattice thermal conductivity due to rattling and internal structural disorder dominates over the mass mismatch between Co and Ru. Other transition metals can be considered as substitutes for Ru in order to improve ZT.

References

6.1 G. S. Nolas, J. L. Cohn, G. A. Slack, S. B. Schujman, Appl. Phys. Lett. **73**, 178 (1998)
6.2 B. C. Sales, B. C. Chakoumakos, R. Jin, J. R. Thompson, D. Mandrus, Phys. Rev. B **63**, 245113 (2001)
6.3 V. L. Kuznetsov, L. A. Kuznetsova, A. E. Kaliazin, D. M. Rowe, J. Appl. Phys. **87**, 7871 (2000)
6.4 V. Keppens, B. C. Sales, D. Mandrus, B. C. Chakoumakos, C. Laermans, Philos. Mag. Lett. **80**, 807 (2000)
6.5 C. L. Condron, S. M. Kauzlarich, F. Gascoin, G. J. Snyder, Chem. Mater. **18**, 4939 (2006)
6.6 A. Saramat, G. Svensson, A. E. C. Palmqvist, C. Stiewe, E. Mueller, D. Platzek, S. G. K. Williams, and D. M. Rowe, J. Appl. Phys. **99**, 023708 (2006)
6.7 G. S. Nolas, in Thermoelectrics Handbook: Macro to Nano, edited by D. M. Rowe (CRC Press, Boca Raton, FL, 2006)
6.8 C. U. Segre, H. F. Braun, and K. Yvon, in Ternary Superconductors, edited by G. K. Shenoy, B. D. Dunlap, and F. Y. Fradin (Elsevier, New York, NY,1981), p. 243.
6.9 E. L. Thomas, H. O. Lee, A. N. Bankston, S. MaQuilon, P. Klavins, M. Moldovan, D. P. Young, Z. Fisk, J. Y. Chan, J. Solid State Chem. **179**, 1642 (2006)
6.10 J. L. Hodeau, J. Chenavas, M. Marezio, J. P. Remeika, Solid State Commun. **36**, 839 (1980)
6.11 K. Ghosh, S. Ramakrishnan, G. Chandra, Phys. Rev. B **48**, 10435 (1993)
6.12 C. Uher, in Recent Trends in Thermoelectric Materials Research I, Semiconductors and Semimetals, Vol. **69**, edited by T. M. Tritt (Academic Press, San Diego 2001), p. 139-253 and references therein
6.13 K. Ghosh . Ramakrishnan, S. K. Dhar, S. K. Malik, G. Chandra, Phys. Rev. B **52**, 7267 (1995)
6.14 V. Leute, N. Z. Volkmer, Phys. Chem. Neue Folge **144**, 144-145(1985)
6.15 H. J. Goldsmid, in Semiconductors and Semimetals, edited by T. M. Tritt (Academic, San Diego, CA, 2000), Vol. 69, p. 14
6.16 V. A. Bruskov, V. K. Pecharsky, O. I. Bodak, Izv. Akad. Nauk SSSR, Neorg. Mater. **22**, 1471 (1986) [Inorg. Mater. **22**, 1289 (1986)]

Appendix
List of Publications

1. Thermoelectric properties of rare earth-ruthenium-germanium compounds, H.Kong, X.Shi, C.Uher, D.T.Morelli, Journal of Applied Physics **102**, 023702 (2007)

2. Low thermal conductivity and high thermoelectric figure of merit in n-type $Ba_xYb_yCo_4Sb_{12}$ double-filled skutterudites, X.Shi, H.Kong, C.Li, C.Uher, J.Yang, J.R.Salvador, H.Wang, L.Chen, W.Zhang, Appl. Phy. Lett. **92**, 182101 (2008)

3. Substitution of Bi for Sb and its role in the thermoelectric properties and nanostructuring in $Ag_{1-x}Pb_{18}MTe_{20}$ (M = Bi, Sb) (x = 0, 0.14, 0.3), M.K.Han, K.Hoang, H.Kong, R.Pcionek, C.Uher, K.M.Paraskevopoulos, S.D.Mahanti, M.G.Kanatzidis, Chem. Mater. **20**, 3512 (2008)

4. Spinodal decomposition and nucleation and growth as a means to bulk nanostructured thermoelectrics: Enhanced performance in $Pb_{1-x}Sn_xTe$-PbS, J.Androulakis, C.H.Lin, H.Kong, C.Uher, C.I.Wu, T.Hogan, B.A.Cook, T.Caillat, K.M.Paraskevopoulos, M.G.Kanatzidis, J. Amer. Chem. Soc. **129**, 9784 (2007)

5. Thermoelectric properties of quaternary $(Sb_{0.75}Bi_{0.25})_{2-x}In_xTe_3$ single crystals, M.Zabcik, C.Drasar, L.Benes, P.Lostak, H.Kong, C.Uher, the 5th European Conference on Thermoelectrics Proceedings (2007)

6. Large enhancements in the thermoelectric power factor of bulk PbTe at high temperature via synergistic co-nanostructuring, J.Sootsman, H.Kong, C.Uher, J.D'Angelo, C.I.Wu, T.Hogan, T.Caillat, M.G.Kanatzidis (submitted)

7. The high temperature elastic moduli of polycrystalline PbTe measured by resonant ultrasound spectroscopy, F.Ren, E.D.Case, J.Sootsman, M.G.Kanatzidis, H.Kong, C.Uher, E.Lara-Curzio, R.M.Trejo (accepted by Acta Materialia)

8. Nanostructuring and high thermoelectric efficiency in p-type $Ag(Pb_{1-y}Sn_y)_mSbTe_{2+m}$, J.Androulakis, K.F.Hsu, R.Pcionek, H.Kong, C.Uher, J.J.D'Angelo, A.Downey, T. Hogan, M.G.Kanatzidis, Advanced Materials **18**, 1170 (2006)

9. Nanostructures versus solid solutions: low lattice thermal conductivity and enhanced thermoelectric figure-of-merit in $Pb_{9.6}Sb_{0.2}Te_{10-x}Se_x$ bulk materials, P.F.P.Poudeu, J.D'Angelo, H.Kong, A.Downey, J.L.Short, R.Pcionek, T.Hogan, C.Uher, M.G.Kanatzidis, J. Amer. Chem. Soc. **128**, 14347(2006)

10. Strong reduction of thermal conductivity in nanostructured PbTe prepared by matrix encapsulation, J.Sootsman, R.Pcionek, H.Kong, C.Uher, M.G.Kanatzidis, Chem. Mater. **18**, 4993 (2006)

11. Phase segregation and thermoelectric properties of $AgPb_mSbTe_{m+2}$ m = 2, 4, 6, and 8, J.Sootsman, R.Pcionek, H.Kong, C.Uher, M.G.Kanatzidis, Mater. Res. Soc. Symp. Proc. Vol. **886**, F08-05.1 (2006)

12. Nanostructuring and its Influence on the Thermoelectric Properties of the $AgSbTe_2$-SnTe Quaternary System, J.Androulakis, R.Pcionek, E.Quarez, O.Palchik, H.Kong, C.Uher, J.J.D'Angelo, T.Hogan, X.Tang, T.Tritt, and M. G. Kanatzidis, Mater. Res. Soc. Symp. Proc. Vol. **886**, F05-08.1 (2006)

13. Thermoelectric properties of $Bi_2Se_{3-x}As_x$ single crystals, C.Drasar, P.Lostak, A.Krejcova, Z.Zhou, H.Kong, C.Uher, the 3rd European Conference on Thermoelectrics Proceedings (2005)